Study of Scalar Leptons at the TESLA Photon Collider

D I S S E R T A T I ON

zur Erlangung des akademischen Grades
doctor rerum naturalium
(Dr. rer. nat.)
im Fach Physik

eingereicht an der
Mathematisch-Naturwissenschaftlichen Fakultät I
Humboldt-Universität zu Berlin

von
Herr Huber A. Nieto-Chaupis
geboren am 4.Juli 1973 in Lima(Peru)

Präsident der Humboldt-Universität zu Berlin:
Prof. Dr. Christoph Markschies

Dekan der Mathematisch-Naturwissenschaftlichen Fakultät I:
Prof. Dr. Christian Limberg

Gutachter:

1. Prof. Dr. H. Kolanoski
2. Prof. Dr. K. Desch
3. Dr. habil. K. Mönig

eingereicht am:	23. October 2006
Tag der mündlichen Prüfung:	23. April 2007

Abstract

In this thesis, the potential to discover supersymmetric signatures in both e^+e^- and $\gamma\gamma$ colliders evaluated with a Monte Carlo analysis, is discussed. The analysis was focused on the detection of muons, essentially. First, we study the detection of $\tilde{\mu}_R^+\tilde{\mu}_R^-$ in e^-e^+ collisions, whose purpose is the measurement of the $\tilde{\mu}_R$ mass. It was found that an uncertainty of 0.11 GeV (stat) can be achieved. Under the assumption of the real conditions of the ILC photon collider, a study covering the detection of $\tilde{\mu}_R^+\tilde{\mu}_R^-$ and $\tilde{\mu}_L^+\tilde{\mu}_L^-$ pairs for $\sqrt{s}_{e^-e^-} = 0.5$ and 0.6 TeV was performed. According to the simulation, a statistical error for the branching ratios of $\tilde{\mu}_L^\pm \to \tilde{\chi}_1^0\mu^\pm$ of 0.98% and $\tilde{\mu}_L^\pm \to \tilde{\chi}_2^0\mu^\pm$ of 3.97% can be reached. In order to judge the Monte Carlo results, we have used a technique based on a multidimensional fit to evaluate the impact of the branching ratio measurements on the precision of the SUSY parameters. Furthermore, the possibility of identifying heavy neutralinos such as $\tilde{\chi}_2^0$ via detection of the $\mu^-\mu^+\tilde{\chi}_1^0\mu^-\mu^+\tilde{\chi}_1^0$ and $\mu^-e^+\tilde{\chi}_1^0 e - \mu^+\tilde{\chi}_1^0$ final states produced in $\gamma\gamma$ collisions, was explored. This study reveals that the photon collider will provide a remarkable amount of data for this topology, contrary to lepton colliders. Information acquired from energy distributions of final state leptons turns out to be enough to identify the supersymmetric signal. From the invariant mass scatter plots the mass difference of the supersymmetric particles involved in the cascades is determined. It is shown that the $\tilde{\chi}_2^0$ mass and the mass differences $m_{\tilde{\chi}_2^0}$ - $m_{\tilde{\chi}_1^0}$ and $m_{\tilde{\mu}_L}$ - $m_{\tilde{\mu}_R}$ can be quite well estimated. Further potential sources of inherent systematic errors, are discussed.

Keywords:
ILC, photon collider, Supersymmetry, sleptons

Zusammenfassung

In dieser Arbeit wird die Möglichkeit untersucht, am e^+e^-- und am $\gamma\gamma$-Collider mittels einer Monte Carlo Methode supersymmetrische Signaturen zu entdecken. Im Wesentlichen wurde sich auf den Nachweis von Myonen konzentriert. Zuerst wird der Nachweis von $\tilde{\mu}_R^+\tilde{\mu}_R^-$ in e^+e^- Kollisionen untersucht, der die Grundlage zur Bestimmung der $\tilde{\mu}_R$ Masse ist. Es stellte sich heraus, dass eine statistische Unsicherheit von 0.11 GeV erreicht werden kann. Unter Annahme der Realbedingungen am ILC Photon Collider wurde eine Studie durchgeführt, die den Nachweis von $\tilde{\mu}_R^+\tilde{\mu}_R^-$ und $\tilde{\mu}_L^+\tilde{\mu}_L^-$ Paaren bei Schwerpunktsenergien von $\sqrt{s}_{e^-e^-} = 0.5$ und 0.6 TeV beinhalted. Die Simulation ergab, dass ein statistischer Fehler für die Verzweigungsverhältnisse $\tilde{\mu}_L^\pm \to \tilde{\chi}_1^0\mu^\pm$ von 0.98% und $\tilde{\mu}_L^\pm \to \tilde{\chi}_2^0\mu^\pm$ von 3.97% erreicht werden kann. Um die Monte Carlo Ergebnisse beurteilen zu können, wurde eine Methode benutzt, die auf einem multidimensionalen Fit basiert, um den Einfluss der Messungen der Verzweigungsverhältnisse auf die Genauigkeit der SUSY Parameter abzuschätzen. Weiterhin wird die Möglichkeit untersucht, schwere Neutralinos wie $\tilde{\chi}_2^0$ über den Nachweis von $\mu^-\mu^+\tilde{\chi}_1^0\mu^-\mu^+\tilde{\chi}_1^0$ und $\mu^-e^+\tilde{\chi}_1^0e^-\mu^+\tilde{\chi}_1^0$ Endzuständen, produziert in $\gamma\gamma$ Kollisionen, zu identifizieren. Diese Studie verdeutlicht, dass der Photon Collider, im Gegensatz zu Lepton Collidern, eine aussergewöhnliche Datenmenge für diese Topologie bieten wird. Es stellte sich heraus, dass die aus den Energieverteilungen der Leptonen im Endzustand gewonnene Information ausreicht, um das supersymmetrische Signal zu identifizieren. Aus den Streudiagrammen der invarianten Masse wurde die Massendifferenz der supersymmetrischen Teilchen in den Kaskaden bestimmt. Es wird gezeigt, dass die $\tilde{\chi}_2^0$ Masse und die Massendifferenzen $m_{\tilde{\chi}_2^0} - m_{\tilde{\chi}_1^0}$ und $m_{\tilde{\mu}_L} - m_{\tilde{\mu}_R}$ gut abgeschätzt werden können. Weitere potentielle Quellen der innnewohnenden systematischen Fehler werden diskutiert.

Schlagwörter:
ILC, photon kollision, Supersymmetry, skalarteilchen

Dedication

This modest work is dedicated to my family at Lima: my mother Lucinda Chaupis-Valdivia, my father Rolando Nieto-Alfaro, my sister Lourdes Nieto-Chaupis and my brothers Elmer Nieto-Chaupis and Rolando Nieto-Chaupis.

I would like also to dedicate to my friends (forever!) and the people what are trying to reach the highest dreams of the life: "...no, no he terminado, solamente estoy descansando porque aún hay mas camino por recorrer..."

Contents

List of Figures

List of Tables

Chapter 1

Introduction

From 1996 to 1997 three projects, NLC (North America), JLC (Asia) and TESLA (Europe) have published their Conceptual Design Reports for a linear collider in the energy range of a few hundred GeV to about 1 TeV [R$^+$01]. At the beginning of 2004, and after key debates, it was established that the next linear collider should be developed based on the European technology. It was the starting point for the ILC (International Linear Collider) [A$^+$07], based on the superconducting TESLA-like [BF02] technology.

The physics program of ILC involves several strategies to find and measure the Higgs boson mass. Top threshold studies are also contemplated as one of the most important points of the program. Effectively, a precise determination of the top quark and Higgs mass will provide a stringent test of the Standard Model. Another important area to be explored inside the arena of e^+e^- collisions turns out to be Supersymmetry [BB99], the theory which could be the extension of the Standard Model. This theory gives an elegant solution to the hierarchy problem. If Supersymmetry is a low energy theory, or in other words, if the mass spectrum predicted by the Lagrangian is at the TeV scale, the ILC shall be a suitable arena to explore signatures of the predicted particles. Special attention should be paid on the searching for the right-handed scalar muon, because of its simple decay topology. This particle could be the first supersymmetric specie to be discovered. How the ILC could benefit from LHC (Large Hadron Collider) measurements, specially from the Higgs and Supersymmetry sector, is nowadays considered as the "inflexion point" to build the ILC. Several ILC scenarios with respect to the physics program and detector functionality are under study.

An optional project that naturally emerges from taking advantage of the high beam energy, is the construction of a photon collider [KT02]. The highlighted characteristic of this machine is the production of polarized photons with energies up to a fraction of ≈ 0.85 of the initial electron beam. Con-

cretely, a photon collider gives complementary information to the ILC-LHC measurements where the reconstruction of the SUSY Lagrangian is one of the main tasks. Apart from Higgs physics which can be tested by the measurement of the two-photon width of Higgs boson [Ros04], the exploration of a few supersymmetric reactions can only be covered by a photon collider.

Supersymmetric scalar particles produced in a photon collider have been investigated recently, such as the channel $\tilde{\mu}_L \rightarrow \mu\tilde{\chi}_1^0$ where it was shown that a statistical error of about 1.96% for the branching ratio can be reached [M$^+$06]. Because the ILC detector can isolate muons with a high efficiency $\approx$ 99 %, final states containing muons are logically the best option. A notable advantage of $\tilde{\mu}_L \rightarrow \mu\tilde{\chi}_1^0$ decays is its simple topology which is used to assess collider capabilities, and to evaluate some supersymmetric scenarios. In this thesis, we present a detailed Monte Carlo study of the production and detection of supersymmetric scalar leptons by assuming the real conditions of the planned ILC photon collider. We have basically assessed its potential to measure the branching ratio error of decays of the left-handed scalar muon as well as the study of cascade due to $\tilde{\chi}_2^0$ decays are treated.

This thesis is divided this thesis in 8 chapters. In chapter 2, an overview of the ILC program is given. In chapter 3, we provide an introduction of Standard Model and the theory that presumably would be the continuation of the electroweak unification: Supersymmetry. In chapter 4, we describe the functionality of the components of the ILC detector, while the fast simulation package which emulates the response of the ILC detector is given in chapter 5. In this chapter, we also study the production and detection of the right-handed scalar muon in e^+e^- collisions. This study is inside the framework of the SPA project [AS$^+$05].

In chapter 6 a review of the principles of the photon collider is given. Chapter 7 presents a study of the right-handed and left-handed scalar muon production and detection in the ILC photon collider, respectively. We have investigated through a simple strategy of selection the possible value of the branching ratio error for the main decay of the left-handed smuon under real circumstances. It is actually the major result of this work. In chapter 8, we explain how to measure the $\tilde{\chi}_2^0$ mass in an attempt to demonstrate a new feature of $\gamma\gamma$ collisions. The measurement of the mass difference of supersymmetric particles involved in cascade decays is performed. Finally, we draw conclusions from the obtained results in this thesis.

Chapter 2

The ILC Project

2.1 The ILC Linear Collider

A model of a possible layout of the experimental areas and facilities for a linear collider was published in the Technical Design Report (TDR) [R+01] of the TESLA (Tera Electron Superconducting Linear Accelerator) collaboration. At the beginning of 2003, a world-wide consensus declared the

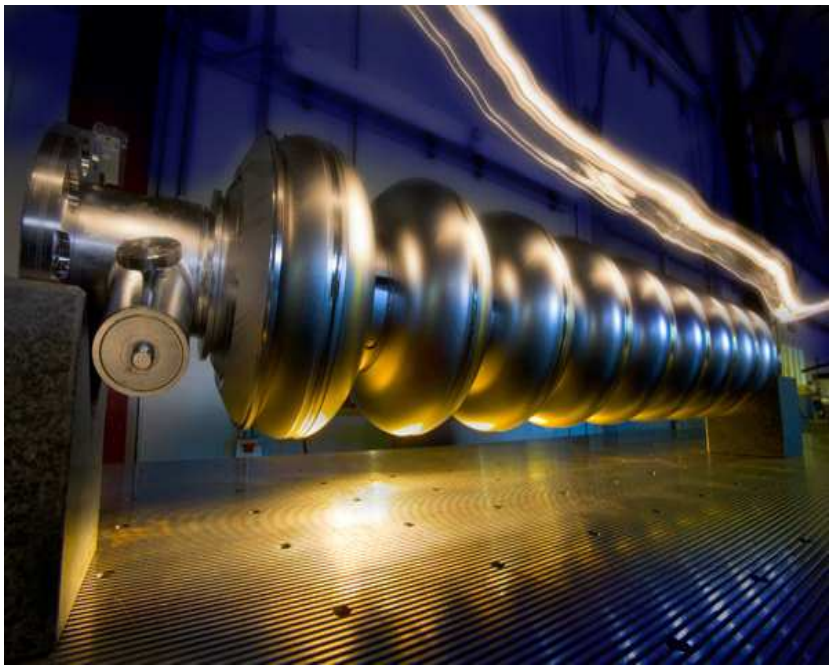

Figure 2.1: TESLA 9-cell 1.3 GHz SRF cavities from ACCEL Corporation in Germany for ILC.

"cold" technology (or European proposal) as the one which is nearer to fulfill the physics requirements of a future e^+e^- collider. Recently, it has been published the Reference Design Report where the newest developments and other important progresses are described [W$^+$07b]. The accelerator has a total length of 33 km and consists of two parts: one for the e^+ and one for the e^- beam-line. The "European proposal" is based on the technology of superconducting cavities. In Fig. 2.1 a photography of these cavities is shown. On the other hand, the superconducting accelerator has already been successfully tested at the TESLA test facility, at DESY Hamburg (Fig. 2.2). In essence, the superconducting technology relies on cavities with an accelerating gradient exceeding 25 MV per meter against to the 7 MV/m used for the LEP2. The importance of this technology is based on its main characteristics,

Figure 2.2: Superconducting accelerator structures at the TESLA test facility at DESY in Hamburg.

Parameter	Units	TESLA (ILC)
$\sqrt{s}_{e^+e^-}$	[TeV]	0.500
Luminosity $\mathcal{L}$	$[10^{34}/(cm^2\text{s})]$	3.4
Repetition rate f_r	[Hz]	5
No. bunch/train n_b		2820
No. particle/bunch N_e	$[10^{10}]$	2
Bunch spacing Δt_b	[ns]	337
Accel. gradient G	[MeV/m]	23.4
Beams power $2P_b$	[MW]	22.6
IP beta-function β_x/β_y	[mm]	15/0.4
R.m.s beam size at IP σ_x/σ_y	[nm]	553/5
R.m.s beam length σ_z	$[\mu]$	300

Table 2.1: The relevant parameters of the TESLA linear collider for $\sqrt{s}_{e^+e^-}$= 500 GeV [Beh01a]

- a small power dissipation;
- a high power transfer efficiency to the beam particles.

A mandatory requirement of the accelerator is to achieve very small sizes of the electron and positron bunches at the interaction point (IP). Conservation of small sizes of the beams during the acceleration would avoid large wakefields, which could spoil the quality of the beam. In Table 2.1 is listed the most relevant parameters of the TESLA linear collider for $\sqrt{s}_{e^+e^-}$ = 500 GeV. It is easy to note that they surpass numerically the ones used at LEP2. TESLA have proposed to reach a $\sqrt{s}_{e^+e^-}$= 500 GeV in comparison to the 209 GeV reached by the LEP2. Besides the center-of-mass energies, a crucial parameter is the luminosity. The notable difference between the TESLA luminosity and the one used in the past is reflected in the ratio $\mathcal{L}_{TESLA}/\mathcal{L}_{LEP2}$ = 3.4$\times$ 10^3 which might be affected by Beamstrahlung and other beams effects. They give rise to an unavoidable energy spread of $\delta E/E \approx 2\%$. Indeed, TESLA aims an ultra-fine bunch spacing of 337 ns against to the 22μs used at LEP2 while a R.m.s beam size at IP σ_x/σ_y = 553/5 for TESLA compared to 200/2.5 reached at LEP2 is foreseen.

2.2 The Physics Program

2.2.1 The Standard Model Higgs

The ILC, in its first phase would operate in the 300 GeV to 500 GeV center-of-mass energy range. The most essential reason in building the e^+e^- collider is that of measuring the Higgs boson mass, and to have access to its properties [D+07]. Since the past up to now, it have been believed that the Higgs boson should exist at the electroweak scale, having a mass of around 120 GeV. Thus, the ILC would encounter such a particle at energies $\sqrt{s}_{e^-e^+} \approx 240$ GeV. Basically, the Higgs [Hig64] can be produced by the Higgsstrahlung process

$$e^+e^- \rightarrow Z^* \rightarrow Z^0h^0 \tag{2.1}$$

or by the fusion of W^+W^- and Z^0Z^0 bosons

$$e^+e^- \rightarrow \nu\bar{\nu}h^0 \quad and \quad e^+e^- \rightarrow e^+e^-h^0. \tag{2.2}$$

In a scenario that contemplates $\sqrt{s}_{e^+e^-}$= 360 GeV and M_h = 140 GeV, the

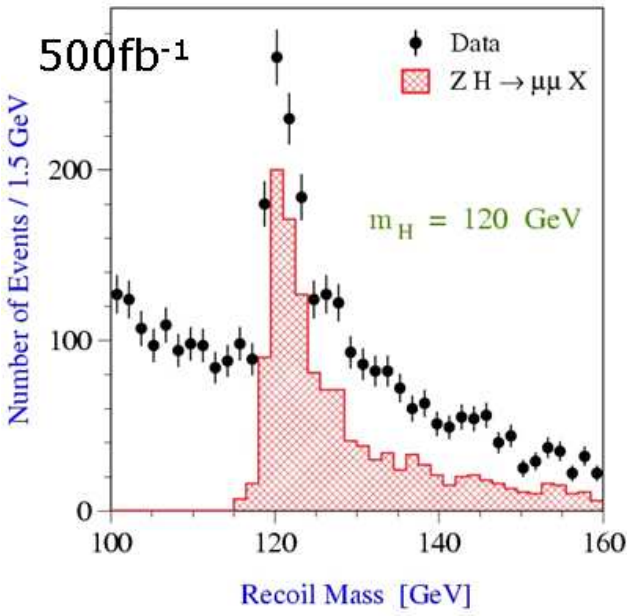

Figure 2.3: Monte Carlo simulation of the reconstructed recoil mass (against Z^0 boson) of Higgs boson production via Higgs-strahlung and background events, to be observed in e^+e^- collisions. "Data" means the simulated signal.

Higgsstrahlung process is the most important one. Two techniques have been studied exhaustively

- The calculation of the mass recoiling against the Z^0. Based on kinematics, the recoil mass is expressed as follows,

$$m_{\text{rec}} = \sqrt{s + m_{\ell\ell}^2 - 2 \cdot E_{\ell\ell} \cdot \sqrt{s}} \tag{2.3}$$

  where $m_{\ell\ell}$ and $E_{\ell\ell}$ are the di-lepton mass and energy respectively whereas $\sqrt{s}$ denotes the center-of-mass energy. This technique will be conveniently applied in the $Z^0 \to e^+e^-$ and $\mu^+\mu^-$ decays. It is noteworthy that this method has the unique feature of being independent on assumptions about the Higgs decay modes.

- Direct reconstruction of the invariant mass of the Higgs decay products. For instance at the ILC the $h^0 \to b\bar{b}$ decays might be reconstructed through

$$m_{h^0} = \sqrt{(E_{\text{jet}}^+ + E_{\text{jet}}^-)^2 - \Sigma_j (p_{j,\text{jet}}^+ + p_{j,\text{jet}}^-)^2} \tag{2.4}$$

  where E_{jet} and $p_{j,\text{jet}}$ is the jet energy and momentum, and $j = x, y, z$. The reconstruction of the Higgs mass is also viable through the $h^0 \to WW$, $\tau^+\tau^-$ decays.

2.2.2 Supersymmetry

The physics program of ILC includes the testing of Supersymmetric theories which have been intensively searched in former experiments. In reality, SUSY is the most promising candidate for being the theory beyond Standard Model and it is believed to be discovered in the electroweak scale. It means that its mass spectrum contains superpartners whose masses are ranging between 100 GeV and 400 GeV. SUSY is also attractive because it predicts a specie which could be the most elemental component of cold dark matter in universe.

The roles of the ILC experiment are not restricted to the discovery of new supersymmetric particles. Masses at the level of one per mile, quantum numbers, and various couplings of Supersymmetric particles can be measured with good accuracy. Determination of these quantities without relying on some specific model of Supersymmetry breaking is necessary in order to test and establish a new symmetry principle of nature.

For the testing of Supersymmetry, beam polarization plays an important role. Since the production of squarks and sleptons are sensitive to polarization effects, the initial electron-positron beam polarization is very useful to distinguish left-handed or right-handed superparticles. Even though the production of scalar leptons doubles when polarizated beams are used. Although the ILC can guarantee at least one polarizated beam (e^-), polarization of

positron beam is desirable. It would significantly enhance cross sections and to set a promising arena for precision measurements.

Therefore, the ILC is compromised to the :

- determination of mass and spin from decay energy distributions,
- production angle distribution,
- threshold scans in pair production,
- reconstruction of chargino and neutralino mass matrices from cross sections,
- reconstruction of angular distributions with possible effects on CP violation,
- determination of the slepton-lepton-bino coupling through $e^+e^- \rightarrow \tilde{\ell}^+\tilde{\ell}^-$,
- searching of lepton flavour violation in slepton pair production,
- testing of gaugino mass as given by Grand Unification Theories (GUT).

In order to determine the supersymmetric Lagrangian, all these measurements are needed. Moreover, in order to obtain a whole picture of a supersymmetric model, it is most likely that information from LHC and ILC has to be combined. Combining colored supersymmetric particles mass measurements from LHC and slepton/chargino/neutralino masses from ILC, we may be able to figure out the origin of Supersymmetry breaking in nature.

2.2.3 Top Threshold Studies

One of the most important topics of the physics program of a linear collider, is the detailed study of the top quark properties. Top quarks will be copiously pair-produced at such a machine and, since they are heavier than the intermediate vector boson, might be heavier than the Higgs boson as well. Thus is not unreasonable to think that their properties might well be different from the ones of the lighter quarks. The dominant top production channel goes through the

$$e^+e^- \rightarrow Z^0 \rightarrow t\bar{t} \tag{2.5}$$

reactions. The $t\bar{t}$ production cross section is about 650 fb at $\sqrt{s}_{e^+e^-} =$ 500 GeV. At the foreseen luminosities of 10^{33} -10^{34} cm^{2}s^{-1} (or 10-100 fb^{-1}

per year) the event sample is sufficient for detailed studies. The ILC will be an ideal scenario to measure precisely the top quark mass. An energy scan around the production threshold is needed. It takes into account three observables:

- The total production cross section,
- the forward-backward asymmetry,
- and top momentum distribution.

In addition, it is expected to measure the Top quark mass within a precision ± 0.05 GeV.

2.2.4 Extra Dimensions

Since 1998, the topic of Extra Dimensions (ED) has been intensively investigated, as to its phenomenological aspects in collider and possible cosmological implications.

Essentially, ED theories have predicted the existence of extra spatial dimensions hidden in the universe, or technically speaking, the compactification scale of the extra dimension can be as large as inverse TeV or even submilimeter. It is noteworthy that these kind of predictions have its origin in string theories. The test of ED might be the beginning of an era of subsequent tests of string theories.

Two hypotheses have called the attention of the HEP community: In the first one, gravity propagates from the SM brane to the higher D>4 dimensions, for energies $\approx$ 1 TeV, well below the Planck scale [Ant98]. Thus, graviton fields can be described by Kaluza-Klein states with masses of order of n/R, where n denotes the number of ED and R the radii of compactification. The ILC can measure two parameters of these hypothesis, the fundamental Plack scale Λ_D and n through the

$$e^+e^- \rightarrow \gamma G_{KK} \tag{2.6}$$

reactions with G_{KK} denoting the graviton states. A sophisticated technique would have to be applied to detect one single photon with a substantial selection efficiency.

The second hypothesis assumes as a cornerstone the metric containing a warp factor exp(-$2kr_c\phi_b$) [RS99], with k the curvature, r_c the compactification radius and ϕ_b the distance between the gravity and the SM brane. The introduced variable ϕ_b is contained between ϕ_b=0, the gravity located brane and ϕ_b=π the SM brane. This model is known as the Randall-Sundrum

model, and it predicts the existence of a particle called radion living along the bulk. Furthermore, this model offers a potential solution to the hierarchy problem. The testing of this model at the ILC would consist in detecting anomalies in the

$$e^+e^- \to \mu^+\mu^- \tag{2.7}$$

reactions, where its resonant s-channel would be affected. The ILC would generate enough statistics within ≈4 years of running to extract the ED signatures from background processes.

2.3 A Second Interaction Region

In addition to e^+e^- collisions, the ILC have contemplated the inclusion of a second interaction region, based on the possibility to collide laser photons on the electron beam and therefore to get backscattered photons carrying energies of the same magnitude of the initial electrons [Gin81].

The collision with another backscattered photon occurs in a few millimeters of distance from the conversion point. In addition to the photon collisions, electron-photon and electron-electron collisions are also expected.

The essential purpose of having a supplementary laboratory is based on the idea of extending our knowledge of Higgs and beyond Standard Model physics. Concerning the photon collider, there is a priority on the following reactions,

- Higgs physics:

$$\gamma\gamma \to h^0 \to b\bar{b}, \qquad \gamma\gamma \to H, A \to b\bar{b} \tag{2.8}$$

- Supersymmetry:

$$\gamma\gamma \to \ell\tilde{\ell}, q\tilde{q}, \chi_i^+\tilde{\chi}_i^-, \qquad \gamma e^- \to \tilde{e}_R^-\tilde{\chi}_1^0, \tilde{e}_L^-\tilde{\chi}_2^0 \tag{2.9}$$

- Anomalous coupling at Standard Model

$$\gamma\gamma \to W^+W^-, \qquad e^-\gamma \to \nu W^- \tag{2.10}$$

One of the most important issues is the measuring of the uncertainty of the two-photon width of the light Higgs boson in its dominant channel $h \to b\bar{b}$. Monte Carlo simulations have shown that an error of up to 1.9% can be reached [Ros04]. Several simulations of signal and some strategies for rejecting background have been performed and analyzed in Ref. [M$^+$06] for

various processes listed above. In this thesis we will discuss in detail those processes where the production of scalar muons and heavy neutralinos might be available for ILC energies. The aim of this thesis is also to demonstrate that the second interaction region would serve to reconstruct some portions of SUSY Lagrangian which would not be covered neither by LHC nor ILC.

Chapter 3

Theoretical Aspects

3.1 The Role of Quantum Electrodynamics

Unification in Physics have been an important fact what have inspired to theoreticians to formulate and propose esthetic models in order to provide a simplified view of laws in nature. Following this spirit, during the 70s, even it was in somewhat a clear conviction to reformulate the V-A model created by Fermi by using arguments based on symmetry principles. To be more precise, the developments in pursuing electroweak unification have extensively used the gauge invariance as a cornerstone to built the complete theory and herein to postulate the dynamics among the fields. The electroweak theory often called Standard Model have been successfully tested in former experiments in high energy regimes. Various of its free parameters has been measured within an extraordinary precision confirming the predictive power of model.

Even current experiments are verifying exceedingly the model at the low energy scale [QWe07]. Nevertheless, it is widely accepted that a new model would have to replace the SM in order to explain new phenomena. Furthermore since some decades ago have been troublesome to face some aspects as the hierarchy problem, fine tunnning, etc, which suggests the incorporation of new symmetries in nature. We shall briefly describe the main features of SM and try to justify the emergence of SUSY and its elements based in two excellent books [BT06] [Bie07]. The case of Quantum Electrodynamics (QED) is the best case to understand the importance and usage of gauge principles. It is the most elemental description of interactions consisting in the dynamics of fermions and gauge fields.

Traditionally, QED have been postulated in a semiclassical manner. We kept this definition unless the gauge field is quantizated. We stress that the field is semiclassical in the sense that its representation is actually an ordinary 4-vector potential. The QED Lagrangian can be written as

$$\mathcal{L} = i\bar{\psi}\gamma_\mu\partial^\mu\psi - m\bar{\psi}\psi \tag{3.1}$$

which is invariant under the transformation

$$\psi(x) \rightarrow e^{iq\alpha(x)}, q = charge. \tag{3.2}$$

This transformation is accompanied with the introduction of a field A_μ inside the covariant derivative, and due to the insertion of this field a new term proportional to $|F_{\mu\nu}|^2$ is added to the Lagrangian,

$$\mathcal{L} = i\bar{\psi}\gamma_\mu(\partial^\mu + iqA_\mu(x))\psi - m\bar{\psi}\psi + \frac{1}{4}F^{\mu\nu}F_{\mu\nu}, \tag{3.3}$$

with $D^\mu = \partial^\mu + iqA_\mu(x)$. In order that the Lagrangian keeps its invariance, the field is "forced" to suffer a redefinition,

$$A_\mu(x) \rightarrow A_\mu(x) - \partial_\mu\alpha(x) \tag{3.4}$$

leading to guarantee the invariance under a set of local gauge transformations forming the Abelian group U(1). Note the omission of a term proportional to $m_\gamma A^\mu A_\mu$ which destroys the symmetry and gives rise to a massless photon. The Lagrangian allows to build the vertices given by $iq\bar{\psi}\gamma_\mu A_\mu(x)\psi$ which in the most simple words we can call it as the coupling between matter and light. A similar structure holds for scalar fields. For this case the Lagrangian reads

$$\mathcal{L} = (D^\mu\phi)^*(D_\mu\phi) - m\phi^*\phi + \frac{1}{4}F^{\mu\nu}F_{\mu\nu}, \tag{3.5}$$

and will be used for describing the interaction between photons and new particles such as the scalar supersymmetric particles. In addition, interactions between Dirac fields (or scalars) and light emerges from a concept of gauge invariance.

Unlike electrodynamics, QCD obeys a structure non-Abelian reflected in the gluon field or SU(3) gauge bosons. Thus the Lagrangian can be expressed as

$$\mathcal{L}_{QCD} = \Sigma_j\bar{q}_j(i\gamma^\mu D_{A\mu} - m_j)q_j + \frac{1}{4}G_A^{\mu\nu}G_{A\mu\nu}, \tag{3.6}$$

where $G_{A\mu\nu} = \partial_\mu G_{A\nu} - \partial_\nu G_{A\mu} - gf_{ABC}G_{B\mu}G_{C\nu}$, $D_{A\mu} = \partial_\mu + ig_s\frac{\lambda_A}{2}G_{A\mu}$ and i runs overall flavors. The interactions between the quark fields q_i and their

corresponding field gauges or gluons are now extracted by writing explicitely each individual term,

$$\mathcal{L}_{\text{kin}} = -g_s \Sigma_i \bar{q}_i \gamma^\mu \frac{\lambda_A}{2} G_{A\mu} q_i + \frac{1}{2} g_s f_{ABC} (\partial_\mu G_{A\nu} - \partial_\nu G_{A\mu}) G^\mu_B G^\nu_C - \frac{1}{4} g_s^2 f_{ABC} f_{AB'C'} G_{B\mu} G_{C\nu} G^\mu_{B'} G^\nu_{C'}, \quad (3.7)$$

where the first one of right side gives rise to the vertice quark-gluon, whereas the second and third ones describe triple and quartic gluon coupling. These self-interactions are derived from gauge principles, and it shall be best appreciate in electroweak interactions.

3.1.1 Electroweak Unification

Based on QED current-current interactions, early attempts have provided an adequate framework to explain nuclear beat decay $n \to p + e^- + \bar{\nu}_e$ as follows

$$\mathcal{H} = \frac{G_F}{\sqrt{2}} [\bar{p}(x) \gamma^\mu n(x)][\bar{e}(x) \gamma_\mu \nu_e(x)] + \text{h.}c \quad (3.8)$$

where $p, n, ...$ are the spinor fields and G_F is the Fermi constant $G_F = 10^{-5} m_p^{-2}$. Unfortunately, it was serious problems in using this Hamiltonian to face the Gamow-Teller transitions and other processes of same type. But once the parity violation was discovered, invaluable insights toward a full comprehension of weak interactions arrived to postulate the called V-A theory. Again, for beta decay we have

$$\mathcal{H} = \frac{G_F}{\sqrt{2}} [\bar{p}(x) \gamma^\mu (g_V + g_A \gamma_5) n(x)][\bar{e}(x) \gamma_\mu (1 - \gamma_5) \nu_e(x)] + \text{h.}c, \quad (3.9)$$

with $g_V \approx 1$ and $g_A / g_V \approx$ -1.26. One important fact have been the inclusion of axial vectors to have a better description of nuclear interactions. It was found that the V-A theory is non-renormalizable since the Fermi coupling G_F has negative mass dimension. Phenomenologically, the theory had serious problems as for example: the cross sections increase monotonically for center-of-mass energies. It certainly enters in contradiction with the principle of unitarity demanded by the S matrix. Concretely, the V-A theory yields σ to be proportional to $G_F^2 (\sqrt{s})^2 = G_F^2 s$ which is inconsistent with basic principles and therefore the theory should be replaced by a new fully consistent theory. Mathematically, the model would have to have propagators or intermediate lines to drop out the inconsistencies.

Then, Fermi had to insert "new" field gauges in his new formulation of weak interactions, in a very similar manner to the case of QED where the

fields would play the role of intermediate messengers like the photon which mediates the Coulomb force. These gauge fields of the weak interaction would clearly be the $W^{\pm}$ bosons, and they couples to the matter currents as follow

$$\begin{aligned}\mathcal{L} = g\bar{u}\gamma^{\mu}\frac{1-\gamma_5}{2}dW_{\mu}^{+} + g\bar{d}\gamma^{\mu}\frac{1-\gamma_5}{2}uW_{\mu}^{-} \\ +g\bar{\nu}_e\gamma^{\mu}\frac{1-\gamma_5}{2}eW_{\mu}^{+} + g\bar{e}\gamma^{\mu}\frac{1-\gamma_5}{2}\nu_e W_{\mu}^{-} \\ +g\bar{\nu}_{\mu}\gamma^{\mu}\frac{1-\gamma_5}{2}\mu W_{\mu}^{+} + g\bar{\mu}\gamma^{\mu}\frac{1-\gamma_5}{2}\nu_{\mu}W_{\mu}^{-}. \end{aligned} \tag{3.10}$$

The next step in that of taking the Lagrangian structure of QED $\mathcal{L} = J^{\mu}A_{\mu}$ for the formulation of a novel Lagrangian capable to predict the interaction between a $SU(2)$ gauge field A_{μ}^{a} and a doublet fermion Ψ as

$$\mathcal{L}_{int} = gJ^{a\mu}A_{\mu}^{a}. \tag{3.11}$$

With the definition of the associated currents $J_{\pm}^{\mu} = J^{1\mu} \pm iJ^{2\mu}$, (3.11) can be written as

$$\mathcal{L}_{int} = \frac{g}{\sqrt{2}}(J_{+}^{\mu}W_{\mu}^{+} + J_{-}^{\mu}W_{\mu}^{-} + gJ^{3\mu}A_{\mu}^{3}). \tag{3.12}$$

It is easy to note in (3.10) the current exhibits a structure similar to $J_{+}^{\mu} = \bar{\psi}_1\gamma^{\mu}\psi_2$ and $J_{-}^{\mu} = \bar{\psi}_2\gamma^{\mu}\psi_1$ suggesting that the fermions obey a $SU(2)$ structure. Indeed of (3.10),

$$\bar{u}\gamma^{\mu}\frac{1-\gamma_5}{2}d = \bar{u}\frac{1+\gamma_5}{2}\gamma^{\mu}\frac{1-\gamma_5}{2}d = \bar{u}_L\gamma^{\mu}d_L, \tag{3.13}$$

by implying that only the left-handed components of the quarks and leptons are elements of the non-Abelian symmetry group $SU(2)$ and they couples to the $W^{\pm}$ bosons.

3.1.2 The SU(2)xU(1) Model

The electromagnetic gauge theory can be unified with the non-Abelian $SU(2)$ to give rise to the well-known Standard Model or $SU(2)\times U(1)$ model. Thus, the Lagrangian which describes the gauge and scalar sectors can be written as

$$\mathcal{L} = -\frac{1}{4}F^{a\mu\nu}F_{a\mu\nu} - \frac{1}{4}B^{a\mu\nu}B_{a\mu\nu} + D^{\mu}\Phi^{\dagger}D_{\mu}\Phi - V(\Phi^{\dagger}\Phi) \tag{3.14}$$

with $F_{\mu\nu}^{a}$ is the $SU(2)$ covariant field strength whereas $B_{\mu\nu} = \partial_{\mu}B_{\nu} - \partial_{\nu}B_{\mu}$ the $U(1)$ field. Respect to the Higgs doublet Φ, its derivative is covariant under $SU(2)$ and $U(1)$

$$D_{\mu}\Phi = \partial_{\mu}\Phi - igA_{\mu}^{a}\frac{\sigma^{a}}{2}\Phi - i\frac{g'}{2}y_{\phi}B_{\mu}\Phi. \tag{3.15}$$

The potential reads

$$V(\Phi^\dagger\Phi) = -m^2\Phi^\dagger\Phi + \lambda(\Phi^\dagger\Phi)^2. \tag{3.16}$$

with the ground state according to the Higgs mechanism

$$< \Phi >= \Phi_0 = \begin{pmatrix} 0 \\ \frac{v}{\sqrt{2}} \end{pmatrix}, v = \sqrt{\frac{m^2}{\lambda}}. \tag{3.17}$$

Taking the covariant derivative and the ground state, we get

$$< D_\mu\Phi >= \begin{pmatrix} -ig\frac{v}{\sqrt{2}}\frac{A^1_\mu - iA^2_\mu}{2} \\ +i\frac{v}{\sqrt{2}}\frac{gA^3_\mu - g'B_\mu}{2} \end{pmatrix} \tag{3.18}$$

and thus one can read the mass terms from the Lagrangian (3.14) as follows

$$W^\pm_\mu = \frac{A^1_\mu \mp iA^2_\mu}{\sqrt{2}}, M_W = \frac{1}{2}gv, Z^0_\mu = \frac{gA^3_\mu - g'B_\mu}{\sqrt{g^2+g'^2}}, M_Z = \frac{1}{2}v\sqrt{g^2+g'^2},$$
$$A_\mu = \frac{g'A^3_\mu + gB_\mu}{\sqrt{g^2+g'^2}}, M_A = 0 \tag{3.19}$$

as consequence that $SU(2) \times U(1)$ is spontaneously broken down to $U(1)$ where the photon is massless. Actually, a more adequate parameterization of Higgs field reads

$$\Phi(x) = e^{\tau^a t^a} \begin{pmatrix} 0 \\ \frac{v+h(x)}{\sqrt{2}} \end{pmatrix} \tag{3.20}$$

where the τ^a provides the longitudinal degrees to the $W^\pm$ and Z^0 fields. The SM provides three relations of importance

$$sin\theta_W = \frac{g'}{\sqrt{g^2+g'^2}}, cos\theta_W = \frac{g}{\sqrt{g^2+g'^2}}, \mathrm{t}g\theta_W = \frac{g'}{g}. \tag{3.21}$$

SM also predicts the important relation between masses and the mixing angle,

$$\rho = \frac{M^2_W}{M^2_Z \mathrm{cos}^2\theta_W} = 1. \tag{3.22}$$

Even though there is not experimental evidence of the existence of Higgs boson, the SM is a successfully theory as demonstrated in the LEP experiments: M_Z=91.1875 $\pm$ 0.0021 GeV, Γ_Z = 2.4952 $\pm$ 0.0023 GeV, M_W = 80.426 $\pm$ 0.034 GeV, Γ_W = 2.139 $\pm$ 0.069 GeV $\sin 2\theta_W = 0.23113 \pm 0.00015$, and others results presented in the Particle Data Group (PDG) [E$^+$04].

3.2 Necessity of Going Beyond Standard Model

One of the most critical points in the SM is related to loops and high order corrections. In the language of Feynman graphs, when the Higgs propagator is corrected by a Dirac fermion loop, the correction to the Higgs squared mass is

$$\Delta m_H^2 = \frac{\lambda_f^2}{16\pi^2}\left[-2M_{\rm UV}^2 + 6m_f^2 ln(M_{\rm UV}/m_f) + ...\right] \tag{3.23}$$

where λ_f is the coupling of the fermion to the Higgs. It is obvious that the squared nature of coupling or λ_f^2 comes from the two vertices as depicted in left-side of Fig. 3.1. Here $M_{\rm UV}$ is interpreted as the ultraviolet cutoff. Immediately, one can conclude that m_H^2 is sensitive to the largest mass scales. For instance when $M_{\rm UV} \approx M_{Planck}$ one gets

$$\frac{|m_H^2|}{M_{\rm Planck}^2} \leq 10^{-32} \tag{3.24}$$

the well-known Hierarchy problem.

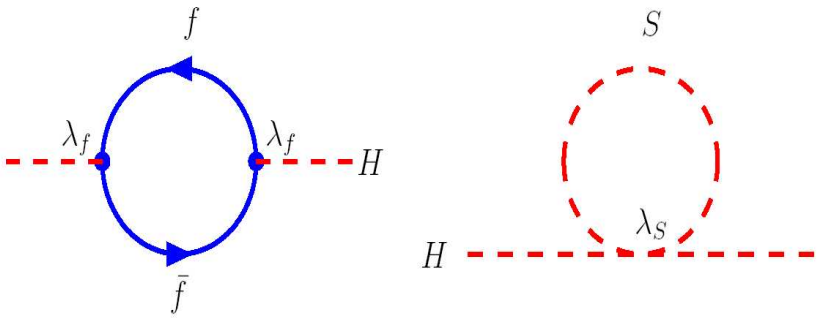

Figure 3.1: One-loop correction to the Higgs mass parameter m_H^2, due to (left) Dirac fermion f, and (right) a scalar S.

To complete the idea, let us now to consider the case when the Higgs acquire a correction through a scalar as shown in right-side of Fig. 3.1. There appears one vertice which couples the scalar S to the Higgs by means λ_S,

$$\Delta m_H^2 = \frac{\lambda_S}{16\pi^2}\left[M_{\rm UV}^2 - 2m_S^2 ln(M_{\rm UV}/m_f) + ...\right] \tag{3.25}$$

Even though for indirect couplings the problem still persists. Hence one can say that for either direct or indirect coupling of the Higgs boson to very heavy particles gives a non-sense large contribution to m_H^2. However, the cancellation of loop corrections to the Higgs mass squared is possible if one

appeal to principles of symmetry. In other words both fermion and boson loops give corrections of opposite signs,

$$\Delta m_H^2 = -\frac{\lambda_f^2}{16\pi^2}(2M_{\mathrm{UV}}^2 + ...) \qquad (fermion),$$
$$\Delta m_H^2 = +\frac{\lambda_S}{16\pi^2}(M_{\mathrm{UV}}^2 + ...) \qquad (scalar), \tag{3.26}$$

and the cancellation occurs only if it is attributed to a Supersymmetry between bosons and fermions

$$Q|boson>=|fermion> \qquad Q|fermion>=|boson> \tag{3.27}$$

being the theory discovered by Volkov (former Sovietic Union) and Ramond (USA) during the first years of the 70s. Supersymmetry or SUSY has its cornerstone in the algebra defined by the anticommutation of the momentum P_μ and fermionic operators Q_α,

$$\{Q_\alpha, Q_\beta\} = 2\sigma^\mu_{\alpha\beta} P_\mu, \tag{3.28}$$

where σ the Pauli matrices. SUSY is also the maximal possible extension of the Lorentz group and is the only symmetry of S-matrix that combines particles of different spins. SUSY joints scalar and spinorial Lagrangians in a sole picture. The most general Lagrangian involves of course additional terms of interaction

$$\mathcal{L} = i\bar{\psi}_i\gamma_\mu\partial^\mu\psi^i + |\partial_\mu\phi^i|^2 - |\frac{\partial W}{\partial\phi^i}|^2 - \frac{1}{2}\frac{\partial^2 W}{\partial\phi^i\partial\phi^j}\bar{\psi}^i\partial\psi^j + h.c \tag{3.29}$$

where W is called the Superpotential and is a polynomial function of fields. The SUSY Lagrangian contains 124 free parameters and it seems to be out of control because the almost impossibility of getting a comprehension of the phenomenology of the theory. Instead, exist there valid assumptions leading to the MSSM and Supergravity models.

3.3 The MSSM

Some authors [Mar05] have pointed out that the way to make a realistic SUSY model should take into account the following steps,

- Choose the $SU(3) \times SU(2) \times U(1)$ group symmetry.
- Choose a superpotential W by which it should be invariant under gauge symmetry.

- Choose a soft SUSY-breaking Lagrangian in order to break SUSY spontaneously.

This recipe is just applied to the MSSM that is a strict SUSY extension of the SM. It assumes that the R-parity $R = (-1)^{3(B_L)+2S}$ is conserved. Exist there some consequences about the conservation of this quantum number. Firstly, if $R = -1$ then the called "Lightest Supersymmetric Particle" or LSP must be stable. If the LSP is neutral it can certainly be an attractive candidate for cold dark matter in universe. Secondly, it should be expected in collider that the superpartners are produced in pairs. Third, each superpartner should decay in a state that contains at least a LSP.

Thus, we take a $SU(3) \times SU(2) \times U(1)$ Lagrangian and we include soft terms in order to break the symmetry of SUSY. Thus the Lagrangian reads,

$$\begin{aligned}\mathcal{L} = -m_{H_d}^2|H_d|^2 - m_{H_u}^2|H_u|^2 + \mu B\epsilon_{ij}(H_d^i H_u^j + h.c.) \\ -\frac{1}{2}M_1\tilde{B}\tilde{B} - \frac{1}{2}M_2\tilde{W}\tilde{W} - \frac{1}{2}M_3\tilde{g}\tilde{g} \\ -M_{\tilde{Q}}^2(\tilde{u}_L^*\tilde{u}_L + \tilde{d}_L^*\tilde{d}_L) - M_{\tilde{U}}^2 u_R^* u_R - M_{\tilde{D}}^2\tilde{d}_R^*\tilde{d}_R \\ -M_{\tilde{L}}^2(\tilde{\ell}_L^*\tilde{\ell}_L + \tilde{\nu}_L^*\tilde{\nu}_L) - M_{\tilde{E}}^2\tilde{\ell}_R^*\tilde{\ell}_R \\ -\epsilon_{ij}(-\lambda_u A_u H_u^i\tilde{Q}^j\tilde{u}_R^* + \lambda_d A_D H_d^i\tilde{Q}^j\tilde{d}_R^* + \lambda_l A_E H_d^i\tilde{L}^j\tilde{\ell}_R^*)\end{aligned} \tag{3.30}$$

where the objects Q, L, H_u, H_d are identified as the $SU(2)$ weak doublets. It is important to recall that the Higgsino mass μ has a mass of order of SUSY breaking masses. The breaking of the electroweak sector is due to the Higgs mechanism again but by requiring two Higgs doublets. To be more precise we write down the Higgs potential

$$\begin{aligned}V_{\mathrm{H}iggs} = (m_{H_d}^2 + \mu^2)|H_d|^2 + (m_{H_u}^2 + \mu^2)|H_u|^2 - B\mu(\epsilon_{ij}H_d^i H_u^j + h.c.) \\ +\frac{1}{8}(g^2 + g'^2)(|H_d|^2 - |H_u|^2)^2 + \frac{1}{2}g^2|H_d^{i*}H_u^i|^2\end{aligned} \tag{3.31}$$

which allows to break both SUSY and the electroweak sectors. Therefore species with the same quantum numbers appear to be mixed. For example, the charginos are composed by winos and Higgsinos, whereas the neutralinos by neutral Higgsinos, photinos and zinos. In the following we shall very briefly describe some of the superpartners of importance in this thesis.

Fields	**Spin-0**	**Spin-1/2**	$SU(3) \times SU(2) \times U(1)$
squarks, quarks	$\tilde{Q} = (\tilde{u}_L, \tilde{d}_L)$	$Q = (u_L, d_L)$	(3,2,1/6)
	$\tilde{u}^*_R$	$\bar{u}_R$	$(\bar{3}, 1, -2/3)$
	$\tilde{d}^*_R$	$\bar{d}_R$	$(\bar{3}, 1, 1/3)$
sleptons, leptons	$\tilde{L} = (\tilde{\nu}, \tilde{e}_L)$	$L = (\nu, e_L)$	(1,2,-1/2)
	$\tilde{e}^*_R$	$\bar{e}_R$	(1,1,1)
Higgs, Higgsinos	$H_u = (H^+_u, H^0_u)$	$\tilde{H}_u = (\tilde{H}^+_u, \tilde{H}^0_u)$	(1,2,1/2)
	$H_d = (H^0_d, H^-_d)$	$\tilde{H}_d = (\tilde{H}^0_d, \tilde{H}^-_d)$	(1,2,-1/2)

Fields	**Spin-1/2**	**Spin-0**	$SU(3) \times SU(2) \times U(1)$
gluino,gluon	$\tilde{g}$	g	(8,1,0)
winos, W's	$\tilde{W}^{\pm}, \tilde{W}^0$	$W^{\pm}, W^0$	(1,3,0)
bino, B	$\tilde{B}$	B	(1,1,1)

Table 3.1: MSSM particles and its corresponding group symmetry. (Taken from Ref. [ATL99]).

3.3.1 Charginos

The charginos are defined as the physical states composed of winos and higgsinos. The mass term can be written as

$$\mathcal{L}_{m_{\tilde{\chi}^{\pm}}} = -\frac{1}{2}(\psi_L, \psi_R) \begin{pmatrix} 0 & X^{\dagger} \\ X & 0 \end{pmatrix} \begin{pmatrix} \psi_L \\ \psi_R \end{pmatrix} + h.c \tag{3.32}$$

where X is a 2×2 mass matrix defined as

$$X = \begin{pmatrix} M_2 & \sqrt{2}M_W sin\beta \\ \sqrt{2}M_W cos\beta & \mu \end{pmatrix} \tag{3.33}$$

$\psi_{L,R}$ denotes the spinor composed of winos and higgsinos, M_2 is the mass of the gaugino, β is given by the definition of tanβ, the ratio between the expectation values of two Higgs fields in their ground states, and μ is the parameter of the Higgs potential. The real physical states (or observables) are obtained following a diagonalization procedure

$$UXU^{-1} = \begin{pmatrix} m_{\tilde{\chi}_1^{\pm}} & 0 \\ 0 & m_{\tilde{\chi}_2^{\pm}} \end{pmatrix} \tag{3.34}$$

which leads to the following expression for the masses of the charginos

$$m_{\tilde{\chi}_{1,2}^{\pm}} = \frac{1}{2}\left(\sqrt{(M_2-\mu)^2 + 2M_W^2(1+sin2\beta)} \mp \sqrt{(M_2+\mu)^2 + 2M_W^2(1-sin2\beta)}\right) \tag{3.35}$$

3.3.2 Neutralinos

The neutralinos are objects that are mixtures of the neutral higgsinos $\tilde{H}_1^0$, $\tilde{H}_2^0$, the photino, and the zino. In this case the mass term is written as

$$\mathcal{L}_{m_{\tilde{\chi}^0}} = -\frac{1}{2}\psi_0^{\dagger,i} Y^{ij} \psi_{0,j} + h.c \tag{3.36}$$

with $\psi_0^{\dagger} = (-i\tilde{\gamma}, -i\tilde{Z}, H_1 cos\beta - H_2 sin\beta, H_1 sin\beta + H_2 cos\beta)$. The mass matrix reads

$$Y = \begin{pmatrix} c_W^2 M_1 + s_W^2 M_2 & -c_W s_W (M_1 - M_2) & 0 & 0 \\ -c_W s_W (M_1 - M_2) & c_W^2 M_1 + s_W^2 M_2 & M_Z cos\beta & -M_Z sin\beta \\ 0 & M_Z cos\beta & 0 & \mu \\ 0 & -M_Z sin\beta & -\mu & 0 \end{pmatrix} \tag{3.37}$$

where $c_W = M_W/M_Z$, $s_W = \sqrt{1 - M_W^2/M_Z^2}$, M_1 is the gaugino mass, and tanβ already defined. Again, the physical states are available from a diagonalization procedure $NYN^{-1} = \text{diag}(m_{\tilde{\chi}_1^0}, m_{\tilde{\chi}_2^0}, m_{\tilde{\chi}_3^0}, m_{\tilde{\chi}_4^0})$, with a hierarchy among the masses. The $\tilde{\chi}_1^0$ has the lowest mass. In some scenarios, as for example in models with gravity involved, this particle is a candidate for dark matter in the universe.

3.3.3 Sfermions

The Lagrangian which describes the sfermions in the MSSM has the form $-\frac{1}{2}\bar{f}M_{\tilde{f}}f$ and explicitely reads

$$\mathcal{L}_{m_{\tilde{f}}} = -\frac{1}{2}(\tilde{f}_L^*, \tilde{f}_R^*) \begin{pmatrix} M_{\tilde{f}_L}^2 + m_f^2 + \xi_a & \xi_1 \\ \xi_1^* & M_{\tilde{f}_R}^2 + m_f^2 + \xi_b \end{pmatrix} \begin{pmatrix} \tilde{f}_L \\ \tilde{f}_R \end{pmatrix}, \quad (3.38)$$

where $\xi_a = M_Z^2 cos\beta(I_3^f - e_f s_W^2)$, $\xi_b = M_Z^2 cos\beta(e_f s_W^2)$, $\xi_1 = m_f(A_f - \mu tan\beta)$, and $\xi_1^* = m_f(A_f^* - \mu tan\beta)$. A_f is a scalar quantity, e_f is the corresponding charge of the fermion, and I_3^f is the third component of the weak isospin. The diagonalization

$$D_{\tilde{f}} = U_{\tilde{f}} M_{\tilde{f}} U_{\tilde{f}}^{-1} = \begin{pmatrix} m_{\tilde{f}_1}^2 & 0 \\ 0 & m_{\tilde{f}_2}^2 \end{pmatrix} \quad (3.39)$$

yields the following masses:

$$m_{\tilde{f}_{1,2}}^2 = \frac{1}{2}(M_{\tilde{f}_L}^2 + M_{\tilde{f}_R}^2) + \frac{1}{2}M_Z^2 cos\beta T_f^3 + m_{\tilde{f}}^2 \pm \frac{1}{2}\sqrt{(M_{\tilde{f}_L}^2 - M_{\tilde{f}_R}^2 + M_Z^2 cos\beta(T_f^3 - 2e_f s_W^2))^2 + 4m_f^2(A_f - \mu tan\beta)^2} \quad (3.40)$$

Now, the connection between the chiral partners $\tilde{f}_L$ and $\tilde{f}_R$ and the mass states $\tilde{f}_1$ and $\tilde{f}_2$ is given by

$$\begin{pmatrix} \tilde{f}_1 \\ \tilde{f}_2 \end{pmatrix} = \begin{pmatrix} cos\theta_{\tilde{f}} & sin\theta_{\tilde{f}} \\ -sin\theta_{\tilde{f}} & cos\theta_{\tilde{f}} \end{pmatrix} \begin{pmatrix} \tilde{f}_L \\ \tilde{f}_R \end{pmatrix} \quad (3.41)$$

with

$$cos\theta_{\tilde{f}} = \frac{-m_f(A_f - \mu tan\beta)}{\sqrt{(M_{\tilde{f}_{LL}}^2 - m_{\tilde{f}_1}^2)^2 + M_{\tilde{f}_{LR}}^4}}, sin\theta_{\tilde{f}} = \frac{M_{\tilde{f}_{LL}}^2 - m_{\tilde{f}_1}^2}{\sqrt{(M_{\tilde{f}_{LL}}^2 - m_{\tilde{f}_1}^2)^2 + M_{\tilde{f}_{LR}}^4}}. \quad (3.42)$$

where the quantities $M_{\tilde{f}_{LL}}^2$ and $M_{\tilde{f}_{LR}}^2$ are the matrix elements given at the 2×2 matrix mass $M_{\tilde{f}}$ (3.38).

3.4 Simplified Supersymmetric Models

Certainly, it is not realistic an exploration of the full parameter space of the complete SUSY Lagrangian neither the MSSM. In order to make predictions, one must to assume some facts being the most logical that of SUSY must be broken spontaneously. Even though this SUSY breaking does not seem to be possible when only MSSM fields are used. Thus, there is a necessity of introducing a hidden sector to break SUSY by allowing the communication between the breaking and the MSSM sector by using the messenger associated. An example is the model where gravity plays the role of messenger. If SUSY is broken in the hidden sector, then the MSSM soft terms is of order of

$$m_{soft} \sim \frac{< F >}{M_P} \tag{3.43}$$

where $< F > \sim 10^{22}$ GeV^2 and $M_P \sim 2.4 \times 10^{18}$ GeV. Therefore one expects to have m_{soft} of order of a few hundred GeV. We turn to write down an effective field theory non-renormalizable Lagrangian that couples F to the MSSM scalar fields ϕ_i and gauginos λ^a [Mar05],

$$\begin{aligned}\mathcal{L} = &-\left(\frac{f^a}{2M_P} F\lambda^a\lambda^a + c.c.\right) - \frac{k_i^j}{M_P^2} FF^*\phi_i\phi^{*j} \\ &-\left(\frac{\alpha^{ijk}}{6M_P} F\phi_i\phi_j\phi_k + \frac{\beta^{ij}}{2M_P} F\phi_i\phi_j + c.c.\right).\end{aligned} \tag{3.44}$$

This piece appears in the fully supersymmetric Lagrangian which describes Supergravity. From it, is easy to recognize masses and couplings as follows

- gaugino masses: $M_a = f^a < F > /M_P$,
- scalar squared masses: $(m^2)_j^i = k_i^j| < F > |^2/M_P^2$, $b^{ij} = \beta^{ij} < F > /M_P$, and
- scalar couplings $a^{ijk} = \alpha^{ijk} < F > /M_P$.

Interestingly, a dramatic simplification happens if the underlying supergravity theory is restringed in its gauge and kinetic interactions. It means that $f^a = f$ for all gauge interactions, $k_i^j = k\delta_i^j$ for all scalars, and $\alpha^{ijk} = \alpha y^{ijk}$ and $\beta^{ij} = \beta M^{ij}$ for couplings. It permits that the MSSM can solely be expressed in 4 parameters,

- a common gaugino mass $m_{1/2} = f\frac{<F>}{M_P}$,
- a common scalar squared mass $m_0^2 = k\frac{|<F>|^2}{M_P^2}$,

- a scalar coupling $A_0 = \alpha \frac{<F>}{M_P}$, and
- a scalar mass prefactor $B_0 = \beta \frac{<F>}{M_P}$

which is often called "Minimal Supergravity" or mSUGRA. In Fig. 3.2 an example of universality in the high scale is plotted [Mar05]. Of course, there is not a robust argument of why it is too simple in its formulation but it have been used for testing SUSY in colliders. The preparatives for physics studies at LHC and ILC have demanded to set a few scenarios in order to assess collider capabilities. In particular, the mSUGRA model containing m_0 denoting the common scalar mass at the high scale, $m_{1/2}$ the common gaugino mass at the high scale, A_0 the common trilinear coupling, tanβ the ratio between two Higgs doublets in the ground state, and signμ the sign of Higgs mixing parameter, provides testable scenarios and invaluable information about the prospects for detection of superpartners which might be gained. The most used scenarios are those called SPS (Snowmass Points and Slopes) in their types 1a and 1a'. In table 3.2 the models to be used throughout this thesis are specified. The generated mass spectra and widths of these

	tanβ	$m_{1/2}$	m_0	A_0	signμ
SPS1a	10	250	100	-100	> 0
SPS1a'	10	250	70	-300	> 0

Table 3.2: SPS scenarios and the values of their parameters.

scenarios are obtained from various codes such as `PYTHIA` [S$^+$01], `ISAJET` [P$^+$03] and `SPheno` [Por03]. The different methods used in the calculation of the mass spectra yield a little discrepancy of order of 1% (average) among the codes. However, the Monte Carlo studies are aimed to assess detector capabilities and test precision measurement of the expected new particles: "how much precise might be the measurement of the particle X under certain circumstances", for example.

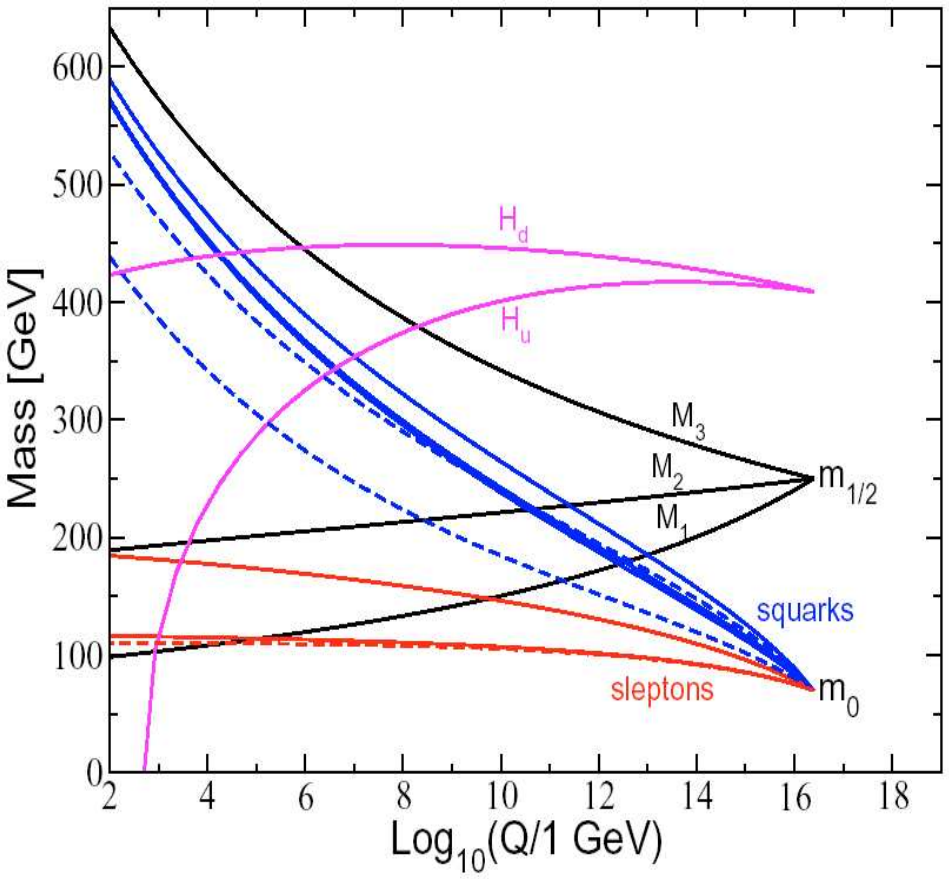

Figure 3.2: Convergence of the masses at the high scale in SUGRA models. M_1, M_2, M_3 and H_u, H_d denote the gaugino and Higgs masses, whereas the lines converging to m_0 and $m_{1/2}$ denote the masses of the different species (sleptons or squarks) evolving from the low to the high scale [Mar05].

Chapter 4

The ILC Detector

4.1 The Detector Concept

Thanks to the efforts of the linear collider community, various technical aspects concerning the performance of a detector for the next generation of e^+e^- colliders for energies up to 800 GeV, have been enormously clarified because the early proposals such as TESLA (Germany), NLC (United States) and JLC (Japan) which have contributed to have a better understanding in all technical details. It is well reflected in the recent Reference Design Report [B$^+$07] which have also incorporated all those results presented in the ECFA-DESY Workshops, Conferences and other meetings as well as those results published as LC-notes during the years 2000-2007.

During the last ten years, world wide studies have demonstrated the excellent functionality of the most crucial components of the future ILC detector through simulations and in some cases experimental studies. Although some aspects from the LEP detector have been taken into account the performance of a ILC detector is much more ambitious as is explained at the TESLA Technical Design Report [A$^+$01] and now at the Reference Design Report [B$^+$07], where a technologically robust detector to fulfill the requirements to discover and measure the Higgs boson mass and test new physics is envisaged. Actually the main priority is to find evidence of the existence of Higgs boson, the particle which is responsible for generation of mass, by means the its couplings to known SM species. The SM predicts that the observation of Higgs boson might be through the reactions:

- $e^-e^+ \to Z^0h$ at $\sqrt{s}_{e^+e^-} = 250$ GeV,
- $e^-e^+ \to Z^0hh$ at $\sqrt{s}_{e^+e^-} = 500$ GeV, and
- $e^-e^+ \to t\bar{t}h$ at $\sqrt{s}_{e^+e^-} = 800$ GeV.

Therefore there is a clear compromise in to develop carefully certain components aimed to have an excellent capabilities for detection of reconstruction of jets and stable leptons what are derived from the Z^0 boson and the t quark. A few details of the main components will be described below. Since the HEP literature offers a wide spectrum of excellent references aimed to describe the basics of the ILC detector, we follow that description given in Ref. [Tho06].

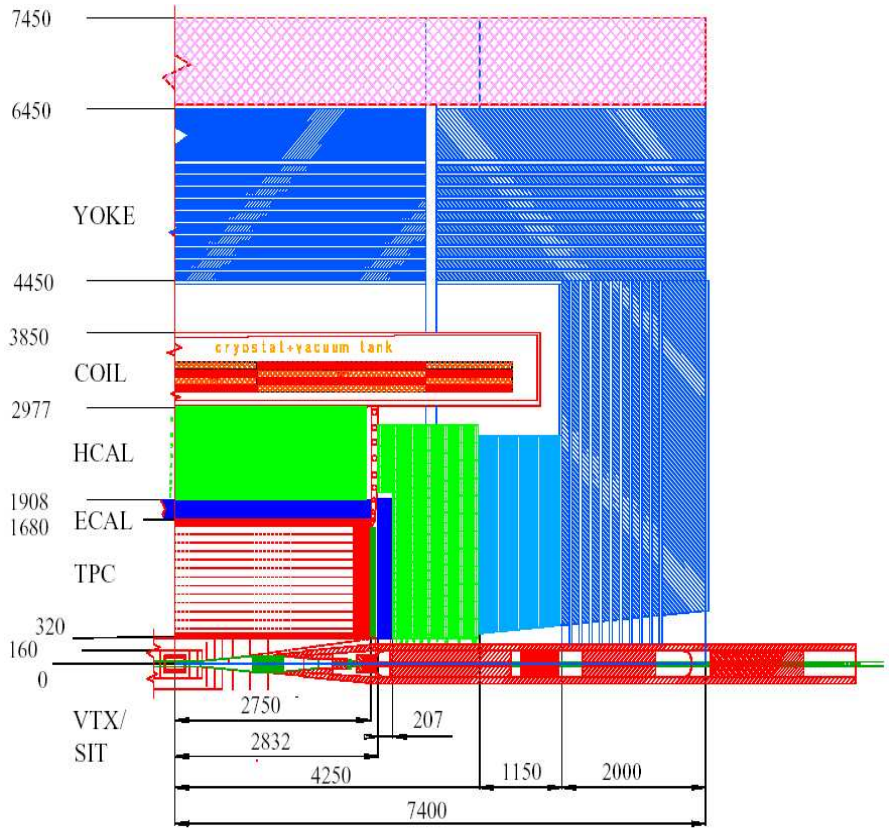

Figure 4.1: Cross transversal of one quarter of the ILC (TESLA) detector.

4.1.1 The Tracking System

A precise Higgs boson mass measurement implies to have a very good track momentum resolution better than those used in the past. Independently of its decays, the searching of Higgs boson through the $e^+e^- \rightarrow hZ^0 \rightarrow h\ell^+\ell^-$ processes represent a promising direction towards a measurement of the recoil mass by means the $\ell^+\ell^+$ pairs. In order to guarantee the physics accomplishments, the ILC tracking system would consist in the following,

- the Forward Tracker Disks (FTD),
- the Silicon Intermediate Tracker (SIT)
- a large Time Projector Chamber (TPC), and
- the forward chambers.

Tracking Resolutions

At the ILC, one can perform precision measurements of the various sectors of SM and SUSY Lagrangians. Recent studies have predicted that the Higgs boson mass can be well measured via the recoil mass method within a precision of $\delta M_{\ell^+\ell^-} = 0.1$ GeV [W$^+$07a]. Under this perspective, excellent precision on the tracking components of ILC detector is mandatory. Thus, a central tracking resolution of $\delta\ (\frac{1}{p_T}) \leq 5 \cdot 10^{-5}(GeV)^{-1}$ a and magnetic field ≥ 4T and a large tracking volume are required. Also, a forward tracking resolution of $\delta\ (\frac{1}{p_T}) \leq 3 \cdot 10^{-4}(GeV)^{-1}$ is desirable. It is important to note that the inherent presence of an enormous amount of tracks at very low angles down to 80 mrad and the compromise in to reach a precise measurement of the luminosity an angular resolution of $\delta\theta \leq 2 \cdot 10^{-5}$ rad is foreseen.

4.1.2 Vertexing

The main role of a ILC detector is the identification of those species which would reconstruct the Higgs boson mass and other properties. Thus the principal task of a vertex detector would consist in to distinguish the Higgs decays: $h \to c\bar{c}$, $h \to b\bar{b}$, $H \to g\bar{g}$ and $h \to \tau\bar{\tau}$. Moreover, if SUSY exist in nature the e^-e^+ collider might be a factory of superpartners only if the SUSY masses are ranging between 200 GeV and 300 GeV. Here, the vertex detector would play the role in identifying the $e^+e^- \to \tilde{t}_1^+\tilde{t}_1^-$ reactions which would be reconstructed by means the $\tilde{t}_1 \to b\tilde{\chi}^+ \to bW^+\tilde{\chi}_1^0$ decays, only if b tagging is allowed. To achieve these goals, an impact parameter resolution of order of 5 μm is needed. In general terms, the ILC vertex detector demands the inclusion of a multilayered Si-based pixel detector, an innermost layer very closely to the IP and, a large selenoide field to retain inherent backgrounds species.

The Vertex Detector

A possible configuration of vertex detector would consist in a silicon pixel detector composed by 5 layers, with a radius ranging between 1.6 cm (from

the IP) and 6.0 cm. The technology to be used is still under study, being the most promising CMOS and CCD. In all cases the net number of pixels can reach more than 500 million. The Fig. 4.1 displays a possible layout of vertex detector.

4.1.3 Energy Flow

Multiparton final states represents a via for testing new physics at ILC energies. Their identification requires the application of sophisticated techniques such as the energy flow concept based on the experience of LEP. To be able to deduce the original parton four-momentum, the combination of the acquired information from the tracking and calorimetry is needed for a robust estimate of the flow of particles. Concretely, the applicability of the energy flow concept will allow us the separation of species per event within an excellent resolution.

The Particle Flow Concept

The identification of single jets imposes serious challenges towards the full reconstruction of Higgs particle and other signals of new physics. The most adequate way which encompasses these requirements is the usage of particle flow algorithm in where information of both Electromagnetic Calorimeter (ECAL) and Hadronic Calorimeter (HCAL) are joined to a complete reconstruction of four momentum of species accounted. According to the LEP, a rough estimated about the composition of jets would be

- 62% of the energy is carried by charged particles,
- 27% by photons,
- 10% by long-lived neutral hadrons, and
- 1.5% by neutrinos.

Concerning the jet resolution, it can be estimated from the contributions from tracks, γs and neutral species yielding a resolution of around $0.19/\sqrt{E}(\mathrm{GeV})$. In praxis, this performance is degraded by various factors. One of them is linked to the impossibility of a perfect association of the deposited energy with the correct species. Thus, one needs to improve the performance of the granularity in both ECAL and HCAL.

4.1.4 Hermeticity

The searching of SUSY and extra dimensional scenarios where an important amount of missing energy is manifested requires the necessity of having a ILC detector with a good hermeticity and coverage and particle detection capabilities at small angles down to 80 mrad. The two-photon processes, a dangerous background for slepton studies demand us the inclusion of a forward detector expected to improve the SUSY signal statistics. In this thesis we shall emphasize this necessity which is translated to have an efficient discrimination of these processes and to improve the signal purity. The role of a forward detector is beyond the searching of new physics. A stringent point is the measuring of the luminosity via Babha scattering which normally is performed at low angles. Recent achievements concerning the forward detector can be found in Ref. [Kou07].

4.1.5 The Electromagnetic Calorimeter

The task of a ECAL is that of measuring the energy of photons and electrons and to separate the electromagnetic species from the hadronic ones. According to the TDR the existing options are,

- a very high granularity 3D calorimeter, based on tungsten absorbers and silicon diode pads. A remarkable point is that of the functionality of Si-W calorimeter which encompasses the energy flow concept.
- a shashlik calorimeter consisting in sampling calorimeters where the scintillation light is read-out by means the wavelength shifting fibers.

The relevant quantities of importance for the material to be used in a ECAL are λ_I and L_{X0}. It is useful to compare the values for the iron, the tungsten and the lead,

material	λ_I (cm)	L_{X0} (cm)	λ_I/ L_{X0}
Fe	16.8	1.76	9.5
W	9.6	0.35	27.4
Pb	17.1	0.56	30.5

Table 4.1: Some material parameters taken from Thompson's work [Tho06]

An ECAL made of silicon-tungsten with 1.0 cm^2 cell size and 32 million channels and a high granularity, is desired. It is translated in to gain a resolution of

$$\frac{\sigma_E}{E} \leq 1\% + \frac{10\%}{\sqrt{E\mathrm{G}eV}}. \tag{4.1}$$

4.1.6 The Hadronic Calorimeter

The HCAL should be suited behind the ECAL and its main task in that of measuring the energy as well as angles of hadrons and jets by allowing the tracking of ionized particles inside the calorimeter volume. On the other hand, for optimization of the energy flow measurement the HCAL

- should contain the hadronic shower,
- to allow a precise determination of the deposited energy,
- to allow the separation of close by cluster by means a high granularity along the transverse and longitudinal direction,
- should be able to measure the time of events, and
- to help to reject cosmic events.

The TDR have launched two approaches for a HCAL. The first one, a tile hadronic calorimeter of moderate segmentation is a sampling calorimeter made of stainless iron and scintillating tiles of 5×5 cm^2 cell size and an energy resolution (per hadron)

$$\frac{\sigma_E}{E} \leq 3\% + \frac{35\%}{\sqrt{E\mathrm{GeV}}}. \tag{4.2}$$

On the other hand, the second one a highly segmented digital hadronic calorimeter with a highly granularity by which a refined description of the interactions will be possible. This approach serves to separate muons and pions at low energies down to 1 GeV.

4.1.7 Magnet and Muon Identification

The resolution of momentum at the ILC depends on the magnetic field, therefore a resolution of 5 10^{-5}(1/GeV) can be possible if a magnetic field of 4 T surrounds the whole calorimetry. It is important to note that the ILC magnet system have adopted the Compact Muon Selenoide (CMS) technology. The functionality of the muon system is derived from the magnet system, it is the iron return yoke of the magnet system and its instrumentation based on resistive plate chambers. In essence, the main task of a muon detector is to identify muons and perform momentum measurements for penetrating particles. A secondary task of muon detector is the tail catching of those hadronic showers not contained in calorimeters. As we shall see later, a minimum muon energy of 5 GeV is guaranteed for the ILC design.

Chapter 5

Prospects For Right-Handed Smuon Mass Measurement at the ILC

5.1 Introduction

This chapter is devoted to test SUSY at the future ILC. Our plan consist in to perform a simulation of right-handed smuon production aimed to assess the reconstruction of the $\mu^-\mu^+\mathrm{E}^{miss}$ final states that represents an invaluable window to measure the smuon mass (and other sparticles). Starting from the assumption in where $\tilde{\mu}_R^+\tilde{\mu}_R^-$ pairs can be copiously created in virtue of R-parity conservation, for models whose mass spectra are ranging over the electroweak scale the production of smuon basically the right-handed ones, are expected to be observed and their masses might be measured within a respectable precision. We would like also to show possible pros and cons about the reconstruction of data of smuons together with their background in a linear collider running at $\sqrt{s}$=0.5 TeV.

5.1.1 Essentials Aspects of the Simulation

The simulation procedure for the present case involves several steps. This procedure will be repeated for subsequent analysis like the smuon production in photon collisions in later chapters. It is important to specify the role of each step as well as the software to be used according to the physics.

Event Generation

First of all, the simulation procedure starts with the choice of the correct software which will be capable of generating the events in according to the machine. We will use the SPS1a' scenario based on the SPA convention [AS$^+$05]. For the case of a linear collider running at energies of 500 GeV we have decided by the following softwares

- PYTHIA [S$^+$01]: This code will be used for the right-handed smuon analysis for both signal and all background processes. It is important to note that this code needs of CIRCE [Ohl] which provides the beam parameters.

- ISAJET: [P$^+$03]: The use of this code is aimed to replace some masses of the generated spectrum by PYTHIA.

Fast Detector Simulation

Once the events are already generated, they are processed by SIMDET [Poh02] which is responsible to incorporate the expected detector effects. This code contains a file which summarizes the main detector parameters as the expected one for the ILC. SIMDET contains the subpackage SIANAL whose task is that of analyzing event by event and the subsequent storing of data in n-tuples through HBOOK [PAW95] links. SIMDET is defined as a fast simulator, in the sense that it provides the opportunity to simulate the detection of events with a "velocity" of up to 10^4 events/min (by assuming a CPU 1.7 GHz). Essentially, SIMDET treats the detector response in a realistic manner using a parametrisation of results from the Monte Carlo programme BRAHMS [Beh01b].

The Detector Parameters: The main detector parameters considered in this code are

(1) a magnetic field of 4.0 Tesla,

(2) a muon misidentification probability of 0.005,

(3) an average deposited energy of muons in the ECAL/HCAL of 3.8 GeV and a minimum energy of muons to be considered as isolated of 5.0 GeV,

(4) a TPC with an inner and outer radius of 0.362 m and 1.618 m, respectively, of 5.0 m lenght. The tracking step size within the TPC (or the $\frac{\mathrm{d}E}{\mathrm{d}x}$ tracking parameter) is taken to be 3 cm. A tracker efficiency of 0.99 is assumed, with the minimum transverse momentum of charged particles of 0.10 GeV,

(5) a tracker acceptance > 7 degrees, with the TPC acceptance > 12 degrees and a CCD vertex detector technology with an acceptance > 16

degrees. Also, an acceptance of the low angle calorimeter (LCAL) between 4.6 mrad and 27.5 mrad is required,

(6) an electromagnetic calorimeter with acceptance > 4.3 degrees. The minimum energy for $\gamma/e^{\pm}$ detection to be 0.2 GeV is required, as well as an electron misidentification probability of 0.002,

(7) the hadron calorimeter acceptance is fixed to be > 4.3 degrees, with 0.5 GeV of minimum energy of hadron detection.

Data Analysis

The n-tuples are thus analyzed in PAW [PAW95] which serves of framework to compare the signal n-tuples to its corresponding background and therefore to apply the necessary cuts. Once the signal have been cleaned, the n-tuples are projected to one dimensional histograms to further analysis.

5.2 Basics of Smuon Production at the ILC

The right-handed smuon would in reality be the first superpartner in being observed in TeV colliders. One point to be taken into account is a possible but very promising observation of this sparticle at proton-proton collisions. Actually, either observation or evidence of superpartners in a proton-proton collider differs substantially from that of an electron-positron machine. It is because in hadron collisions, the unique road to "see" smuons, or neutralinos, etc, is the reconstruction of invariant mass spectra which would display hard edges as consequence of production of superpartner in cascade. Thus the observables to be measured are the mass differences, and their measuring would be quite precise [Mon96]. But an individual identification of species is not accessible so far, or at least no any strategy to identify single smuons have been drawn.

Contrarily to hadron facilities, the e^+e^- machine would reveal direct information of SUSY particles. In this machine the right-handed smuon can be produced via $\gamma - Z^0$ exchange, since sleptons are coupled to Z_μ and A_μ fields in virtue of Lagrangian. Consequently, smuon is going to decay into invisible neutralino and an isotropic muon. In some mSUGRA models, the lightest neutralino has a mass closely to 100 GeV and its presence in SUSY models have acquired importance because it could be the key piece for understanding the darkness of universe. This sparticle escapes the detector carrying away an important amount of energy. A typical signature about the existence of the smuon have been the acoplanar production of muons accompanied of missing energy. In Fig. 5.1 is depicted the graph which is responsible of its creation

as well as its subsequent decay into muon and the lightest neutralino. Another fact of interest for us, consist in the decay of right-handed smuon. For the SPS1a point, this sparticle has a branching ratio Br($\tilde{\mu}_R \to \tilde{\chi}_1^0 \mu$) 100%, whereas for SPS1a' 90% [AS+05] [KZ06]. Theoretical studies have investi-

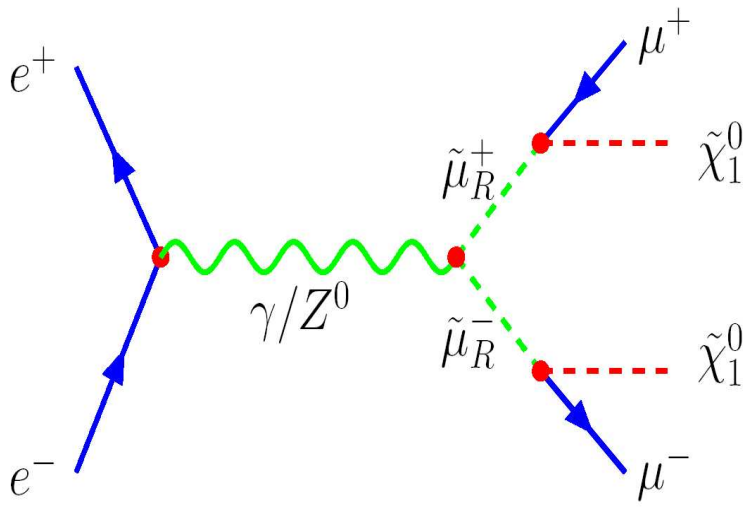

Figure 5.1: Production of $\tilde{\mu}_R^- \tilde{\mu}_R^+$ via Z^0/γ exchange followed by $\tilde{\mu}_R \to \mu \tilde{\chi}_1^0$ decays.

gated the production and smuons for current collider parameters. From these studies [F+04], the computed cross sections reads

$$\sigma[e_L^+ e_R^- \to \tilde{\mu}_R^+ \tilde{\mu}_R^-] = \frac{2\pi\alpha^2}{3s}\beta^3 \left(1 + g_i g_{L,R} \frac{s}{s - M_Z^2}\right)^2, \qquad (5.1)$$

with $i = L, R$ the left and right-chiral Z coupling $g_{\rm L} = \frac{-1+2s_{\rm W}^2}{2s_{\rm W}c_{\rm W}}$ and $g_{\rm R} = \frac{s_{\rm W}}{c_{\rm W}}$. Intrinsically, the angular distribution for smuon pair production is featured by a $sin^2\theta$ shape because both smuons are preferentially produced perpendicular to the e^+e^- beam axis. Furthermore, these cross sections also show the importance of having polarized beams. Actually the polarization of incoming beams is considered a serious topic in TDR for building the ILC. It is because the evident advantages in the searching SUSY signals. An interesting configuration contemplates P_{e^-}=0.8 and P_{e^+}= -0.6 which is desired for enhancing the smuon signal in about 100% in comparison for the case of unpolarized beams. In Fig. 5.2 various cross sections for right-handed smuons production are illustrated. Curves generally reach their maximum in around 400 GeV and for these energies σ gets 175 fb when both leptons are polarized. Therefore, polarization changes drastically cross sections and becomes a crucial ingredient for the e^+e^- collider. It gives rise to an extraordinary

production of several tens of thousands of supersymmetric particles pairs per year. A crude estimated at $\sqrt{s}$=500 GeV, and an integrated luminosity of 1000 fb^{-1}, more than 150K smuon pairs are foresee. It obviously provides enough statistics to disentangle the signal from the background without a substantial lost of signal efficiency. In the past, experiments have also paid attention for searching smuons and other superpartners. One of the well-known precursors have certainly been PETRA. In effect, during the 80s the CELLO detector collected data equivalent to 48pb^{-1} at energies $\approx$ 47 GeV. Although evidence of SUSY signals was discarded, exclusion mass domains were imposed. For instance, smuon mass had to be restringed between 2 GeV and 20 GeV [B$^+$87]. A decade later and with the advent of new technologies

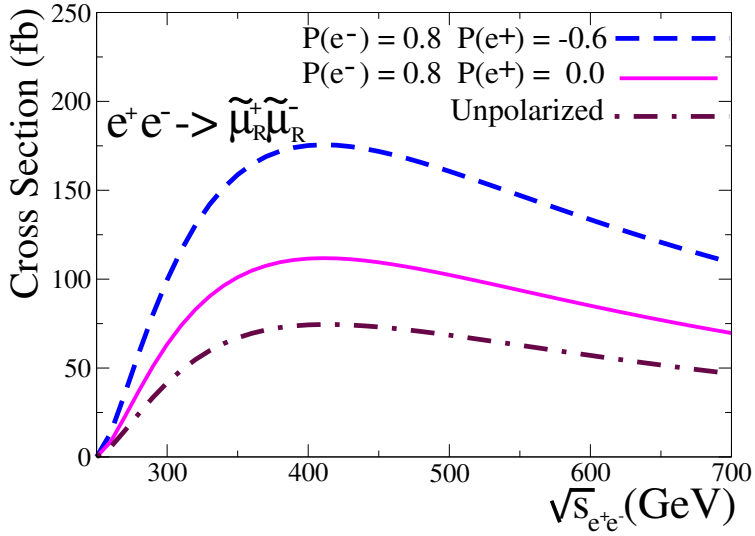

Figure 5.2: The cross section for right-handed smuons production in e^+e^- collisions for different polarization configuration is plotted under the assumption of SPS1a' scenario [AS$^+$05]. The SPheno code was used. For the P_{e^-}=0.8 and P_{e^+}= -0.6 configuration, the cross section can reach up to 175 fb at $\sqrt{s}_{e^+e^-}$=0.4 TeV.

have permitted to accelerate electron-positron pairs at LEP at energies of up to 210 GeV, having constituted an interesting arena for testing SUSY. Thus LEP have searched for smuons, staus and selectrons in the data taken during year 2000 at center-of-mass energies ranging from 204 GeV to 209 GeV [McP02]. Naturally, several SUSY theories have been evaluated, among them Gravity Mediated Supersymmetry Breaking (GMSB) model. In essence, the model contains the following parameters N_M denotes the number of messengers, M_S the messenger mass scale, Λ the effective SUSY-breaking order

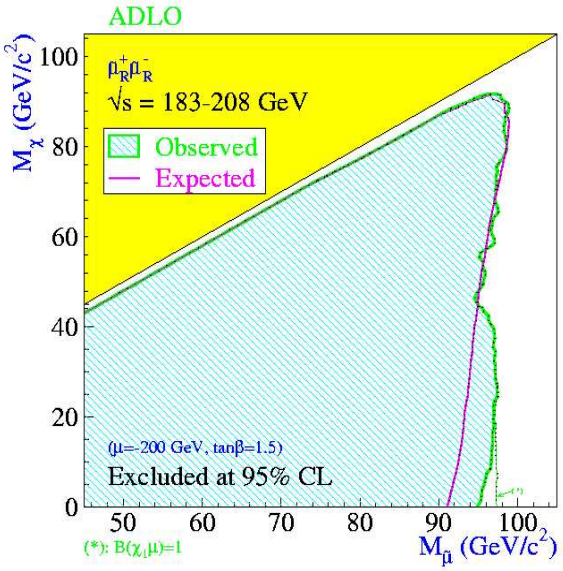

Figure 5.3: Excluded regions in slepton-neutralino mass plane obtained from LEP2 [McP02]. The regions "observated" means the experimental data which appears to be in disagree to the "expected" one based on MSSM scenarios.

parameter, tanβ and signμ. The GMSB model accepts to gravitino as the LSP. Also, sleptons can be the next lightest supersymmetry particles (NLSP) in this model. Their decay lenght is arbitrary and depends on the gravitino mass which is proportional to SUSY breaking scale. Hence LEP used various analysis to be sensitive to all ranges of slepton lifetime by searching for events containing at least two leptons plus missing energy, tracks with large impact parameter and for heavy stable charged particles. Despite that no any evidence was encountered, constrains have been derived in the context of GMSB scenario. In another approach, 2000 year data had to be combined with those taken at lower energies during the years 1999 and 1998. As result cross sections and branching rations were calculated by performing a scan over the parameters Λ (5-150 TeV), tanβ (2-50), M_S (1-10^6 TeV), N_M (1-5) and signμ (-1,+1). Slepton masses lower than 97.5 GeV have been excluded at 95% of confidence limit (C.L). In Fig. 5.3 an example of the region of "observated" data is illustrated and it does not matches the area which expected from the MSSM theory [McP02]. In this way, the next task of future accelerators would have to be the continuation of the searching of these species for energies beyond 100 GeV. Under this spirit, we present a simulation of production and subsequent decay of smuons at the e^+e^- mode, being the reconstruction of smuon mass the target. In the past, smuon studies for the former version of ILC or TESLA was pioneered by H.U Martyn [Mar04]. Our

intention here is to provide a pedagogical approach for simulation of signal together with its corresponding background and describe the neccesary steps towards a significant signal-to-background rate.

5.3 Description and Simulation of Signal

The simplicity of smuon production is appreciated in left panel of Fig. 5.4. While $\tilde{\mu}_R^+\tilde{\mu}_R^-$ particles obey the back-to-back topology, the produced muons

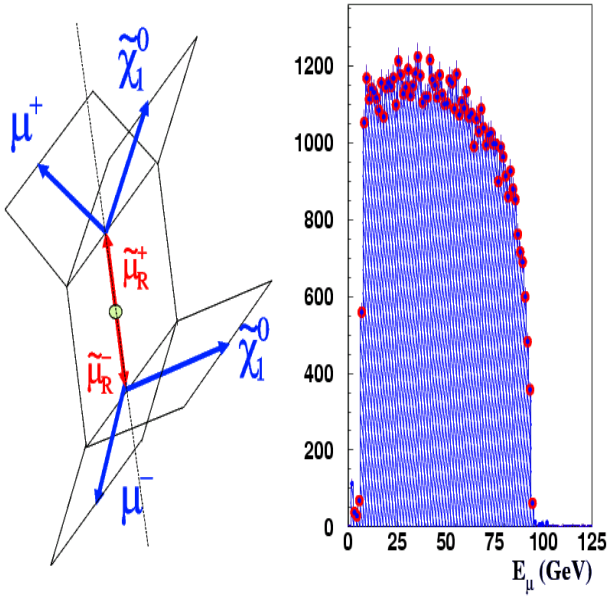

Figure 5.4: (Left) Sketch of smuon pair production. (Right) The muon energy distribution obtained at the detector level by including all radiation effects.

are acollinear and them are produced in all directions. In other words, the muons do not travel in any preferred direction because of the spin-0 smuon decays. Missing energy is another feature of these signals. It is because the $\tilde{\chi}_1^0$ neutralino is invisible to detectors and thereby carrying away an important fraction of energy. Our simulation attempts to demonstrate the feasibility in getting information of smuon kinematics from the muon energy which is a variable of enormous interest for us. Now we say a few words about the kinematics. In the laboratory system, the energy spectrum would have to have a box-like shape. But this ideal shape is not longer valid since the presence of radiation of effects would distort substantially the ideal shape. As illustration, on right panel of Fig. 5.4 is presented the energy distribution of detected

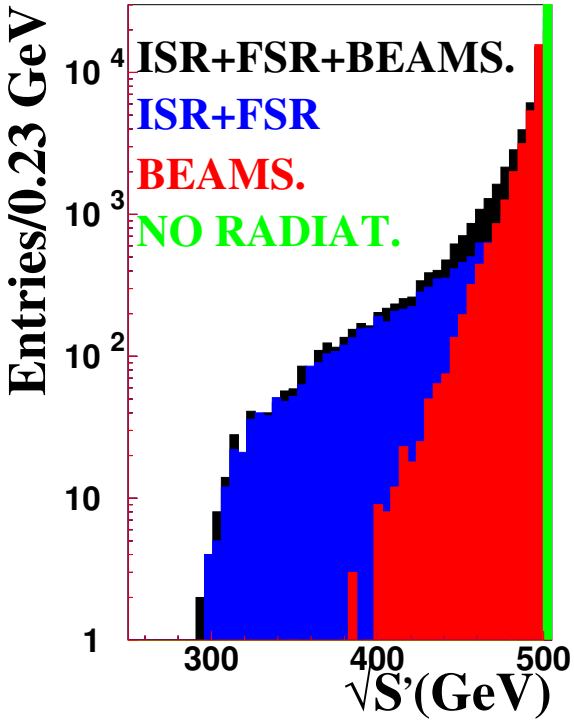

Figure 5.5: Radiation effects in e^+e^- collisions. The $\sqrt{s'}$ distribution is plotted for different levels of radiation.

muons. For this example, the SPS1a' scenario was used. The events were generated with PYTHIA [S$^+$01] interfaced with ISAJET [P$^+$03], including in parallel all mandatory radiation effects. To emulate the detection of muons in a possible ILC detector, we have used the package SIMDET where the algorithm based on the energy flow object (enflo) concept is implemented.

From the figure it is observed that the simulated energy distribution presents a trapezoidal-like distribution. Moreover the observed level of distortion is asymmetric. It should be noted that the right-side endpoint have turned to be completed damaged. Such a distortion has its origin in the following phenomena: Beamstrahlung, initial and final state radiation. While Beamstrahlung radiation damage both endpoints of spectrum, initial and final state radiations affect the right-side producing a long tail. We recall that the distortion obey to radiation phenomena rather than detector resolution.

It is interesting to compare the impact of the different radiation levels on the effective center-of-mass-energy $\sqrt{s'}$. In Fig. 5.5 we have displayed the

diverse stages of radiation in what the lepton beam suffers a notable modification before the collision. One can note the overall radiation is actually non-negligible and as consequence the energy spectrum is modified. Beamstrahlung had to be simulated with the package CIRCE2 [P$^+$03], whereas initial and final state radiation with PYTHIA. The current ILC parameters were used at Circe by allowing us to know how behaves $\sqrt{s'}$ under possible conditions of the electron-positron beams.

Turning to the signal simulation specifications, for $\sqrt{s}_{e^+e^-} = 0.5$ TeV one gets a cross section of 161 fb suggesting the simulation of 74750 signal events corresponding to one year run or 464 fb^{-1} of integrated luminosity, roughly. Since SIMDET has already incorporated to PYTHIA as generator, the next task is the creation of n-tuples PAW to store the data. As stated earlier SIMDET contains the subpackage SIANAL aimed to carry out physics analysis. Therefore, the creation of n-tuples serves also for background analysis. In the following the associated noise is considered.

5.4 The Background Processes

We define the background or noise, as those events whose topology matches that of the signal. In our case, are background events those what are characterized by two muons of opposite charge plus missing energy. The background processes have been classified in two blocks. The first one contains SM reactions and the second one are all those SUSY reactions. The SM features the off-shell two photon processes as the dominant ones. In Table 5.1 the processes and their respective channels that contribute to the background are listed. We have simulated the cross sections with PYTHIA without any cut at the phase space, except for the off-shell two photon processes by which will be explained in turn. The generation of events was given according to the product of cross section times branching ratio.

For the second block 0.5 TeV is expected an important contribution of background events derived from supersymmetric particles, because of their masses, several supersymmetric processes are kinematically allowed. For completeness, we have assumed a Higgs boson and a Top quark with masses 120 GeV and 174.3 GeV, respectively. In the SPS1a' scenario, supersymmetric phases are negligible leading to have a CP conservation. Technically speaking, 2→2 reactions were generated according to their cross sections and luminosity. Additionally the supersymmetric particles were allowed to decay according to their branching ratios. An example is the left-handed smuon. This sparticle, according to mSUGRA scenarios presents the following decay channels: $\tilde{\mu}_L \to \mu\tilde{\chi}_1^0$, $\tilde{\mu}_L \to \mu\tilde{\chi}_2^0$ and $\tilde{\mu}_L \to \nu\tilde{\chi}_1^{\pm}$, moreover both

$e^+e^- \rightarrow$ $\sigma(fb)$	Channel	$\sigma \times \mathcal{BR}$	N($\approx$ 1 Year)
W^+W^- 783.6	$\nu\mu\nu\mu$	$\sigma_{WW} \times \mathcal{BR}(W \rightarrow \mu\nu)^2$	4125
	$\nu\mu\nu\tau$	$2{\cdot}\sigma_{WW} \times \mathcal{BR}(W \rightarrow \mu\nu)$ $\times\mathcal{BR}(W \rightarrow \tau\nu) \times \mathcal{BR}(\tau \rightarrow \mu\nu\nu)$	1431
	$\nu\tau\nu\tau$	$\sigma_{WW} \times \mathcal{BR}(W \rightarrow \tau\nu)^2$ $\times\mathcal{BR}(\tau \rightarrow \mu\nu\nu)^2$	124
Z^0Z^0 575.1	$\nu\nu\mu\mu$	$2 \cdot \sigma_{ZZ} \times \mathcal{BR}(Z \rightarrow l\bar{l}) \times \mathcal{BR}(Z \rightarrow \nu\nu)$ $l = \mu, \tau$	3482
γ/Z^0 1110.0	$\mu\mu$	$\sigma_Z \times \mathcal{BR}(Z \rightarrow \mu\mu)$	500400
	$\tau\tau$	$\sigma_Z \times \mathcal{BR}(Z \rightarrow \tau\tau)$ $\times\mathcal{BR}(\tau \rightarrow \mu\nu\nu)^2$	14697
$l^+l^-(e^+e^-)$ 7000.0	$\mu\mu ee$	$\sigma(e^+e^- \rightarrow e^+e^-\mu^+\mu^-)$	3150000
	$\tau\tau ee$	$\sigma(e^+e^- \rightarrow e^+e^-\tau^+\tau^-)$ $\times\mathcal{BR}(\tau \rightarrow \mu\nu\nu)^2$	94822

Table 5.1: List of the SM background processes showing the relevant channels and number of expected events for an integrated luminosity equivalent to 1 year. In all cases, cross sections have been calculated at 0.5 TeV $\sqrt{s}_{e^+e^-}$.

neutralino and chargino are going to suffer a subsequent decay in virtue of their couplings to SM and SUSY species. PYTHIA does not performs a fully computation of final state observables; instead it computes the multiplication of cross section times branching ratio being this procedure still reasonable for the analysis.

The simulated 2→2 reactions and their respective cross sections (in brackets) and number of simulated events are

- $e^+e^- \to \tilde{\mu}_L^+\tilde{\mu}_L^-$ (16.20 fb) 7300,
- $e^+e^- \to \tilde{\tau}_1^+\tilde{\tau}_1^-$ (168.5 fb) 75850,
- $e^+e^- \to \tilde{\tau}_2^+\tilde{\tau}_2^-$ (16.92 fb) 7613,
- $e^+e^- \to \tilde{\chi}_1^+\tilde{\chi}_1^-$ (14.06 fb) 6330,
- $e^+e^- \to \tilde{\chi}_1^0\tilde{\chi}_2^0$ (17.96 fb) 8082.

Note that the $e^+e^- \to \tilde{\tau}_1^+\tilde{\tau}_1^-$ processes dominate the supersymmetric backgrounds processes. However, it was observed that the SUSY processes are characterized by having low energy muons since they suffer cascades and therefore their energies turns out to be degraded. An apart discussion deserves the photon-photon processes because of their troublesome presence in the analysis. The building of ILC detector includes a very important component, the forward detector whose main purpose is to guarantee the reconstruction of leptons such a e^+e^- pairs down to 83.1 mrad. The neccesity of this component is clearly manifested in the searching of smuons where signal is underneathed by an enormous amount of noise.

5.4.1 The 2-Photon Processes

We shall discuss some of the main physics properties of these processes instead of going in a detailed analysis. An excellent review is given in Ref [Kol84]. The purpose here is to find what is the cut which should reduce substantially the photon-photon background processes. Thus, the information obtained in this subsection will be used through the preselection of signal events. Two-photon scattering in e^+e^- linear colliders can be observed in reactions such as $e^+e^- \to e^+e^-$X. In effect, an electron and a positron radiate photons before the interaction point, which produce a particle system X. Under a QED vision, these phenomena can be well described by t- and s-channels that contribute to the $e^+e^- \to e^+e^-$X processes. The dominant one is given by the t-channel type amplitude where both electron and positron radiate two off-shell photons establishing the system X. In order to illustrate

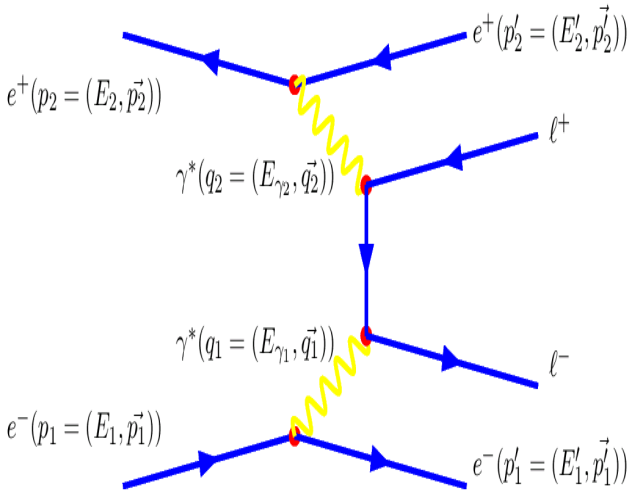

Figure 5.6: Diagram for lepton pair production by two off-shell photons.

the t-channel amplitude, Fig. 5.6 consider two virtual photons created by the electron and positron. As an example we have drawn the case when X$\rightarrow$ $\ell^+\ell^-$. However, in certain kinematical regions the "virtual bremsstrahlung processes" with negative C-parity of the final states X can also give a sizeable contribution. Due to the photon propagators in Fig. 5.6, photons are emitted predominantly at small angles, of order m_e/E with respect to the beam. It implies that a small (space-like) momentum should have to be transfered to the system X. The invariant mass of the system X peaks at small values because the photon energies follow roughly the characteristic bremsstrahlung spectrum which is in fact, proportional to $1/E$. For the inclusive detection of system X the kinematics of the $e^+e^- \rightarrow e^+e^-$X processes is determined by the four-momenta of the incoming and of the scattering electron and positron (p_1, p_2 and p_1', p_2' respectively), but at least no the internal kinematics of system X. For unpolarized beams, five variables are needed for a full determination of $\gamma\gamma$ system at a given beam energy E:

- the energies E_1', E_2' of the scattered leptons,
- their angles Θ_1, Θ_2 with respect to the beam axis,
- the angle Φ between the two lepton scattering planes.

The square masses of the (space-like) photons are $q_1^2 = -Q_1^2 = (p_1 - p_1')^2$ and $q_2^2 = -Q_2^2 = (p_2 - p_2')^2$. For $\Theta_{1,2} >> m/E$, $q_i^2 \approx -2EE_1'(1 - cos\Theta_{1,2})$. Since the scattering angles $\Theta_{1,2}$ are predominantly very small, the electron mass terms cannot always be neglected. In particular, one obtains for $\Theta_{1,2} = 0$ the minimum $Q_{1,2min}^2 \approx m^2\omega_{1,2}/(1 - \omega_{1,2})$ with $\omega_{1,2} = E_{\gamma,1,2}/E$. The invariant

mass of the $\gamma\gamma$ system for small Q_1^2 and Q_2^2 can be approximated by

$$W_{\gamma\gamma}^2 \approx 4 \cdot E_{\gamma 1} \cdot E_{\gamma 2}. \tag{5.2}$$

In general, quantities as $dN_\gamma/d\omega$ are functions of $ln(Q^2_{\mathrm{max}}/Q^2_{\mathrm{min}})$. For the case that the scattered electron is detected in an angular range $m/E << \Theta_{min} < \Theta < \Theta_{\mathrm{max}} << 1$ it is possible to write $Q^2_{\mathrm{max}}/Q^2_{min} = (\Theta_{max}/\Theta_{min})^2 = \eta^2$. Thus we can write an useful observable, the photon spectrum given by

$$\frac{dL_{\gamma\gamma}}{dz} = \frac{4\alpha^2(ln\eta)^2}{z\pi^2}\left((2+z)^2 ln(\frac{1}{z}) - (1-z^2)(3+z^2)\right) \tag{5.3}$$

where $z = \sqrt{\omega_1\omega_2}$. It is neccesary the knowledge of photon spectrum or the two photon luminosity in order to evaluate the correspondent cross section of the $e^+e^- \rightarrow \ell^+\ell^- e^+e^-$ reactions. In other words, the tree level cross section of the $\gamma\gamma \rightarrow \ell^+\ell^-$ reactions has to be convoluted together with their luminosity. Due to the presence of the $ln\eta$, the convoluted cross section turns to be huge for lepton energies at the range of 100-200 GeV, being a typical value 10^4 fb. The present work have used PYTHIA as generator of these reactions. The code provides the opportunity to handle integrations at the phase space. In effect, one of this modifications had to do with the creation of leptons pair with a transversal momenta greater than 10 GeV. Thus one obtains a cross section of about 7000 fb. We have argued that the initial lepton beams, are scattered in a small angle. From the experimental point of view, the detection of such leptons can be successfully done if update technologies allow their reconstruction. The response of a forward detector have been incorporated at the package SIMDET, whose goal is to provide an efficient reconstruction of momentum and energy of detected particles without care about their charge. Thus SIMDET assumes a LAT (lower angle tagging) detector with an acceptance between 27.5 mrad and 83.1 mrad. The minimum energy of an isolated particle is 5.0 GeV, with a resolution of 0.1%. The angular resolutions are 4.0 mrad in θ^*, and 15 mrad in ϕ^*, whereas the acceptance of the low angle calorimeter (LCAL) is between 4.6 mrad and 27.5 mrad. The polar and azimuth angle, θ^* and ϕ^*, respectively, are defined with respect to the beam pipe. We remark the algorithm used by SIMDET is restricted to detect only neutral particles. It means that the scattered electron and positron (p_1' and p_2') would be recognized as "photons" at small angles. In order to test the potential of SIMDET we have performed a simulation for identification and reconstruction of particles in the forward regions. A recent version of SIMDET includes the generator PYTHIA by default. The sipyth.F file allows to change or make extensions properly in according to the desired processes. We think that the very important switches

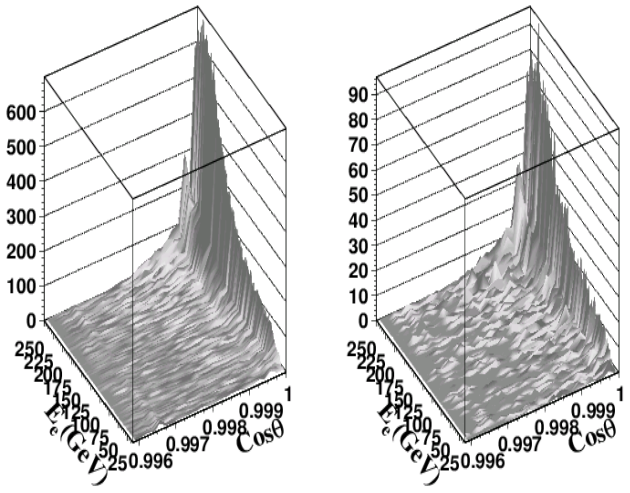

Figure 5.7: Detected particles in the instrumented mask. Left and right panels display the reconstructed e^+/e^- energy from two photons processes: $\gamma^*\gamma^* \to \mu^+\mu^-$ and $\gamma^*\gamma^* \to \tau^-\tau^+ \to \nu\bar{\nu}\mu^+\nu\bar{\nu}\mu^-$ respectively.

for a correct generation of these two-photon events should take into account the following
DO I = 1 , 173
MDME(I,1) = 0
ENDDO
MDME(171,1) = 1
CKIN(3) = 10.0.
While MDME had to be closed for values which are not of our interest, we set MDME(171,1) = 1 enabling the off-shell production of $\mu^+\mu^-$ pairs. The command CKIN(3) has the purpose in to apply a cut at P_T=10 GeV in the phase space integrations. It actually reduces the cross section to 7K fb being required for practical ends. This procedure was used for calculating the cross section shown in Table 5.1. Once the events are generated they are going to fill out the n-tuples for both $\gamma^*\gamma^* \to \mu^+\mu^-$ and $\gamma^*\gamma^* \to \tau^+\tau^-$ by separated. In Fig. 5.7 are plotted 2-dimension histograms of energy lepton energy versus cosΘ. These plots give an evidence of a higher population of events just for energies in the order of 225 GeV at small angles at cosΘ $\approx$ 0.999. For this example a $\sqrt{s}_{e^+e^-} = 0.5$ TeV is assumed. Once we have the simulated signal events in hands we turn now to make a confrontation with the off-shell two-photon processes.

Usage of SIMDET at Low Angles

The SIMDET package includes the subroutine silowt.F which is responsible to simulate the instrumented mask and forward luminosity calorimeter what are the subcomponents of ILC detector for angles down to 83.1 mrad. The forward calorimeter consists in two parts: Low Angle Tagging (LAT) and the Luminosity Calorimeter (LCAL). It is important to recall the technical limitation of LCAL which is that of detecting electrons or positrons like neutral objects.

Precisely, this limitation is taken into account in SIMDET what have treated to the particles entering to the LCAL as "photons".

It means that a useful way to recognize and reject the photon-photon processes would be that of measuring the energy of detected photons E_γ. Consequently, we have filled out histograms containing uniquely information about the energy of detected photons.

It is displayed in Fig. 5.8 in where one can see that a small fraction of signal events contain a $E_\gamma > 50$ GeV contrarily to the two-photon processes which displays an ascendent behavior for E_γ greater than 50 GeV. From Fig. 5.8 one can drawn that an acceptance of E_γ below 80 GeV rejects a sizeable fraction of the two photon processes, namely about 35%. As to the angular distributions, the rejected events had a small angles down 85 mrad, respect to the beam pipe. After of scanning others possible scenarios we have concluded that the best choice is that of applying a cut on 80 GeV. From these simulations we have concluded that the usage of this cut might enhance the signal efficient. Consequently, we have preserved this cut to be considered in the preselection [1]

5.4.2 Preselection of Events

A preselection of events is applied uniquely for rejecting evident noise. This step is performed inside sianal package already included in SIMDET. Actually, the fast simulation option has a performance even competitive to the ones of full reconstruction as to physics analysis. Diagnostics of collider capabilities provided by SIMDET have turned out to be reliable at the past and hence is used for measuring of SUSY observables for instance masses, widths and decays. Concretely, SIMDET is used to emulate the expected response of a ILC detector aimed to reconstruct the 4-momentum of stable particles based on the detector parameters cited in TESLA TDR [A$^+$01]. According to this document a high efficiency of order of 99% to identify single muons with energies above 5 GeV might be viable. On the other hand, detector

[1] H. U. Martyn have coined a name to this cut: "*v*eto *a l*o *Z*euthen".

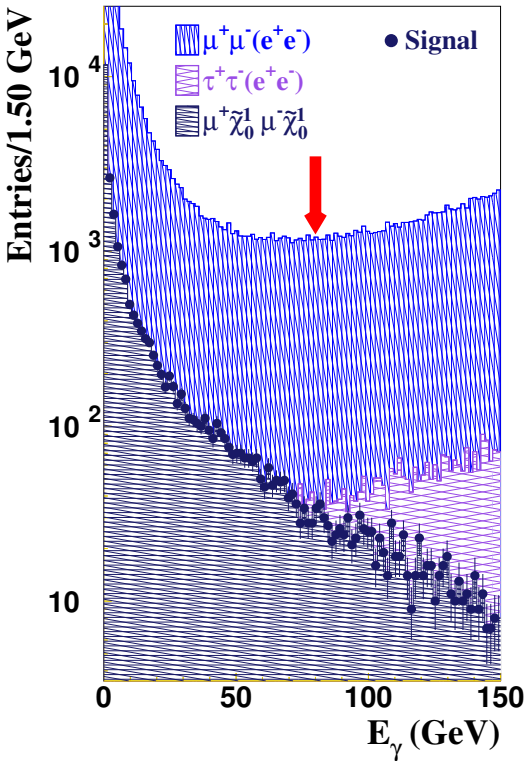

Figure 5.8: Simulated E_γ for signal and two photon processes in their ways $\gamma^*\gamma^* \to \mu^-\mu^+$ and $\gamma^*\gamma^* \to \tau^-\tau^+ \to \nu\bar{\nu}\mu^+\nu\bar{\nu}\mu^-$ with the package SIMDET.

resolution would fail in identifying such species for energies below the 5 GeV. However, the current 4th concept have introduced strategies to tag and allow momentum measurement for energies at the range of 1-5 GeV. While the dual-readout calorimeter uniquely tags muons, the magnetic field of the dual solenoid assure us a high precision in the muon momentum measurement. Hence, a complete isolation of a single muon together with its taped kinematics is feasible. For muon identification SIMDET have assumed the following: a magnetic field B = 4.0 T, a muon misidentification probability of 0.005%, an average deposited energy of muons in both ECAL and HCAL of 3.8 GeV, a minimum muon energy of 5 GeV in order to be fully isolated and a TPC acceptance greater than 12 degrees is requiered. Therefore momenta and energies of $\mu^\pm$ for both signal and its background associated are fully reconstructed. Once the 4-momentum is taped it is possible to define some cut variables to be used in this note. In Table 5.2 kinematical and angular variables are listed. Once signal and background events are generated and stores let us to describe the event analysis. The rest of steps is done inside

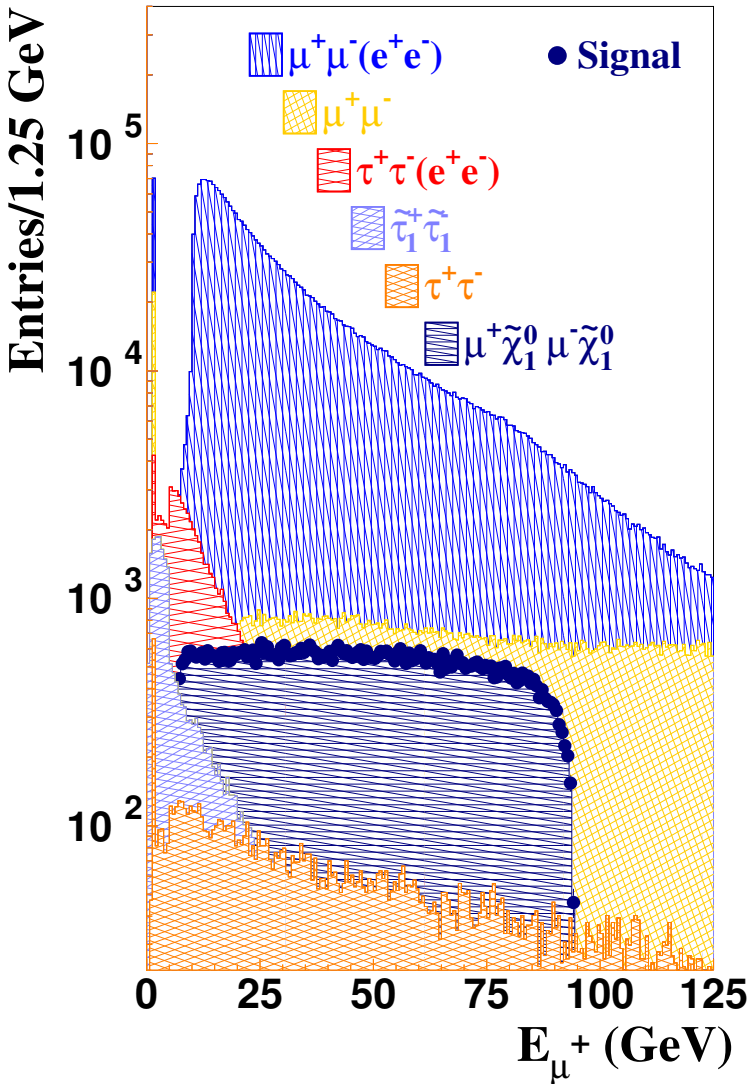

Figure 5.9: Histograms corresponding to the signal and background processes. The two photon processes dominate the SM background, whereas the stau pair production have been identified as the major supersymmetric background at low energies namely over the range 1-25 GeV. Note also the importance of the e^+e^- $\rightarrow \gamma Z^0 \rightarrow \mu^+\mu^-$ reactions throughout the allowed energy range. The pronounced peak of the two photon process histogram is a result of applying the P_T cut at the generator level. No cuts has been applied.

PAW framework.

Hence, at the detector level 74750 signal events were registered whereas 3890610 events were accounted in favour to the background. A 75% of them are derived from the two photon processes as stated early. We start the analysis with a signal purity p = $\frac{N_s}{N_s+N_b}$ = 0.0189. In Fig. 5.9 we have plotted, the muon energy of signal and its relevant background without any cut applied. Special interest is paid on the muon energy distribution because of their importance to extract kinematical information of $\tilde{\mu}_R \to \mu\tilde{\chi}_1^0$ decay. Our strategy is as follows: cuts will be applied by avoiding disturb the shape of signal energy distribution. From Fig. 5.9 one can observe that the signal is completely underneathed essentially by the two-photon processes given by $e^+e^- \to e^+e^-\mu^+\mu^-$ reactions. We can also to note that the $e^+e^- \to \gamma/Z^0 \to \mu^+\mu^-$ processes contribute to the background overall the signal distribution, between 5 and 100 GeV. There are also contamination that seriously affects the low energy part of the signal ($E_\mu < 20$ GeV) and those are the $e^+e^- \to e^+e^-\tau^+\tau^-$, $e^+e^- \to \gamma/Z^0 \to \tau^+\tau^-$ and $e^+e^- \to \gamma/Z^0 \to \tilde{\tau}_1^+\tilde{\tau}_1^-$ processes. In general, final state radiation increase the number of energy flow objects, by increasing the number of photons in the final state only if it is kinematically allowed. In this way, we had to preselect events with a number of energy flow objects between 2 and 4. Indeed, based on the plot 5.7 and 5.8 we have preselected events with $E_\gamma < 80$ GeV. The effect of the preselection is reflect in the gained statistics: 2809260 background events remain, whereas the signal was reduce to 64330 events.

5.4.3 Final Selection

A fully rejection of background needs a strategy that in principle would have to be the most economical way to save signal events as well as improve their purity. Then, we have defined an useful set of cut variables based on the knowledge of the momentum and energy of detected muons. In Table 5.2 are explicitly described the variables to be used in addition to the muon energy distribution. Besides ϕ denotes the opening angle of two particles projected onto a perpendicular plane respect to the beam pipe, cosθ describes the opening angle between two particles in the three dimensional space. Furthermore, P_T denotes the transversal momentum of a muon pair and it becomes the most important variable whereas P_{miss} the missing momentum at the laboratory frame. M_{μ^+,μ^-} and M_{miss} defines the invariant mass and missing mass of a system of two muons, respectively. The next step consists in reconstructing the kinematical variables described in Table 5.2, therefore the histograms are

Variable	Definition
ϕ	$\cos^{-1}(\Sigma_k P_{1,k} P_{2,k} / \sqrt{\Sigma_l P_{1,l}^2 \Sigma_k P_{2,k}^2})$ $l,k = 1,2 \;\; (\mathrm{p}lane \;\; x-y)$
$\cos\,\theta$	$\Sigma_m P_{1,m} P_{2,m} / \sqrt{\Sigma_n P_{1,n}^2 \Sigma_m P_{2,m}^2}$ $m,n = 1,3 \;\; (space \;\; x-y-z)$
P_T	$\sqrt{\Sigma_j (\Sigma_i P_{i,j})^2} \;\; i = \mu^+, \mu^-, \; j = 1,2 \;\; (\mathrm{p}lane \;\; x-y)$
$P_{\mathrm{m}iss}$	$\sqrt{\Sigma_j (\Sigma_i P_{i,j})^2} \;\; i = \mu^+, \mu^-, \; j = 1,3 \;\; (space \;\; x-y-z)$
M_{μ^+,μ^-}	$\sqrt{(\Sigma_i E_i)^2 - \Sigma_j (\Sigma_i P_{i,j})^2} \;\; i = \mu^+, \mu^-, \; j = 1,3 \;\; (space \;\; x-y-z)$
$M_{\mathrm{m}iss}$	$\sqrt{(\sqrt{s} - \Sigma_i E_i)^2 - \Sigma_j (\Sigma_i P_{i,j})^2} \;\; \sqrt{s} = 0.5$ TeV $i = \mu^+, \mu^-, \; j = 1,3 \;\; (space \;\; x-y-z)$

Table 5.2: Definition of kinematical variables used throughout this work.

normalized to the signal luminosity. We define the relative statistical error,

$$\frac{\Delta N_s}{N_s} = \frac{1}{\sqrt{N_s \cdot \epsilon \cdot \mathrm{p}}}. \tag{5.4}$$

where N_s is the number of events before cuts. The numbers ϵ and p are recognized as the efficiency and purity respectively. In top panel of Fig. 5.10 the histograms corresponding to the P_T variable are plotted. Interestingly, SM distributions are featured by a descendent behavior in contrast to the SUSY signal whose P_T distribution is curved. In response to the plots displayed in Fig. 5.10 one should keep the region that in certain extent would have to be inconsistent with the expected or known behaviors. Statistically, we search for those cuts which minimizes $\Delta N/N$ or in other words that maximizes the product e×p.

Respect to the plots of Fig. 5.10 the signal distribution appears to have a distinctive behavior against to the SM ones. So that we have accepted events inside the region of this "anomalous" behavior, between 15 GeV and 90 GeV. In order to be more realistic, on bottom panel of Fig. 5.10 is shown the P_T distribution when histograms of signal and all backgrounds have been added. It is the one which might be observed in the real data. In this histogram a predominant curve between 20 GeV and 90 GeV is observed. This rare

behavior should have to be associated to the presence of new physics. In the following, given a distribution we shall keep events inside the region that is not adjustable to standard physics, or in other words, what is rare respect to the expected ones from SM processes. Herein we means by "real" histogram, the one constituted by the sum of all histograms (signal and backgrounds).

The P_T also serves to reject a huge amount of two photon processes events. Concerning these processes a peak around 10 GeV is viewed. It has its origin at the command CKIN(3)=10 (GeV) which enable us to redefine $1/P_T \rightarrow 1/P_T + 1/(P_T - P_{cut})$ originating a peak at $P_{cut} = 10$ GeV. Thus, we reach a signal purity and efficient of 57.90% and 70.80%, respectively.

We have also used the invariant mass variable M_{μ^+,μ^-} for the next cut to be applied. It is because exist there a notable distinction between signal in virtue of left panel of Fig. 5.11. Hence we have carried out the reconstruction of M_{μ^+,μ^-} for all processes involved. The figure also shows the presence of a peak which is in reality the Z^0 boson mass. It happens because the presence of the $e^+e^- \rightarrow \gamma, Z^0 \rightarrow \mu^+\mu^-$ reactions. The histogram corresponding to these processes contains a minor peak just around 60 GeV as result of P_T cut. In the top right panel one can observe a curve and it demand us to select events inside the curve. Thus we have kept the region between 5 GeV and 190 GeV. The benefits of this cut is reflected in the signal statistics that yields a purity of 70.48%.

Indeed, we have used the missing mass variable for plotting the histograms of remaining processes. The bottom left panel of Fig. 5.11 suggests to evaluate the possibility in to keep the region around the peak closely to 400 GeV. A mostly stringent histogram as depicted in the bottom right panel of Fig. 5.11 indicate us to apply a cut just on 320 GeV which would correspond in to filter those events containing a substantial missing mass due to the existence of heavy invisible particles. Note also the cut is applied just on the region where occurs a jump close to 320 GeV, and it can interpretated as the transition of SM to a "new physics". Statistically speaking, a signal efficiency of 70.35% have been achieved whereas the purity have been augmented to 75.55%.

In parallel we have had to monitor the impact of the applied cuts on the shape of muon energy distribution, the most important observable at this analysis.

Thus, top left panel of Fig. 5.12 displays the muon energy E_{μ^+}. The applied cuts so far have had positive consequences. The signal distribution appears to be defined in comparison with the poor statistics of backgrounds. The top right panel shows the spectrum consisting in a trapezoid-like shape and a long tail. Thus we have had to restringe the region of interest between 3 GeV and 110 GeV in both distributions E_{μ^+} and E_{μ^-}. Instead of accepting

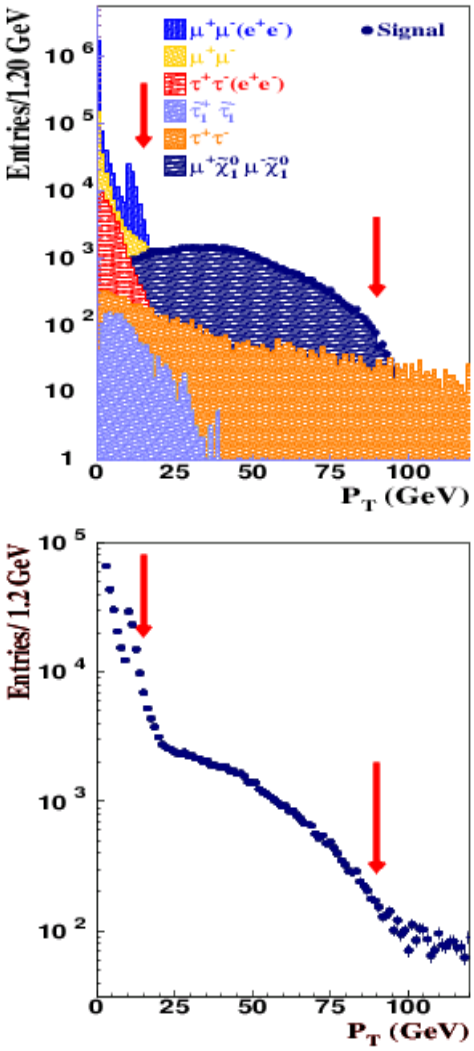

Figure 5.10: Top panel: P_T distribution of signal (with error bars) and background. Bottom panel: A mostly realistic plot for all P_T distributions have considered the sum of both signal and backgrounds histograms. In both cases the arrows indicate the position of the applied cuts.

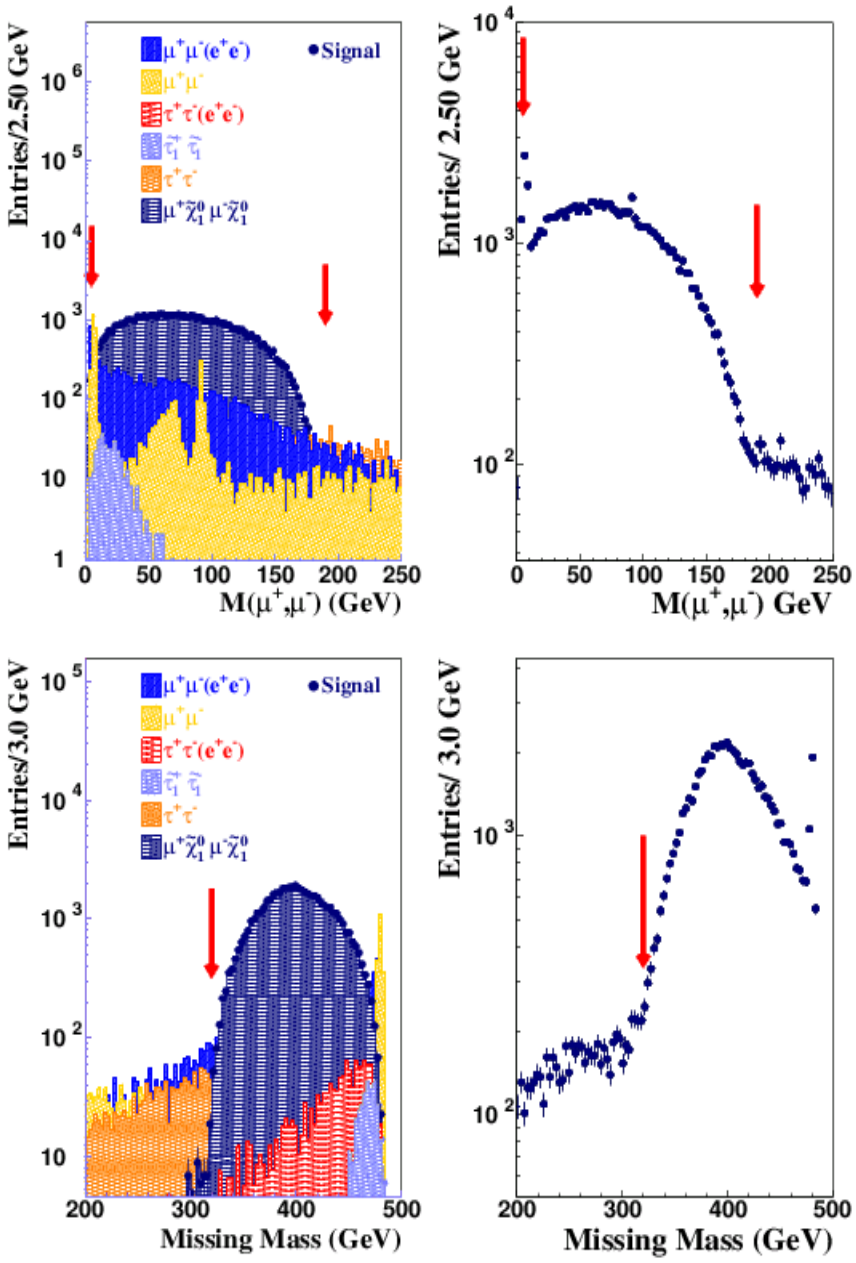

Figure 5.11: On the Top left and right panel panel are plotted the invariant mass distribution of signal and noise. The peaks appears as consequence of the previous cuts. On the bottom left and right panels are plotted the missing mass.

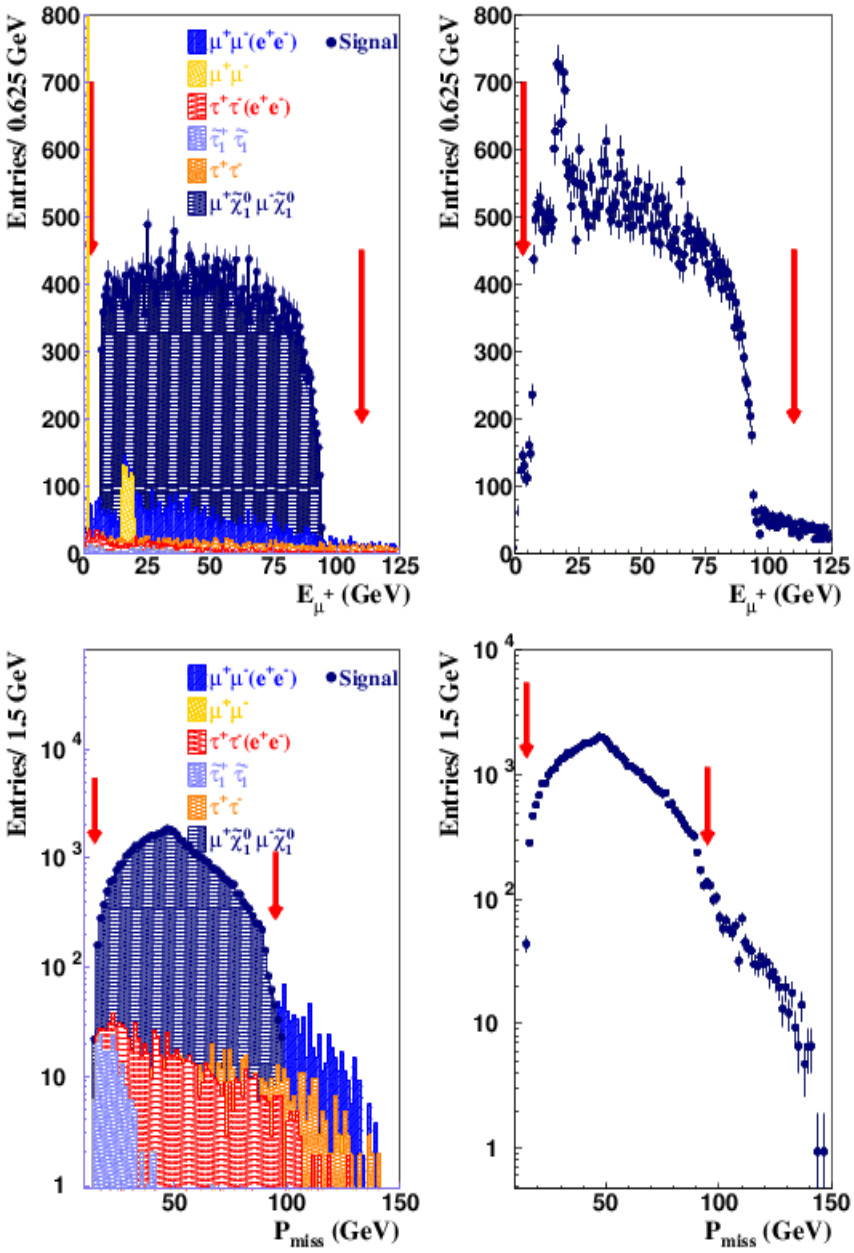

Figure 5.12: Top left and right panel: The E_μ distribution where signal can be distinguishable from noise. Note that the peak on 18 GeV is a consequence of the applied cuts. Bottom left and right panel: The missing momentum and the respective cuts.

signal events just on 97 GeV, which is apparently the endpoint of the right edge of signal spectrum in according to the plot, we have also considered a portion of the tail by which it would help us to measure the endpoint within a reasonable precision as we shall see later. On the other hand, the neccesity in to cut on 3 GeV is in accordance to the unclear left endpoint where a strong contamination of low energy muons occurs.

In other words, the application of cuts on the energy distribution is valid only if the cuts does not affect the tails in both sides of spectrum.

Therefore we have reached a purity of 81.93%. On the other hand, the signal statistics looks stable as seen in $\Delta N_s/N_s = 0.48\%$. However, around 21 GeV is seen a rare peak whose origin is linked to the effect of cuts. It forces us to find more variables what would have to drastically reduce the remaining background events, specially at the low energy region. Based on the fact, we have also decided to accept events with $\cos\theta < 0.975$, having raised the purity to 84.08%. On the bottom left panel of Fig. 5.12, the missing momentum of remaining events have been plotted being the region limited by 15 GeV and 95 GeV is the most favorable, even though the realistic case (bottom right panel) indicates there not any preferred place to apply the cuts. Actually, we have decided to keep signal candidates inside the curve which is actually peaked. Furthermore, for P_{miss} beyond 95 GeV the data can be interpretated as pure SM events in the sense that it cannot coexist with "new physics" events.

Systematically, we have evaluated the impact of the the application of cuts between 15 GeV and 95 GeV and it does not change substantially $\Delta N_s/N_s$. Our strategy for noise rejection thus appears to be efficient as reflected at the statistics, arriving to a signal purity of 85.8%.

Finally, the $(E_{\mu^-} + E_{\mu^+})/E_{vis}$ variable was used to reject events whose total energy is smaller than their visible energy. A clear case are the two

Cut	Efficiency(%)	Purity(%)	$\Delta N_s/N_s$(%)
15 GeV$< P_T <$90 GeV	70.80	57.90	0.57
5 GeV $< M_{\mu^+,\mu^-} <$ 190 GeV	70.45	70.49	0.52
$M_{miss} >$ 320. GeV	70.35	75.55	0.51
3 GeV $< E_{\mu^+,\mu^-} <$ 110 GeV	70.21	81.93	0.48
$cos\theta < 0.975$	69.03	84.08	0.48
$P_{miss} >$ 80. GeV	68.91	85.80	0.48
$(E_{\mu^-} + E_{\mu^+})/E_{vis} > 0.80$	**65.44**	**93.27**	**0.47**

Table 5.3: Final statistics extracted from signal and background events.

photon processes where their visible energy is much bigger than the energy

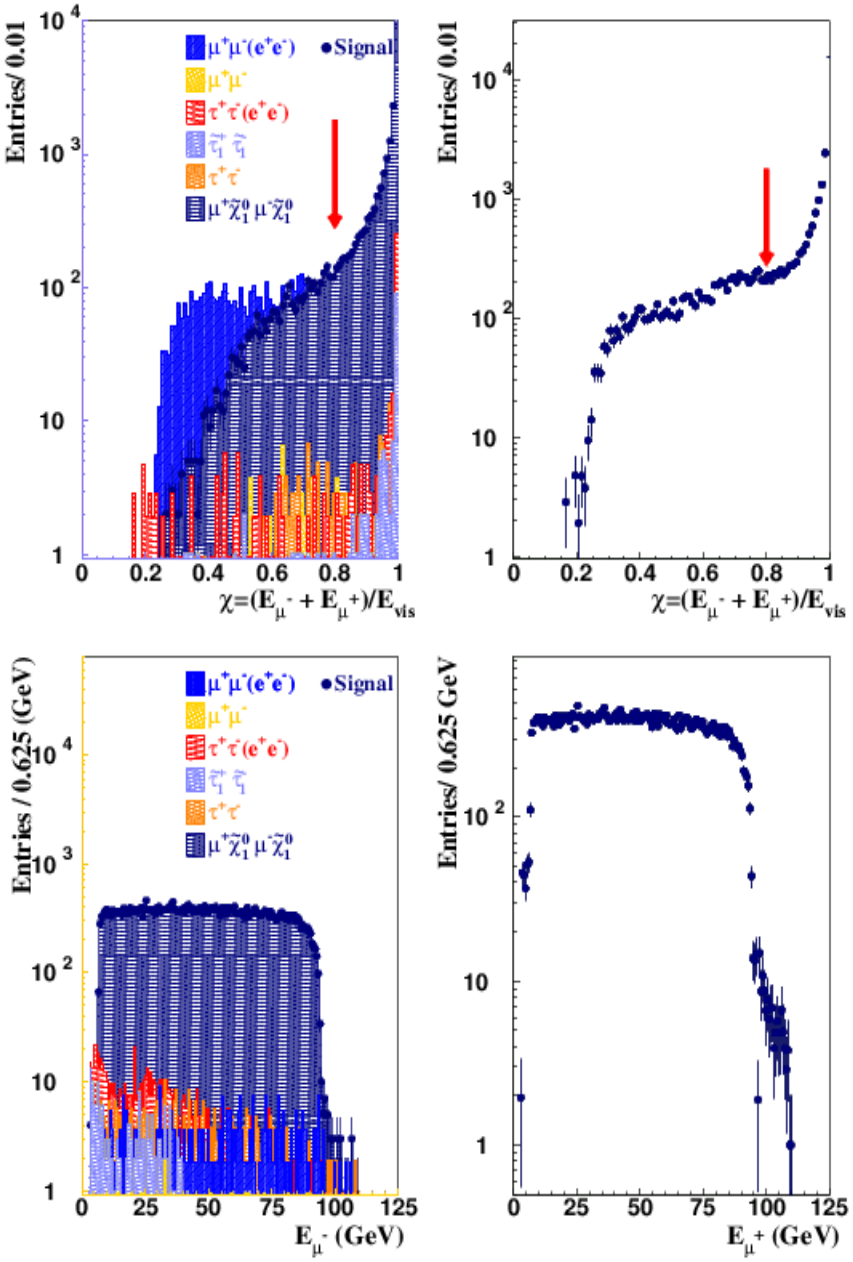

Figure 5.13: Top left and right panel: $(E_{\mu^-} + E_{\mu^+})/E_{vis}$ distribution. To note the absence of a privileged region in comparison with previous cuts. Bottom left and right panel: The E_{μ^+} distribution after selection cuts.

carried by the muons. Concerning the photons accounted in the signal events, they are predominantly low energy and thus $(E_{\mu^-} + E_{\mu^+})/E_{vis} \approx 1$. In this way, a cut close to this value is needed. Before to decide a value on which a cut should be applied, we have confronted the correlation between this cut and the resulting muon energy distribution which is plotted in the bottom left and right panel of Fig. 5.13. In other words, the signal spectrum "geometry" of the signal distribution have been examined for $(E_{\mu^-} + E_{\mu^+})/E_{vis} = 0.5$, 0.6, 0.7 and 0.8 as well.

We have found that the acceptance of events with $(E_{\mu^-} + E_{\mu^+})/E_{vis} > 0.8$ does not substantially change $\Delta N_s/N_s$, neither the shape of the signal muon energy distribution. Finally, the energy distribution has a trapezoid-like shape well defined. The bottom right panel of Fig. 5.13 shows the possible real distribution that could be seen at the e^+e^- collider. The tail on the right edge was kept due to the following reason already stated: It enters to the endpoint analysis and it should be taken into account along the fitting region of the endpoint.

Our mission now is that of using the endpoint method to extract kinematical information from the $\tilde{\mu}_R \to \mu\tilde{\chi}_1^0$ decay. The acquired information is just used for the error calculation in the measurement of $\tilde{\mu}_R$ and $\tilde{\chi}_1^0$ masses. Table 5.3 summarizes the statistics achieved.

5.5 Fitting the Endpoints

From the previous analysis the isolation of the signal have been possible and thus a strategy for extracting information is needed. It is easy to note the simplicity of the $\tilde{\mu}_R \to \mu\tilde{\chi}_1^0$ decays that provides an advantage in these studies. Even though the involved kinematics of this two-body decay led to deduce the masses of the sparticle based on the information of the endpoints located in both sides of the muon energy spectrum. It is called the endpoint method and allows us to know the smuon and neutralino masses only if $E_{\mu,max}$ and $E_{\mu,min}$ are rigorously measured. While a carefully application of cuts have not degraded the "geometry" of energy spectrum, those background events what survived the selection might give raise to ambiguities. This situation makes the usage of the endpoint technique questionable. In order to be consistent, we can assign a systematical error associated to the presence of irreductible background.

On the other hand, the knowledge of the "experimental" endpoints and the center-of-mass energy serve as inputs for the following relations,

$$m_{\tilde{\mu}} = E_{cm}\frac{\sqrt{E_{\mu,max}E_{\mu,min}}}{(E_{\mu,max} + E_{\mu,min})} \tag{5.5}$$

$$m_{\tilde{\chi}_1^0} = m_{\tilde{\mu}} \sqrt{1 - \frac{2(E_{\mu,max} + E_{\mu,min})}{E_{cm}}}, \tag{5.6}$$

which can be obtained after a little algebra. Indeed these equations require a precise knowledge of center of mass energy which it is assumed to be constant. In previous sections, it have been discussed a realistic scenario what contemplates a possible distortion of the energy beam by effects of radiation resulting in systematics. However, the impact of this uncertainty on the results is negligible.

The next step consists in to develop a strategy to measure $E_{\mu,max}$ and $E_{\mu,min}$ from the muon energy distribution. Some strategies were developed in the past by applying a fit along the trapezoid-like energy distribution [T$^+$95]. Instead of searching for a fit function that is adjustable to the background separately, our proposal consist in to perform the fitting procedure once the remaining background histograms have been added to the signal one.

The starting point is the definition of the fit functions or often called "step" functions used in the past to reconstruct some properties of tau lepton in OPAL [Sta02]

$$f_1(E) = (\frac{p_1}{2})(1 - \frac{p_4 \cdot x_0}{\sqrt{1 + x_0^2}}), \qquad \text{(left edge)} \tag{5.7}$$

$$f_2(E) = \frac{p_1}{\pi}(1 - p_4 x_0)(\frac{\pi}{2} - tan^{-1} x_0), \qquad \text{(right edge)} \tag{5.8}$$

where $x_0 = p_2(E - p_3)$, and p_1, p_2, p_3, p_4 are the parameters of the fit, p_1 describe the high, p_2 the width, p_4 the "slope of Plateu", and p_3 is the endpoint. These functions are adjustable to the lateral sides of the energy distribution shown in bottom right panel of Fig. 5.13. At first instance we have performed the fitting by using only functions (5.7) and (5.8). However we have noted that χ^2 per degrees of freedom, have turned to be almost 2 for both sides (left and right) by suggesting that the step-functions does not adjust fully to the data and additional functions are required. It occurs because the background changes the intrinsic nature of the muon energy distribution. A possible solution to this obstacle is the inclusion of a polynomial function which is added to the fit function. This step can guarantee a substantial improvement of χ^2. These statistical analysis have used MINOS and MINUIT [JR75] [Bec03]. In this manner, we had have reformulated the fit functions being now expressed as $f_1(E) + g(E)$ and $f_2(E) + h(E)$ where $g(E)$ and $h(E)$ are polynomial functions. We have performed succesives fits by varying all parameters until a reasonable χ^2 is reached. Then we have fixed the parameters corresponding to the functions $g(E)$ and $h(E)$. We have used fifth

order polynomial functions for modeling the background being featured by a smooth curve.

Once polynomial function parameters are fixed, we have perform a fit by having uniquely the parameters p_1, p_2, p_3 and p_4. We noted that the χ^2 appears to be smaller compared to the case when polynomial functions are not used. In this stage of analysis it is noteworthy the stability of the "step" functions parameters.

In order to optimize χ^2 and extract the endpoints, a last step is performed. After of finding a stable value for χ^2, we have optimized our procedure having fixed p_1, p_2 and p_4 parameters, whereas a one-parameter p_3 fit was finally applied. Actually last step is in accordance with it what can happens in future experiments. We expect when the ILC experiment is running a multi-parameter fit to the full spectrum will be done on Monte Carlo samples while the one-parameter fit will be applied to the data. The fitting have yielded a stable value for p_3 even for different values of bins. Top panel of Fig. 5.14 shows the curve that adjusts to the "data", resulting in p_3= 6.665 $\pm$ 0.0167 for the left side being mostly contamined by event coming from low energy species of stau decay. Some of them are distorting the tail of signal spectrum by producing systematics. For the right side, a p_3= 93.52 $\pm$ 0.0412 have been reached. For this case the curve just matches the error bars of "data" exceptionally over the long tail what is extended up to 105 GeV. For both sides, a small variation of bins had to be taken into account in oder to demonstrate a fully independence on the binning. In addition, χ^2/ndf = 1.07 (left edge) and 1.18 (right edge) have been obtained.

5.5.1 Mass "Measurement"

We are in the position to evaluate the sparticle masses as well as their respectives uncertainties. Inserting the fitted values in (5.5) and (5.6) we get $m_{\tilde{\mu}_R} = 124.6$ and $m_{\tilde{\chi}_2^0} = 96.45$ being these values quite close to the nominal ones given by 124.25 GeV and 96.04 GeV.

However, the most important fact is to know the precision of these "measurements". For the evaluation of uncertainties we assume quadratic errors, and in this way the following expressions will be considered,

$$\delta m_{\tilde{\mu}} = \sqrt{(\frac{\partial m_{\tilde{\mu}}}{\partial E_{max}})^2(\delta E_{\text{max}})^2 + (\frac{\partial m_{\tilde{\mu}}}{\partial E_{min}})^2(\delta E_{\text{min}})^2}, \tag{5.9}$$

$$\delta m_{\tilde{\chi}} = \sqrt{(\frac{\partial m_{\tilde{\chi}}}{\partial E_{max}})^2(\delta E_{\text{max}})^2 + (\frac{\partial m_{\tilde{\chi}}}{\partial E_{min}})^2(\delta E_{\text{min}})^2 + (\frac{\partial m_{\tilde{\chi}}}{\partial m_{\tilde{\mu}}})^2(\delta m_{\tilde{\mu}})^2} \tag{5.10}$$

where center of mass energy fluctuations was neglected. Again, it is assumed that the system energy can be extraordinary measured by implying the absent of terms proportional to $\delta\sqrt{s}$ in (5.9) and (5.10). Concerning (5.9) we have obtained $\delta m_{\tilde{\mu}} = 0.137$ GeV which is roughly a 20% bigger than the one obtained at the past [NC03] where the SPS1a model was used. This discrepancy addresses the issue of testable mSUGRA models in colliders in which might exist the possibility of having a muon spectrum whose left side is close to 0. For (5.10) we have included the smuon uncertainty in agreement to (5.6). The evaluation for the neutralino mass error yields $\delta m_{\chi} = 0.099$ GeV what exceeds in a 25% with respect to the one computed in [NC03].

The reason of why these uncertainties differ at the level of 25% with respect to the ones obtained under the assumption of SPS1a model is related to the left endpoint of spectrum whose value is unclear at very low energies. In fact, when the left side of spectrum just appears to be over the low energy range, 1 GeV - 5 GeV, inherent errors due to stau background and muon detector resolution may have a dramatic impact on the mass "measurement". Mainly, is here where the remaining background events affect the morphology of the left-side endpoint and become a non negligible source of systematic error. Therefore the application of the endpoint technique is not longer valid when the left side of spectrum has energies down to 5 GeV. Contrarily, a successfully use of this technique for energies far from 5 Gev is actually expected.

5.6 Systematics Uncertainties

Basically, the "measurements" are affected by the beam energy, polarization, and cuts.

- Beam energy: We have computed a small influence of the beam energy resolution on the mass measurement. This error enters linearly in the smuon mass measurement yielding a systematics of 0.01%.

- Polarization: An uncertainty of the beam polarization in the level of 0.25% (e^+ and e^- beams) produces a variation of 0.16% on the cross section. Thus it has a negligible influence on the mass measurement.

- Cut procedure: The most important cuts through the analysis have been the P_T cut. We have redo the analysis when the P_T cut varies for values of 15-100 GeV, 10-90 GeV and 5-120 GeV. It yields a small change on the mass measurement of order of 0.1%.

These errors, added in quadrature resulted in a 0.1% systematics error. This uncertainty has to assigned to both smuon and neutralino.

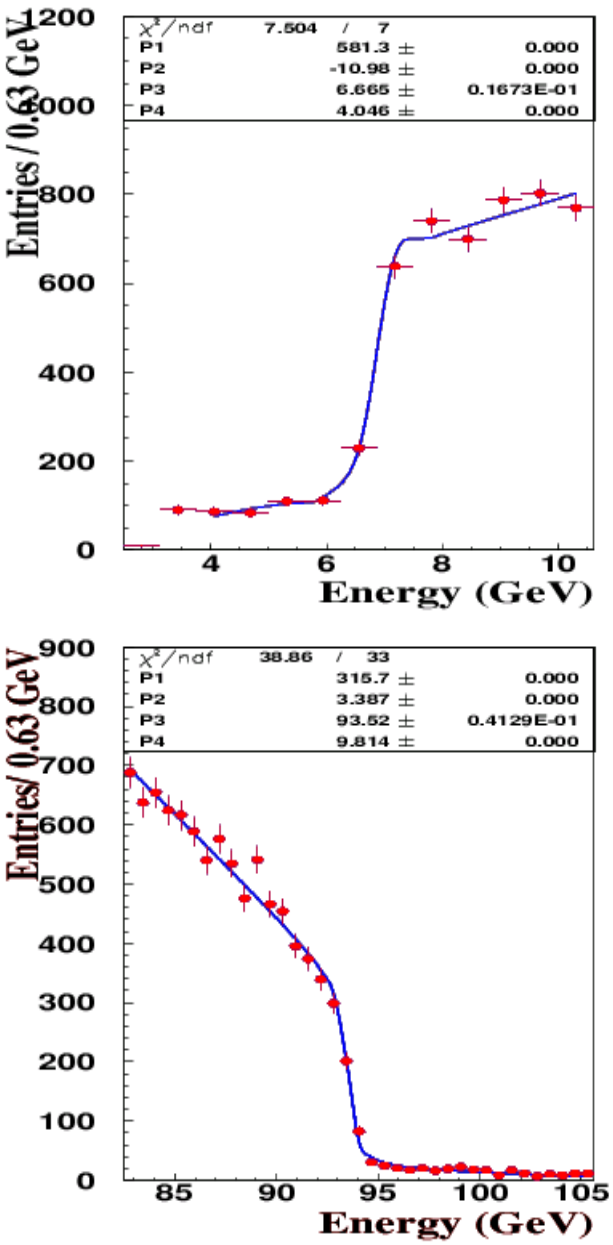

Figure 5.14: Top panel: The fit of the left edge along a short region of the E_μ distribution. Bottom panel: The fit of the right edge which include a portion of the tail, it is up to 105 GeV.

Chapter 6

The ILC Photon Collider

6.1 Functionality of a Photon Collider

A representation of a possible layout of a photon collider is shown in Fig. 6.1(a) where a side is shown. Because the linear collider are single-pass accelerators, the electron beams are used. According to the figure, a single electron collides with a laser photon in the Conversion Point (CP) to a distance "b" from the Interaction Point (IP) by obeying the physics of Compton scattering. In praxis, "b" is of order of a few millimeters whereas $\alpha \approx 30$ mrad. In the CP is created a photon whose energy can reach up to a 85% of incoming electron. Therefore, the created photon travels a distance "b" and collides with the one just created in the opposite side. It constitutes a photon-photon collider but in contrast to the e^+e^- collider, the center-of-mass energy for this system is not constant anymore. Further collisions are also expected: e^-e^- and γe^-. Experimentally, a laser flash energy of several Joules is crucial to convert almost all electrons to high energy photons. It means that a conversion coefficient $\frac{N_\gamma}{N_{e^-}} \approx 1$ is technically feasible. It implies that the number of high-energy photons $N_\gamma \approx N_{e^-} \approx 10^{10}$. Thus, a luminosity comparable to that of the e^+e^- collisions can be achievable. In fact, since the photon spot size at the IP will be almost equal to that of the electrons at the IP, the luminosity of $\gamma\gamma$, $e^-\gamma$ collisions will be similar to the geometric luminosity of the basic e^+e^- beams. To avoid background from the disrupted beams, a crab crossing angle as sketched in Fig. 6.1(b) of about 25 mrad is needed, in order that the final particles do not hit focusing quadruples. In table 6.1 is listed the called "conservative" ($\gamma\gamma^2$) and "optimistic" ($\gamma\gamma^1$) parameters [M$^+$06].

Beam Param.	e^+e^-	$\gamma\gamma^1$	$\gamma\gamma^2$
$\sigma_z[\mathrm{m}m]$	0.3	0.3	0.3
pulser/train	2820	2820	2820
Repetition rate [Hz]	5	5	5
$\gamma\epsilon_{x/y}/10^{-6}$[m.rad]	10/0.03	2.5/0.03	3.0/0.03
$\beta_{x/y}[\mathrm{m}m]$ at IP.	15/0.4	1.5/0.3	4/0.4
$\sigma_{x/y}[\mathrm{n}m]$	553/5	88/4.3	157/5
$\mathcal{L}[10^{34}\mathrm{c}m^{-2}\mathrm{s}^{-1}]$	3.4	1.1	0.6

Table 6.1: Parameters of the e^+e^- collider and the photon collider. Note that the luminostity is given for $z > 0.8z_m$.

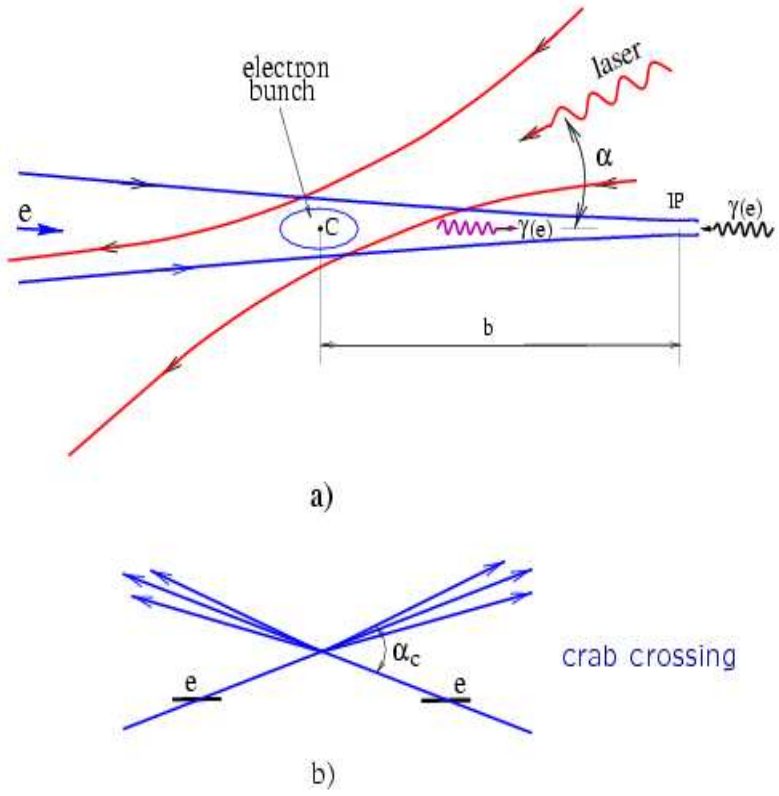

Figure 6.1: A sketch of a possible layout of a photon collider. The parameters b and α denote the distance between the conversion and interaction points and the crossing angle between the laser and the electron beam, respectively.

6.1.1 Requirements for the ILC Design

The building of a photon collider imposes some requirements:

- To remove the disrupted beams a crab-crossing angle of about 25 mrad is needed.
- The $\gamma\gamma$ luminosity is closely proportional to the geometric e^-e^- luminosity, thus the product of the horizontal and vertical emittance should be as small as possible.
- The final-focus system should provide a beam-spot size at the interaction point that is as small as possible.
- The very wide disrupted beams should be transported to the beam dumps with acceptable losses.
- The detector design should allow easy replacement of elements in the forward region (< 100 mrad).
- Space for the optical arrangement has to be reserved.

6.2 Principles of a Photon Collider

The idea of producing single high energy photons at the range of the TeV scale is not new. Historically it was formulated during the 60s [Aru63] inside the theory of Compton scattering. Although the physics behind the formulation of Compton scattering is well-known and totally understood, the experimental requirements for the realization of a photon collider seems to be not simple. Several aspects concerning the construction and functionality as well as the physics processes of central importance are specified in Ref. [KT02].

The starting point for an adequate introduction of the principles of the photon collider is the description of the dynamics which occurs in the Compton scattering. Thus one considers a single laser photon with an energy ω_0 what is scattered by an electron with energy E_0 at a small collision angle α in the conversion region. The energy of the scattered photon (or "converted" electron) ω depends on its angle θ relative to the motion of the incident electron as follows:

$$\omega = \frac{\omega_m}{1 + \left(\frac{\theta}{\theta_0}\right)^2}, \theta_0 = \frac{m}{E_0}\sqrt{x+1}, \omega_m = \frac{x}{x+1}E_0, x = \frac{4E_0\omega_0}{m^2}cos^2\frac{\alpha}{2}, \quad (6.1)$$

where x is a dimensionless parameter and ω_m denotes the maximum photon energy. When the scattered photon goes through the direction of electron, the whole phenomenon is called Compton "backscattering".

The energy spectrum of the scattered photons is defined by the Compton cross section (without non-linear corrections)

$$\frac{1}{\sigma_c}\frac{d\sigma_c}{dy} = \frac{2\sigma_0}{x\sigma_c}\left[\frac{1}{1-y} + 1 - y - 4r(1-r) + 2\lambda P_c r x(1-2r)(2-y)\right], \quad (6.2)$$

where

$$y = \frac{\omega}{E_0}, r = \frac{y}{x(1-y)}, \sigma_0 = 2.5 \times 10^{-25}\mathrm{c}m^2, \quad (6.3)$$

the quantities P_c and λ denote the helicity of laser and electron, respectively. The total Compton cross section reads

$$\sigma_c = \sigma_c^{np} + 2\lambda P_c \sigma_1, \quad (6.4)$$

with

$$\sigma_1 = \frac{2\sigma_0}{x}\left[\left(1 - \frac{2}{x}\right)ln(x+1) - \frac{5}{2} + \frac{1}{x+1} - \frac{1}{2(x+1)^2}\right] and \quad (6.5)$$

$$\sigma_c^{np} = \frac{2\sigma_0}{x}\left[\left(1 - \frac{4}{x} - \frac{8}{x^2}\right)ln(x+1) + \frac{1}{2} + \frac{8}{x} - \frac{1}{2(x+1)^2}\right] \quad (6.6)$$

denoting the cross section with and without polarized electrons, respectively. These expressions does not have a strong influence on the initial polarisation configuration in contrast to the energy spectrum (6.2). It should be noted that the curve is significantly improved when the product of helicities is negative, what actually doubles the number of hard photons.

In order to see the advantage in having polarized beams, in Fig. 6.2 (left-panel) the monochromatic character of spectrum for $\omega/E_0 \approx 0.8$ when $2\lambda P_c$ = -1, is displayed. Naively one can imagine that this monochromaticity grows simultaneously with the laser energy, but unfortunately the parameter x is limited to be roughly 4.8. For values x >4.8 the production of e^+e^- pairs takes place by producing undesired $e^{\pm}\gamma$ collisions. On the other hand, the resulting polarisation is expressed as follows

$$< \lambda_\gamma >= \frac{-P_c(2r-1)[(1-y)^{-1} + (1-y)] + 2\lambda_e x r[1 + (1-y)(2r-1)^2]}{(1-y)^{-1} + 1 - y - 4r(1-r) - 2\lambda_e P_c x r(2-y)(2r-1)}, \quad (6.7)$$

where a circularly polarized laser is assumed. The right panel shows the subsequent polarisation of the scattered photons for various scenarios of helicity configuration. The most favorable configuration is that of $2\lambda P_c$ = -1

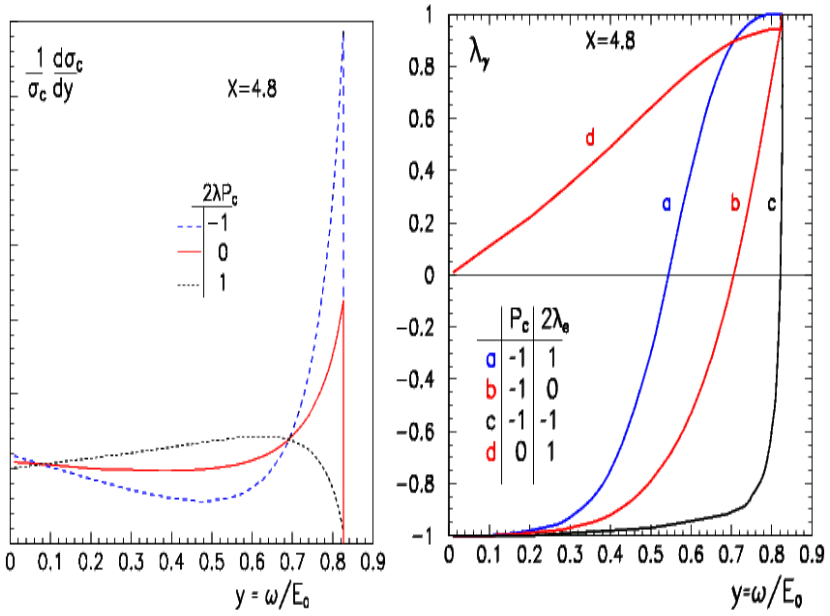

Figure 6.2: (left) Photon spectrum for different values of product $2\lambda_e P_c = -1$, and (b) the polarization as function of ratio ω/E_0

as shown that the photons would conserve their initial polarisation. This very interesting phenomenon is of enormous interest in current experiments [Beh02] in which a lowest degree of polarisation degradation is needed.

Effects by High Order Corrections

The Compton scattering in first order is not enough for a correct understanding of the physics during the conversion. Due to the presence of a high density of photons, the electron has a non-negligible probability in absorbing several photons before the final state. Expressed in the Feynman graphs language, the electron propagator receives an infinite contribution of legs by modifying substantially the total amplitude [B+71]. Undoubtedly, there exists a transition of linear to non-linear regime in the sense that the electron does not suffer of pure Compton scattering but also is sensitive to a more complex situation. This leads to define the intensity parameter

$$\eta^2 = \frac{2n_\gamma r_e^2 \lambda}{\alpha} \tag{6.8}$$

which tell us about the influence of non-linear effects over the observables. Here n_γ denotes the number of absorbed photons, λ the laser wavelength and

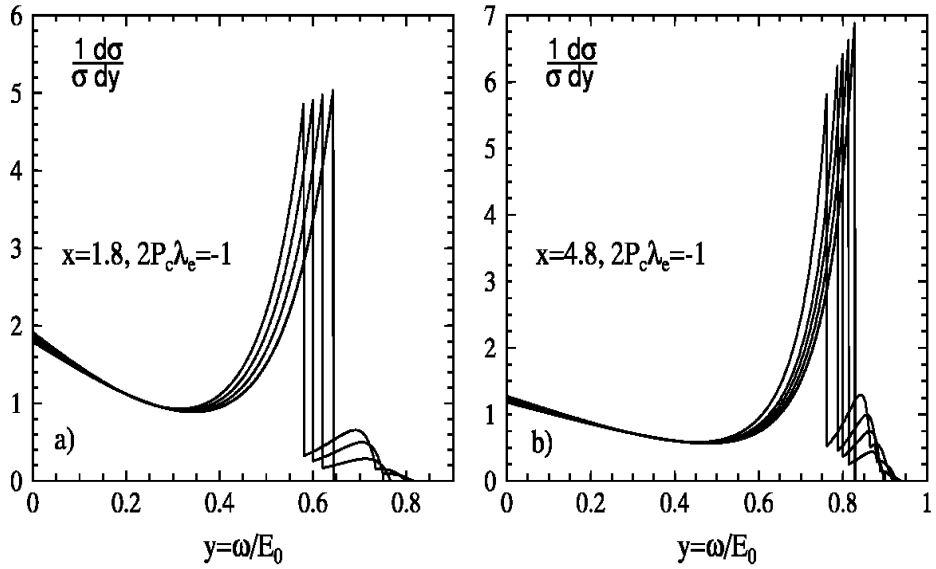

Figure 6.3: Influence on the Compton spectrum by non-linear corrections. From right to left, η^2 = 0,0.1,0.2,0.3,0.5 according to [KT02].

r_e the electron radius. Therefore the existence of non-linear effects has the following consequences

$$m^2 \to m^2(1+\eta^2) \quad and \quad \frac{\omega_m}{E_0} = \frac{x}{1+x+\eta^2}, \tag{6.9}$$

what is reflected in the photon spectrum essentially. These relations can also be interpretated as the necessity in including secondary quantum effects because the presence of a strong electromagnetic field. Fig. 6.3 shows in an instructive way the influence of these non-linear effects on the photon spectrum. For $x = 4.8$ and $2\lambda P_c$ = -1 the left panel displays the degradation of peak of the curve for various values of η^2. Indeed, the figure indicate us that the high energy region of spectrum suffers a displacement to the left side in agreement to (6.9). Interestingly is noted the presence of high harmonics at the high energy region is response to the absorption phenomenon. Actually these secondary effects is clearly against our goals and thus the knowledge of an optimum value for η^2 is crucial for a respectable performance of a photon collider. Previous works have established that $\eta^2 = 0.3$ might be the best upper limit. For example, the relative shift $\Delta\omega_m/\omega_m$ is of order of 5% which is still acceptable for physics studies.

Pair Creation and Other Processes

For values of x greater than 4, the possibility in getting e^+e^- pairs is not null anymore. In effect, the collisions between backscattered photons and laser photons happens and it is realizable above threshold $\omega_m\omega_0 = m^2$ resulting in a $x \approx 4.83$. The Dirac [1] cross section for e^-e^+ creation is given by

$$\sigma_{\gamma\gamma\to e^+e^-} = \sigma^{np} + \lambda_1\lambda_2\sigma_1, \tag{6.10}$$

with

$$\sigma_1 = \frac{4\sigma_0}{x_\lambda}\left[2\left(1+\frac{4}{x_\lambda}-\frac{8}{x_\lambda^2}\right)ln\frac{\sqrt{x_\lambda}+\sqrt{x_\lambda-4}}{2} - \left(1+\frac{4}{x_\lambda}\right)\sqrt{(}1-\frac{4}{x_\lambda})\right] \tag{6.11}$$

and

$$\sigma_1 = \frac{4\sigma_0}{x_\lambda}\left[2ln\frac{\sqrt{x_\lambda}+\sqrt{x_\lambda-4}}{2} - 3\sqrt{1-\frac{4}{x_\lambda}}\right]. \tag{6.12}$$

In these expressions x_λ=$4\omega_m\omega_0 = x^2/(x+1)/m^2$ whereas λ_1, λ_2 denote the initial state helicities. To see the relevancy of e^+e^- pairs creation, an pertaining evaluation of 6.12 should be performed. For example, $\sigma_{\gamma\gamma\to e^+e^-}$ turns out to be bigger than the Compton cross section by a factor 1.5 just for x = 10. However the maximum conversion efficient k is reduced in up to 30%. Thus for higher x does not necessarily means that an acceptable luminosity is guaranteed. So that one expects x $\leq$ 4.8 which is equivalent to have a $k \approx$ 0.4. For these values and a beam energy of 500 GeV one gets λ of order of 1μm which is compatible with high performance lasers. Furthermore, pairs creation dynamics is affected by non-linear corrections. It means that the pairs are created by the interaction of the high energy photons and several laser photons. An immediate consequence is the displacement of x what is shifted to $x_{eff} = 4.8(1+\eta^2)$ when the e^+e^- pair goes to superintense regime. In addition to pair creation, the complexity of the physics at the conversion region is manifested by the presence of

- Low energy electrons; what are produced because of multiple Compton scattering. Simulations have shown the minimum energy of an electron after of leaving the conversion region is of about 2% of its initial energy. This result partially serves for removing the disrupted electrons where in conjunction the disruption angle is also needed.

- Non-linear pair creation, which is possible because the non-negligible probability for collisions between several laser photons and the backscattered one below the single photon threshold $x = 4.8$.

[1] In his book, Landau *et* al [B$^+$71] have pointed out that P. M. Dirac was the first one in solving the cross section.

6.3 The Gamma-Gamma Luminosity

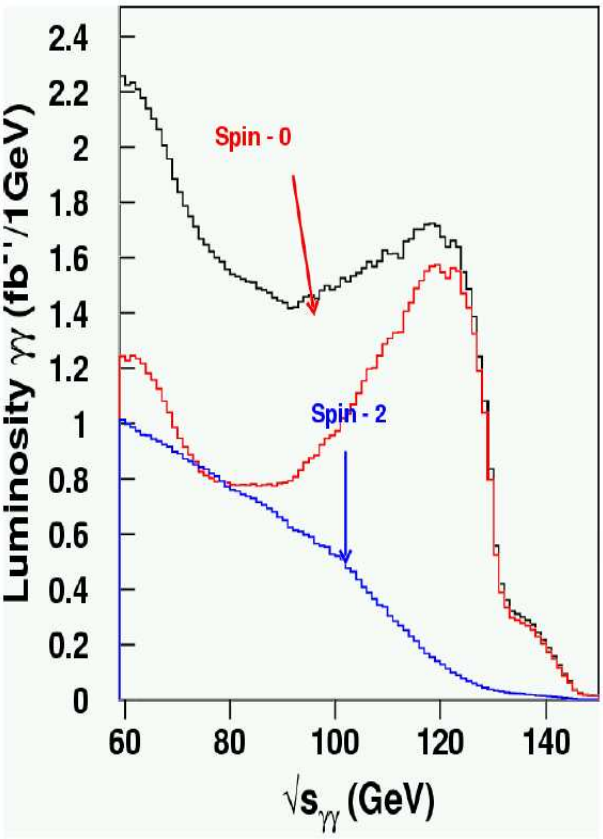

Figure 6.4: The integrated $\gamma\gamma$ luminosity for two spin configurations J = 0 (red line) and J = 2 (blue line) and the total integrated $\gamma\gamma$ luminosity (black line), for one year of running taken from [Hei05].

The $\gamma\gamma$ luminosity at the ILC is fixed by the geometric luminosity of electron beams [KT02]. Concretely, $L_{\gamma\gamma} \approx 0.1\ L_{geom}$, where $Lgeom = N_p^2 \nu\gamma/4\pi\sqrt{\epsilon_x\epsilon_y\beta_x\beta_y}$, where N_p denotes the number of particles, ν the frecuency, γ the Lorentz factor, ϵ the emmitances and β the beta functions. Therefore, to maximize the luminosity, is necessary to have smallest beam emmitances and beta functions. For nominal ILC parameters, one gets $L_{\gamma\gamma} = 3.5{\times}10^{33}\mathrm{c}m^2\mathrm{s}^{-1}$ which is valid for $W_{\gamma\gamma} > W_{\gamma\gamma,MAX}$ and it is $\approx 0.17\ L_{e^+e^-}$ [Tel06]. Since the $\gamma\gamma$ cross sections are bigger than the e^+e^- case, the event rate will be still larger than in e^+e^- collisions.

In Fig. 6.4 is shown the integrated $\gamma\gamma$ luminosity for one year of running and for two spin configurations by indicating that the case most advantageous

turns out to be for J = 0 or when the colliding photons have their helicities in opposite directions.

6.3.1 Measurement of the Gamma-Gamma Luminosity

The $\gamma\gamma$ luminosity at the high energy peak of the luminosity spectrum is proportional to the square of the function $f(x,y) = 1/\sigma_c \cdot d\sigma_c/dy$, which is actually the photon spectrum of Eq. 6.2. In order to determine the luminosity error, two techniques using dimuons final states were worked out by Telnov [I.95] and Mönig [M$^+$03]. Let us summarize both:

- $\gamma\gamma \to \ell^+\ell^-$. Using these processes ($\ell = \mu, e$), the luminosity can be determined only in collisions of photons with $|J|$=2. Because of its simple QED nature, the cross section reads like

$$\sigma_2(|cos\theta| < a) \approx \frac{4\pi\alpha^2}{W_{\gamma\gamma}^2}\left[2ln\left(\frac{1+a}{1-a}\right) - 2a\right], \tag{6.13}$$

  where θ denotes the angle between the beam pipe and the particle and $W_{\gamma\gamma}$ the $\gamma\gamma$ invariant mass. From a straightforward calculation for $\sigma(|\cos\theta|) < a$=0.9 and $\sqrt{s}_{e^-e^-}$= 0.5 TeV about 10^6 $\ell^+\ell^-$ pairs in the high energy peak are predicted. For a detection angle $\theta = 0.3$ rad, and one year running the expected statistical accuracy of the peak value of $dL/dW_{\gamma\gamma}$ is about 0.14% [I.95].

- $\gamma\gamma \to \ell^+\ell^-\gamma$. To measure the two photon width of the Higgs boson the J=0 mode is needed. In this case, the cross section of the process $\gamma\gamma \to \ell^+\ell^-$ is suppressed by a factor m_ℓ^2/s and the reaction cannot be used for luminosity determination. But, the radiative processes $\gamma\gamma \to \ell^+\ell^-\gamma$ has an additional final state photon thus the spin suppression is not longer valid. It means for the evaluation of the cross section the sum over all final state helicity configurations has to be performed. For $\cos\theta < 0.9$ and J=0 one gets a cross section for the $\gamma\gamma \to \ell^+\ell^-\gamma$ reactions, 820 fb. Therefore, a purity of 90% for the selected events is foreseen, by leading to a precision on the luminosity measurement of order of 1.0%, for a 2 GeV Higgs mass window, which is consistent with the detector acceptance [M$^+$03].

6.4 The Laser System and Optics

Turning now to the choice of laser, three basic types of laser may be considered: solid-state lasers, gas lasers, and free-electron lasers. Free-electron lasers technologies have evident advantages like tunable wavelength, adequate repetition rate and duration, and simplicity of synchronization [Tel06]. The laser parameters required for a photon collider are:

- Wavelength ~ 1 μm;
- Time structure $c\Delta t \sim 1000$ m, 3000 bunches/train; where the duration of one train containing 3000 bunches is 1 msec.
- Flash energy ~ 9 J;
- Pulse length ~ 1.5 ps.

The most attractive scheme for a photon collider with the ILC pulse structure is storage and recirculation of every powerful laser in a external optical cavity. Fig. 6.5 shows a possible layout of the optical system to be employed in the photon collider developed by Guido Klemz [Kle06]. Two optical cavities are requiered in this scheme. It is important to carry out electron-photon conversion efficiently, which depends in essence on the state-of-the-art of the telescopic ring cavities. Since the Compton conversion point is very close to the IP, the dimensions of the concave mirrors would have to be strongly correlated to the minimal collision angle α_0 defined as the angle between the direction of the laser and the electron beams [M$^+$06].

6.5 Modifications to the Proposed TESLA Detector

The realization of photon collider demands us to modify a few points indicated at the TDR [Ros03]. Since the backgrounds in the TESLA detector are driven by a large disruption angle as well as an angle between the outgoing beam and the magnetic field, there exists a possibility of a large background from pair production being smaller than in e^+e^- due to the anti-pinch effect. Due to a large disruption angle a crab crossing angle with $\alpha \approx 25$ mrad is required.

Because the imminent presence of a background tremendously large from pair production, is expected to have a negative influence on the gamma gamma physics. It can be suppressed by a proper layout of a mask of Tungsten in the forward region which would avoid to damage the pipes from

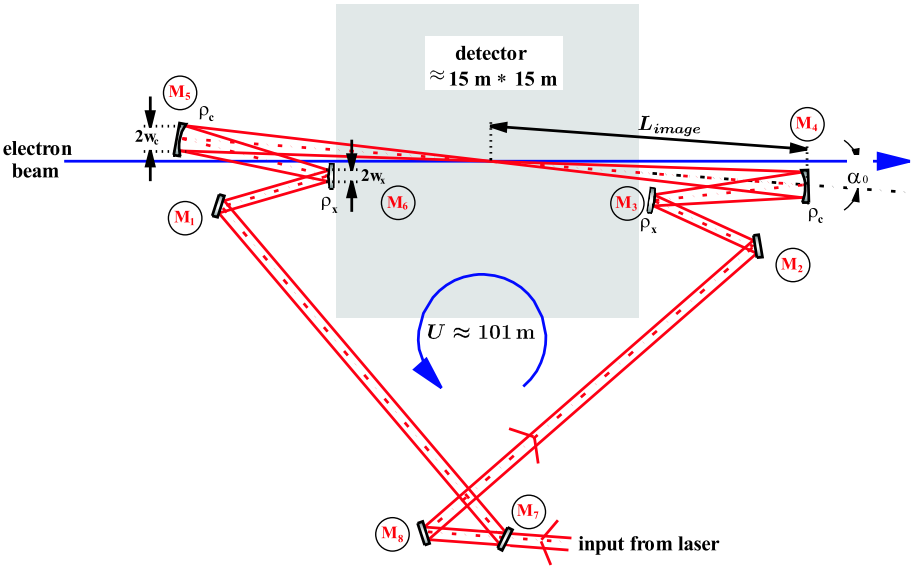

Figure 6.5: Sketch of a proposed optical cavity for the planned photon collider.

backscattered particles [M+06]. The most recent studies have shown that the optimum geometry for a cone-like mask builded of Tungsten should be greater than 100 and 23 cm of lenght for the inner and outer masks, respectively. In addition, to implement a mask, a minimum angle given by $\theta < 7.0$ degrees is required. In Fig. 6.6 a sketch of a possible configuration of the inner detector for the photon collider is shown. Also, the z-impact parameter defined as the z coordinate of the impact point in the x-y plane can be used to separate signal and pile-up events [Sch97], for such as requirement a beamspot lenght of approximately 200 μm is also needed.

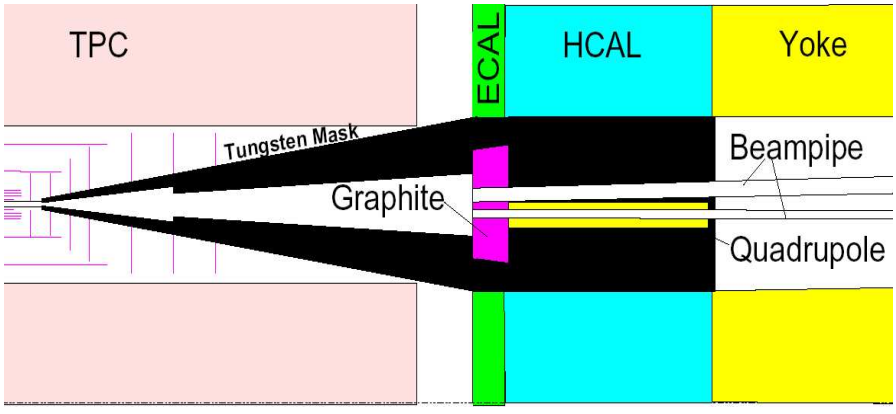

Figure 6.6: The x-z projection of the inner region of the $\gamma\gamma$ detector.

Chapter 7

Study of the 2-Muon and Missing Energy Final States at the ILC Photon Collider

7.1 Plan of the Simulation

Unlike the previous analysis performed for the right-handed smuon production in electron-positron collisions, the simulation of production of SUSY particles in photon-photon collisions involves special features due to the nature of the colliding photons, what are actually derived by Compton backscattering. Thus we have used the softwares which are capable to emulate in some extent the physics in the conversion point as well as in the interaction point.

Event Generation

- CompAz [Zar02]: This code is used to emulate the photon spectrum and it assigns a determined energy to the photon just created in the conversion point.

- SHERPA: [G$^+$04b]: It is the main code to be used in the rest of this thesis. The task of SHERPA is to generate the gamma-gamma reactions taking into account the initial energy of the colliding photons. In praxis, CompAz is already implemented in the code. In other words, SHERPA plays the role of simulating the interaction point and producing the final states according to the necessity of user. In contrast to PYTHIA, the code offers the possibility in producing the final states containing up to 6 particles final states.

- ISAJET: For the present case, SHERPA includes external supersymmetric spectra calculators. Nevertheless, the code has already implemented to ISAJET which provides the masses and widths of the superpartners.

- PYTHIA-CIRCE2 There are several cases where the interface of these two codes is used, basically in the lower energy region in which CompAz is limited for center-of-mass energies down to 200 GeV.

Fast Detector Simulation

As in chapter 5, the generated events are processed by SIMDET [Poh02]. For the present case, SIMDET considers the overlaying of generated events by pile-up events. These events are produced due to the huge effective cross section of the $\gamma\gamma \to q\bar{q}$ reactions ($\sigma \approx 10$ fb) and has strong impact on hadronic final states. Again, the subpackage SIANAL is used for an event by event analysis and storing of data.

Data Analysis

The analysis is performed in a very similar manner as that of the chapter 5. However, in some cases the analysis starts with the cleaning of sample of the pile-up events which affects strongly the low energy range down to 5 GeV. Once the sample is not affected by the pile-up ones, the background rejection strategy can be applied.

7.2 Determination of the Right-Handed Smuon Decay at 500 GeV

In photon collisions right-handed scalar muons are produced via s-channel. The reaction under study is quite simple and reads

$$\gamma\gamma \to \tilde{\mu}_R^+ \tilde{\mu}_R^- \to \mu^+ \tilde{\chi}_1^0 \mu^- \tilde{\chi}_1^0. \tag{7.1}$$

where the right-handed scalar muon decays promptly into a muon and neutralino. The experimental signatures or detected events shall be constituted by a muon pair accompanied of missing energy. The signature (7.1) is just compatible with the ones predicted by the mSUGRA model [BB99] or supergravity-inspired scenario where the lightest neutralino $\tilde{\chi}_1^0$ is candidate for being cold dark matter in universe [Mar06]. Furthermore this theoretical frame looks to be most suitable for an assessment of collider capabilities as

those performed in the past for the case of smuon mass determination in e^+e^- collisions [NC03] [Mar04]. Unless stated otherwise this note shall be based on the mSUGRA model and its variations. In general, the production of smuons in photon collisions is done inside the framework of QED. Logically it represents an advantage compared to e^+e^- collisions where the t-channel amplitudes for smuon pair production involve SUSY couplings. Hence, an analysis in the Born level is sufficient for our purposes. So that the corresponding cross sections for right-handed smuon production can be calculated directly [GK90]

$$\sigma_{\gamma_\pm\gamma_\pm} = \frac{2\pi\alpha^2}{s_{\gamma\gamma}}\beta(1-\beta^2)\{1+\frac{1-\beta^2}{2\beta}\ln(\frac{1+\beta^2}{1-\beta^2})\} \tag{7.2}$$

$$\sigma_{\gamma_\pm\gamma_\mp} = \frac{2\pi\alpha^2}{s_{\gamma\gamma}}\beta(1-\beta^2)\{3-\beta^2+\frac{1}{2\beta}(-3+2\beta^2+\beta^4)\ln(\frac{1+\beta^2}{1-\beta^2})\} \tag{7.3}$$

with β=$\sqrt{1-4m_{\tilde{l}}^2/s_{\gamma\gamma}}$ and $m_{\tilde{l}}$ the smuon mass. The importance of having polarizated beams is noted in the difference between (7.2) and (7.3). The case of interest for us is when $J=0$ ($\sigma_{\gamma\pm\gamma\mp}$) instead of $|J|=2$. The quantity $\sqrt{s}_{\gamma\gamma}$ denotes the center-of-mass energy constituted by the colliding photons. For values of slepton masses, ranging between 200 GeV and 500 GeV and a $\sqrt{s}_{\gamma\gamma}$ = 300 - 500 GeV one gets $\sigma_{\gamma\pm\gamma\mp} \approx 500$ fb. Of course, for the calculation of $\sigma_{\gamma\gamma}$ monochromatic photon beams are used, in contrast with a real $\gamma\gamma$ collider by which the colliding photons are produced by laser backscattering [Aru63]. Thanks to this phenomenon the electron can "transfers" up to 85% of its energy to the backscattered photons producing the spectra shown in Fig. 7.1 (top). We have used the `CompAZ` package [Zar02] for this exercise. The plots illustrate the transition from simple Compton to laser backscattering. As explained in Chapter 6, such a transition is controlled by the intensity parameter ξ^2 whose origin in related to secondary quantum effects. Consequently, Eqs. (7.2 - 7.3) cannot describe correctly the production of scalars and a further step to compromise the laser backscattering spectrum is needed. In effect, these cross sections would have to be convoluted in the following way

$$\sigma^{\lambda_1,\lambda_2}(\sqrt{s}_{e^-e^-}) = \int_{2\tilde{m}_\ell/\sqrt{s}_{e^-e^-}}^{x_{max}}\int_{z^2/x_{max}}^{x_{max}} 2zdz\frac{dx}{x}f_{\gamma e^-}^{P_k}(x_1,\lambda_1)f_{\gamma e^-}^{P_l}(\frac{z^2}{x},\lambda_2)\times \\ \times\,\sigma_{\gamma\gamma}(\sqrt{s}_{\gamma\gamma}=z\sqrt{s}_{e^-e^-}) \tag{7.4}$$

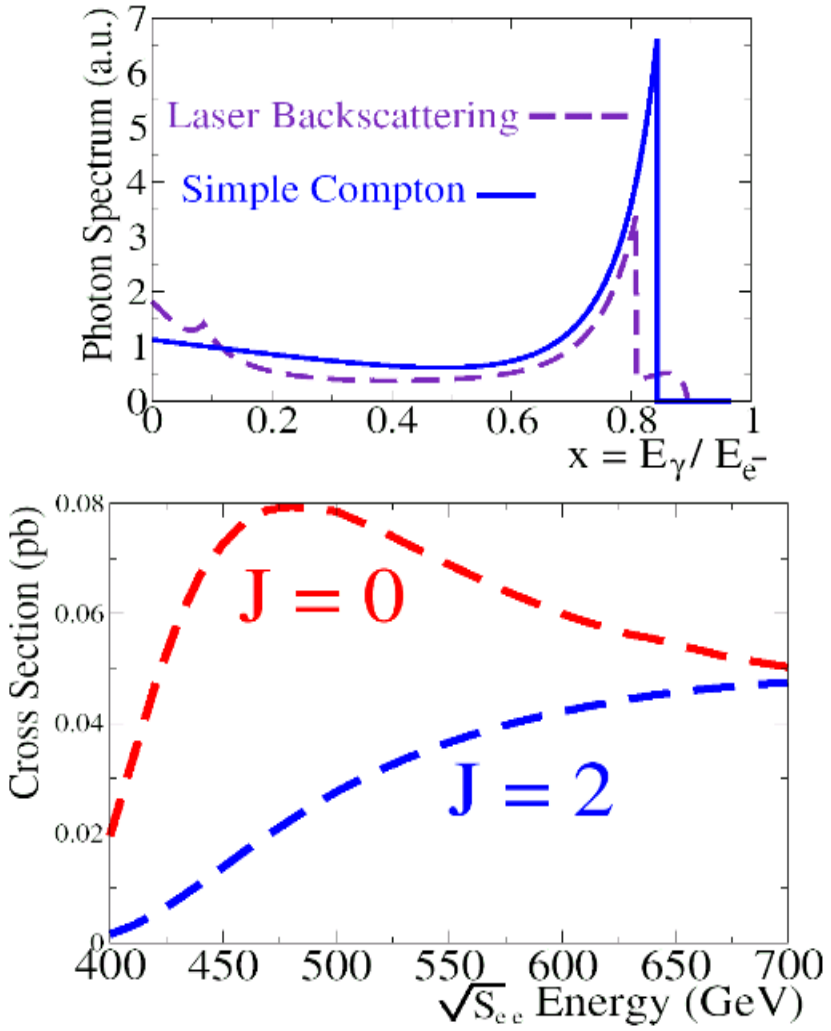

Figure 7.1: (Top) The photon spectrum simulated by CompAZ. The difference between Compton and laser backscattering is dictated by the nonlinear parameter ξ^2. (Bottom) The effective cross sections of $\tilde{\mu}_R^+\tilde{\mu}_R^-$ production in photon collisions for two spin configurations: J=0 and J=2.

where the $f_{\gamma e^-}(x_{1,2}, \lambda_{1,2})$ functions are associated to the laser backscattering, $\lambda_{1,2}$ the helicity of electrons, $P_{k,l}$ the laser beam polarisation, x_{max} the maximal fraction of transfered energy and $\sigma_{\gamma\gamma}$ the Born cross sections. Eq.7.4 is often called effective cross section. Fig.7.1 (bottom) displays the effective cross section obtained with the CompAZ-SHERPA [G$^+$04b] interface in function of incoming electrons energy indicating that the most convenient configuration is that of J=0. The effective cross sections $\sigma^{\lambda_1\lambda_2}$ were calculated by assuming a $\xi^2 \approx 0.4$. It is actually a crucial input to claim in some extent that the simulation is done under realistic conditions of a future ILC photon collider. Also, we have fixed the electron beam polarisation by a 85%. Thus $\sigma^{\lambda_1\lambda_2}(\gamma\gamma \to \tilde{\mu}_R^+\tilde{\mu}_R^-)$ had been computed for $\sqrt{s}_{e^-e^-}$=500 GeV yielding 76 fb. This encompasses possible scenarios that might be tested experimentally. Simulation for generating events of reactions (1) uses SHERPA interfaced to ISAJET [P$^+$03] by assuming the SUSY parameterization as given in the benchmark point SPS1a [GU02]. The resulting mass spectrum yields a smuon mass $m_{\tilde{\mu}_R} = 143$ GeV which surpasses in almost 20 GeV to the one computed with the SPS1a' parameters as observated in Chapter 5, whereas for the neutralino mass a value of 96 GeV have been obtained. In this section, a luminosity of 100 fb^{-1} is assumed.

For definition, this luminosity is taken in the high energy peak of the luminosity spectrum.

It suggests the simulation of 7600 signal events. The special usefulness of SHERPA is manifestly seen in the direct event generation (one step) of kind 2→4, i.e., $\gamma\gamma\to\ \mu^+\tilde{\chi}_1^0\mu^-\tilde{\chi}_1^0$. A notable property of $\tilde{\mu}_R \to \mu\tilde{\chi}_1^0$ decays constitute their simple topology. Because smuons are spin-0 species, muons are isotropically (not for J = 2) produced and the $E_{\mu^\pm}$ distribution acquires a box-like shape. It holds for a constant center-of-mass energy in the electron-positron system. Previous ILC studies, have demonstrated that the "geometry" of E_μ is sensitive to initial (final) state radiation and Beamstrahlung. These radiative processes are inherent to the lepton beams and therefore one expects that the E_μ distribution appears to be distorted yielding a E_μ distribution of a trapezoid-like shape [T$^+$95]. Nevertheless a precise measurement of sparticles masses would be possible by taking advantage of kinematical constrains as demonstrated in Chapter 5.

Unlike the e^+e^- machine, in a photon collider the kinematics of created sparticles depend on the laser backscattering spectrum strongly, since this mechanism controls the center-of-mass energy. For the present case of right-handed smuon production at $\sqrt{s}_{e^-e^-} = 500$ GeV, the endpoints of energy distribution given by $E^{lab}_{\mu,max,min} = \gamma(1 \pm \beta^*)\ E^{cm}_\mu$ with $\beta^* = \sqrt{1 - m^2_{\tilde{\mu}}/E^2_{\tilde{\mu}}}$ become severely damaged because the smuons are created in the high energy

region, closely to 195 GeV. This value have been actually displaced from its theoretical value given by 212.5 GeV as consequence of non-linear effects. Thus at first instance a study of right-handed smuon at photon collisions would not serve for mass measurement because of the evident disadvantage. Prematurely one can conclude that the $\gamma\gamma$ collider would actually have questionable aspects compared to the e^-e^+ machine and it would not guarantee positive prospects for physics studies. Nevertheless, the conclusion stated before is inexact and other positive aspects of photon collider should be exploited.

In effect, an interesting and promising direction that deserves to be explored is the measurement of branching ratio of smuons helped by the LHC-ILC information and supported by higher rates of smuon production. Expressed in a different manner, with the measured masses from LHC-ILC in hands, the decays

$$\tilde{\mu}_{L,R} \to \mu\tilde{\chi}_1^0 \tag{7.5}$$

can be reconstructed directly. Exist there various arguments by supporting the idea of a clean observation of these decays in photon collisions. One of them is the possibility in detecting SUSY signals with higher efficiencies because of the presence of a few SM (and SUSY in some cases) background processes associated. It will allow us to draw a simple strategy of noise discrimination which differs of those studies already performed for searching SUSY scalars at LHC-ILC.

7.2.1 Modeling of Signal and Background

For signal we have simulated 7600 events having lost 150 of them resulting in overall 7450 to be processed in further stages. The detector parameters used for the right-handed smuon studies in e^+e^- collisions (Chapter 5) have been again used as input in SIMDET, except the tracker acceptance whose functionality greater than 7 degrees is demanded. It is mandatory for a photon collider in accordance to its technical design, where the neccesity of having dead zones along the forward regions is emphasized. It explains the why in having lost events what are actually a consequence of vetoing the forward zones.

In contrast to the e^-e^+ case, the processing of events requires the overlaying of pile-up events derived from $\gamma\gamma \to q\bar{q}$ reactions what are expected to have a huge effective cross section $\approx 10^3$ fb (depending upon phase space cuts). Thus we are forced to overlay the pile-up ones onto the generated events by assuming 1.8 pile-up per bunching crossing.

The background processes are those which contain the signal topology

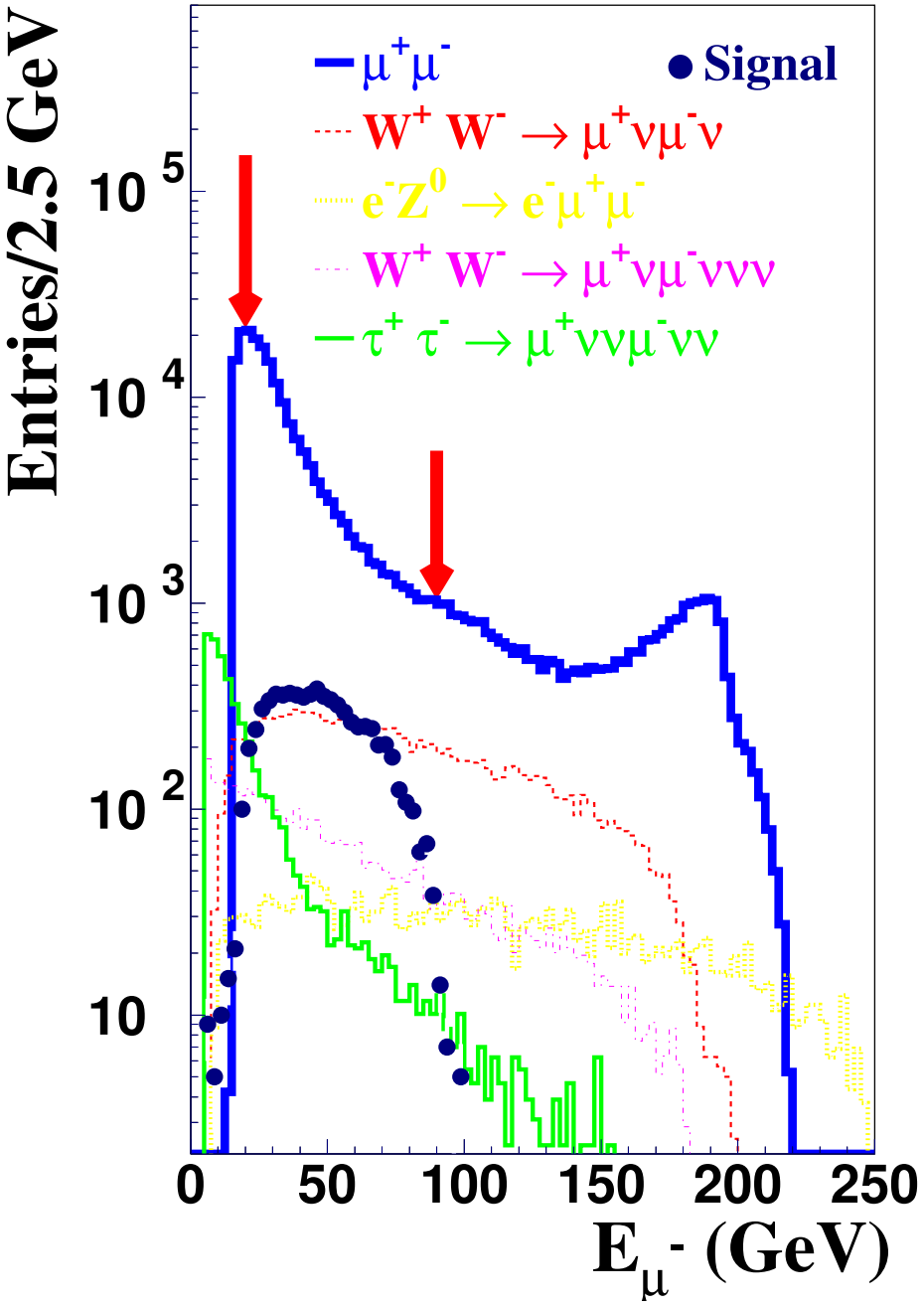

Figure 7.2: Muon (negative charge) energy distribution of signal (dots) and the most dangerous background processes. The signal is underneathed by a huge amount of SM background events produced in its $\gamma\gamma$ and $e^-\gamma$ modes.

made of a muon pair and invisible matter. These are listed below having written in brackets the responsible generator and their effective cross as well,

- $e^-\gamma \to e^- Z^0 \to e^-\mu^+\mu^-$ (SHERPA-ISAJET 41.8 fb);
- $\gamma\gamma \to W^-W^+ \to \nu\mu^+\nu\mu^-$ (PYTHIA-CIRCE2 202.6 fb);
- $\gamma\gamma \to W^-W^+ \to \nu\tau^\pm\nu\mu^\mp \to \nu\mu^+\nu\nu\nu\mu^-$ (PYTHIA-CIRCE2 70.2 fb);
- $\gamma\gamma \to \mu^-\mu^+$ (PYTHIA-CIRCE2 2500 fb);
- $\gamma\gamma \to \tau^-\tau^+ \to \mu^-\nu\nu\nu\mu^+\nu$ (PYTHIA-CIRCE2 72.5 fb).

where CIRCE2 [Ohl] is an alternative package interfaced to PYTHIA aimed to reproduce the laser backscattering spectrum. The usage of CIRCE2 is unconditional for generating events whose invariant mass lies below 200 GeV. We recall that the numbers correspond to the effective cross section.

It should be mention that the simulation for the $e^-\gamma$ reactions have considered a luminosity 1.5 times bigger that the $\gamma\gamma$.

In Fig. 7.2 the histograms corresponding to the muon (negative charge) energy for signal and its noise are plotted. At first glance, signal is completely indistinguishable mostly by dimuon processes followed by Ws, and to a lesser extent $e^-\gamma$ reactions.

7.2.2 Preselection and Selection

We have preselected events containing at least two muons with a minimum energy of 5 GeV for both charges. A remarkable point is that the pile-up events has not a substantial impact on the signal energy spectrum of preselected events. It is because the analysis involves uniquely muons instead of hadrons by which the pile-up ones might distort their energy distributions substantially. Since a small fraction of events were lost namely in the beam pipe and over the very forward region, 7450 and 249447 of signal and background events respectively passed the preselection. For optimization of signal statistics we appeal to a final selection. It is listed in Table 7.1. An efficient rejection of back-to-back dimuon processes occurs for values of ϕ greater than 3.13 (cut 1), resulting a signal purity of 18.97%. In this respect, it is noteworthy the reconstruction of the $\gamma\gamma \to \mu^+\mu^-$ processes that give us a key insight into the possible shape of laser backscattering spectrum as the one of Fig. 7.1 (top). In Fig. 7.2 the $\gamma\gamma \to \mu^+\mu^-$ histogram shows a peak close to 195 GeV by effect of non-linear corrections. It is also noted that the $\gamma\gamma \to \tau^+\tau^-$ histogram is characterized by a major population of low energy events down to 10 GeV. To reject substantial noise, events around the region limited by

the expected endpoints are accepted. Consequently, cuts on the energy muon (both charges) are logically applied. In reality these cuts do not match the ones computed by two body decay and thus we kept the region between 20 GeV and 87 GeV (cut 2) in which one gets a major reduction of background. This operation makes maximum the product $\epsilon \cdot \mathrm{p}$ (ϵ = efficiency and p = purity). In Fig. 7.2 the position where cuts were posed is indicated. (Note that for pedagogical reasons we have preservated the histogram of $\gamma\gamma \rightarrow \mu^+\mu^-$ events). For this procedure, a precise knowledge of smuon and neutralino masses are requiered. We underline the assumption in knowing some SUSY particles masses what are provided by the LHC-ILC measurements. It actually provides an advantage in the analysis. Hence, signal purity and

Cut	Signal	Background	Efficiency(%)	Purity(%)	$\frac{\Delta N_s}{N_s}$ (%)
	7450	249447	100.0	2.9	6.8
1	7408	31643	99.50	18.97	2.67
2	6536	5205	87.77	55.67	1.65
3	6324	4278	**84.93**	**59.65**	**1.63**

Table 7.1: Statistical behavior of signal and background events.

efficiency are increased in up to 55.7% and 87.8% respectively. Despite of applying this important discrimination, even is noted a little contamination by the $\gamma\gamma \rightarrow \tau^+\tau^-$ events populating the low energy region as well as the $\gamma e^- \rightarrow Z^0 e^- \rightarrow e^-\mu^+\mu^-$ events containing energies inside the range 1 GeV $< E_\mu <$ 250 GeV. The applied cuts have demonstrated a certain effectivity since the signal is already distinguishable but a further cut is still needed, aimed to defeat those events from the $e^-\gamma$ mode.

Finally, in top panel of Fig. 7.3 the $(E^+ - E^-)/P_{Miss}$ variable for remaining histograms are plotted. It manifestly exhibits space to apply cuts and thus the region limited by $|(E^+ - E^-)/P_{Miss}| < 0.65$ is kept (cut 3), reaching a purity of 59.7%.

Fig 7.3 (bottom) displays final histograms after cuts showing even remaining WWs events over the energies where signal is distributed. It happens because the ratio $\sigma_{W^+W^-\rightarrow\mu\mu\nu\nu}/\sigma_{\tilde{\mu}_R\tilde{\mu}_R\rightarrow\tilde{\chi}_1^0\mu\tilde{\chi}_1^0\mu} \approx 3$ and both smuon and W decays are quite similar. A point of importance that deserves to be commented is the weak impact of the whole cut procedure on the signal energy spectrum having left almost intact its triangular shape as initially seen in Fig. 7.2. While the background appears to be flat, the signal spectrum have turned out to be peaked around 40 GeV. Of course, one can apply further cuts to improve signal statistics but the present analysis is aimed to demonstrate that the application of a simple discrimination strategy is enough to

cut away noise considerably.

7.2.3 Interpretation of the Relative Error

In Table 7.1 it was defined the relative statistical error already defined in Eq. (5.4). Similarly, for the present case

$$\frac{\Delta N_i}{N_i} = \frac{1}{\sqrt{N_i \cdot \epsilon \cdot \mathrm{p}}} \tag{7.6}$$

where N_i the number of signal candidates or number of events before cuts. Since the branching ratio enters quadratically in the cross section, a relation to calculate the branching ratio error from (7.6) can be inferred,

$$\frac{\Delta \mathrm{B}r}{\mathrm{B}r} = \frac{1}{2}\frac{\Delta N_i}{N_i} = \frac{1}{2}\frac{1}{\sqrt{N_i \cdot \epsilon \cdot \mathrm{p}}} = \frac{1}{2} \cdot 1.63 = 0.82\%. \tag{7.7}$$

Inserting ϵ and p into (6) a relative statistical error of 1.63% is gained. It is equivalent to say that the measurement of decay $\tilde{\mu}_R \rightarrow \mu\tilde{\chi}_1^0$ in up to a 0.82% might be reached, solely for models where right-handed smuon present uniquely a decay channel. For such estimate, Eq. (7.7) was used. The obtained precision is actually remarkable since we have simulated the scrutiny of data for a luminosity of 100 fb^{-1}, corresponding to a bit more than 30 days of collected data. A few systematic uncertainties had been assigned to the results and all of them will be discussed later.

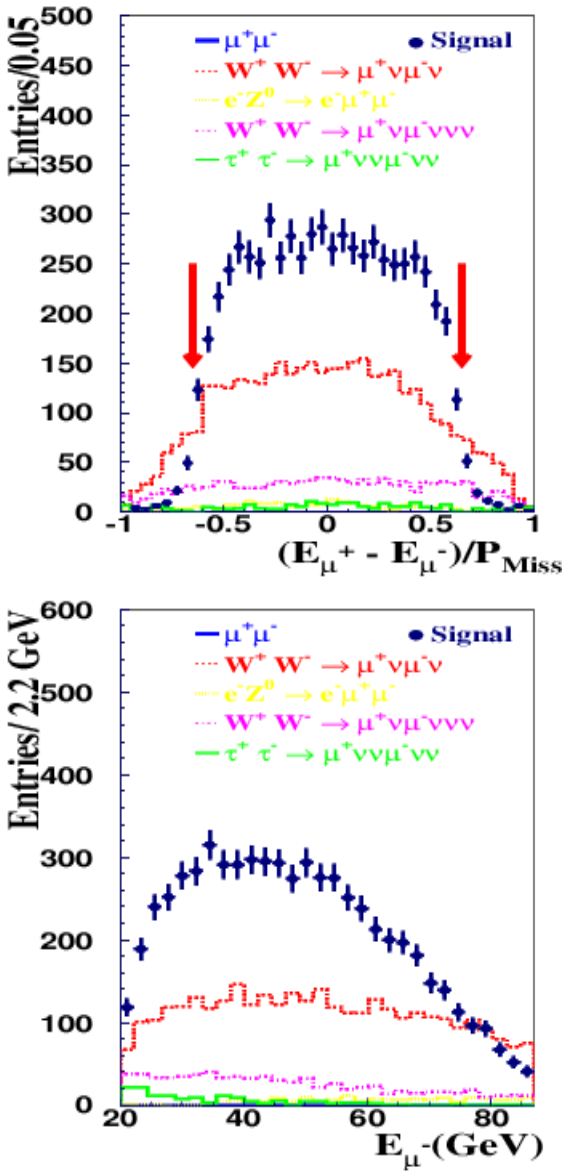

Figure 7.3: (Top) The $(E^+ - E^-)/P_{Miss}$ variable for signal and background showing the position of cuts applied. (Bottom) The resulting muon energy distributions. Note the peaked behavior of SUSY signal against the remaining background.

7.3 Determination of the Left-Handed Smuon Decay at 600 GeV

In previous analysis, the right-handed smuon have been examinated by means its $\tilde{\mu}_R \rightarrow \tilde{\chi}_1^0 \mu$ decay having reached a relative statistical error of 1.63% for signal identification. The importance of this result lies not only in such number but rather in the possibility in getting a similar statistics for the $\tilde{\mu}_L \rightarrow \tilde{\chi}_1^0 \mu$ decay by using a similar strategy. We remind that the strategy was that of applying a few cuts. In SPS1a, the left handed smuon presents a

-

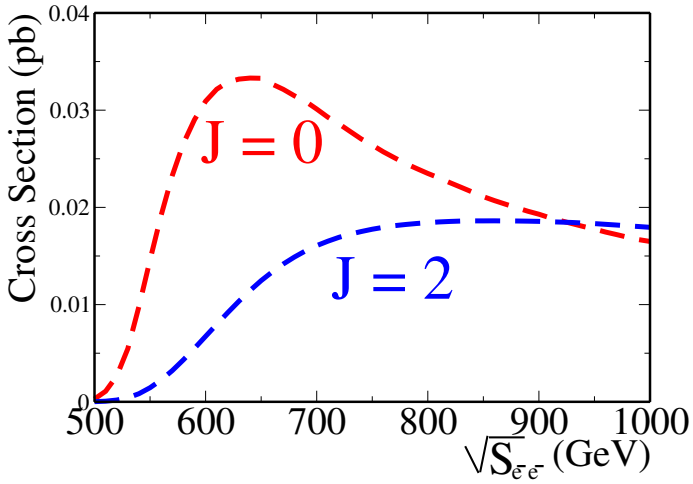

Figure 7.4: The effective cross sections of $\tilde{\mu}_L^+ \tilde{\mu}_L^-$ production at the photon collider for two spin configurations: J = 0 and J = 2.

mass of 204 GeV [P+03] by suggesting its possible observation at the photon collider for available center-of-mass energies. We shall focus on its decays instead of mass or spin measurements what might be already known from the LHC-ILC experiments. It is very important to note that the obtained results in conjunction to those already presented for right-handed smuons would led us to have a clear picture about the role which should play the ILC photon collider for SUSY studies.

The idea of a precise branching ratio determination comes from the possibility of having large rates as is demonstrated in Fig. 7.4. There, the effective cross section suggests to perform the studies at the J = 0 configuration. The figure indicates there that a $\sqrt{s}_{e^-e^-} = 600$ GeV is the most favorable, by which one expects a $\sigma^{\lambda_1,\lambda_2} = 30$ fb. The curves had been obtained with

the CompAZ-SHERPA interface. An interesting feature of left-handed superpartner consist in its decays given by

$$\tilde{\mu}_L \to \mu\tilde{\chi}_1^0 \qquad (55\%), \tag{7.8}$$

$$\tilde{\mu}_L \to \mu\tilde{\chi}_2^0 \qquad (17\%), \tag{7.9}$$

$$\tilde{\mu}_L \to \nu\tilde{\chi}_1^{\pm} \qquad (28\%), \tag{7.10}$$

where the SPS1a scenario is assumed. The most interesting case occurs when both $\tilde{\mu}_L^{\pm}$ has the same decay (7.8) producing the final states as indicated in (7.1). Identification of such events become useful for a measure of channel, using similar arguments as the case of the right-handed smuon analysis. It should be noted that the final states shall contain a mix of species since for the cases (7.9) and (7.10) the $\tilde{\chi}_2^0$ and $\tilde{\chi}_1^{\pm}$ suffer of cascade decay [Cuy93] as the following channels $\tilde{\chi}_2^0 \to \ell^{\pm}\tilde{\ell}^{\mp}$ with $\ell = e, \mu, \tau$ are contemplated, whereas $\tilde{\chi}_1^{\pm} \to \tilde{\tau}_1^{\pm}\nu$. For SPS1a, the latest has a branching ratio of (90%) and could be taken as a promising channel to evaluate photon collider capabilities. But such channel offers a certain degree of difficulty because of the production of several enflo at the final states, what are actually entangled with those of pile-up at the low energy region. This situation makes quite hard either identification or extraction of signal events. A Monte Carlo study performed in the past [KM05] had pointed out the necessity of applying dedicated strategies for extraction of SUSY signals originated by chargino decays. In these studies, an overall resolution of order of 10% was gained. One of the reasons why we shall constrain ourselves to select events containing muons instead of other species is the possibility in reconstructing SUSY observables with efficiencies above 30%.

7.3.1 Analysis of the Main Decay

The identification of events

$$\gamma\gamma \to \tilde{\mu}_L^+\tilde{\mu}_L^- \to \mu^+\tilde{\chi}_1^0\mu^-\tilde{\chi}_1^0 \tag{7.11}$$

constitutes a direct way to measure the main decay of left-handed smuon. In order to be realistic, 30000 $\tilde{\mu}_L^+\tilde{\mu}_L^-$ pairs were simulated and thereby allowing them to decay to their correspondent probabilities in a two-step procedure as follows: SHERPA-ISAJET had been used for producing the $\tilde{\mu}_L^+\tilde{\mu}_L^-$ pairs, whereas PYTHIA had been employed for allowing the subsequent decay of smuons. This step guarantees the presence of background events produced by the left-handed smuon itself. The relevant processes at these studies are listed below,

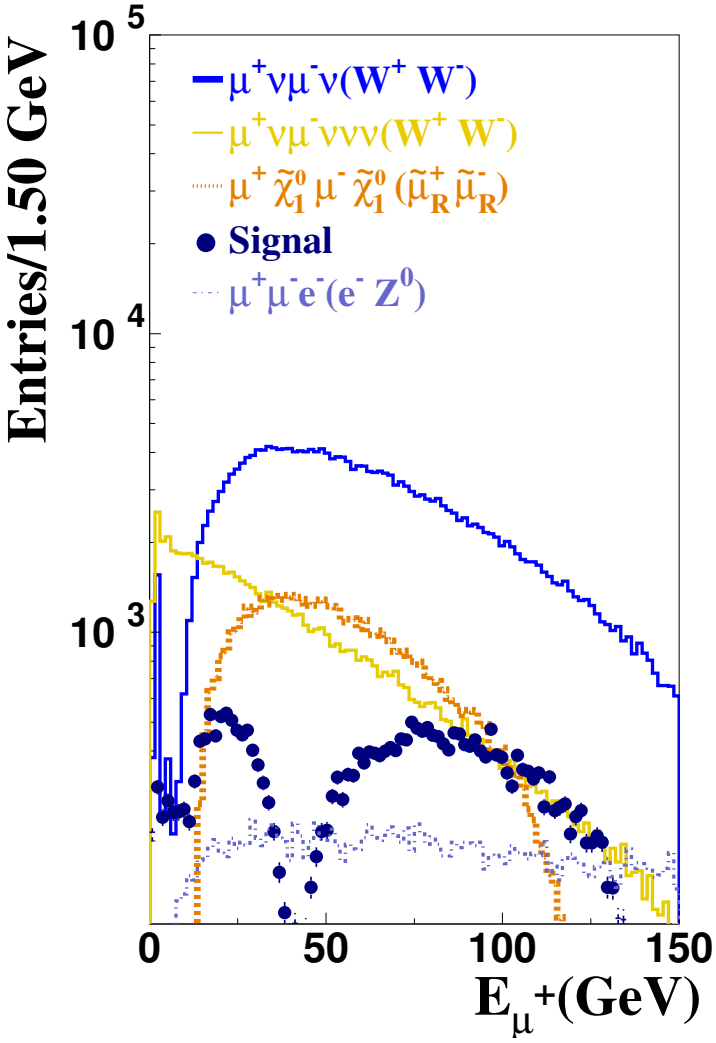

Figure 7.5: Energy distributions of signal (bars) and its corresponding background. Note the composition of the signal distribution because the $\tilde{\mu}_L \to \tilde{\chi}_1^0\mu$ and $\tilde{\mu}_L \to \tilde{\chi}_2^0\mu$ decays. The knowledge of the $\tilde{\mu}_L$ and $\tilde{\chi}_1^0$ masses would led to reject a considerable amount of background events. For the sake of the simplicity we have omitted the $\gamma\gamma \to \mu^+\mu^-$ reactions what are not relevant anymore.

- $e^-\gamma \to e^- Z^0 \to e^-\mu^+\mu^-$ (SHERPA 27.83 fb);
- $\gamma\gamma \to W^-W^+ \to \mu^+\nu\mu^-\nu$ (PYTHIA-CIRCE2 200.32 fb);
- $\gamma\gamma \to W^-W^+ \to \tau^\pm\nu\mu^\mp\nu \to \mu^\pm\nu\nu\nu\mu^\mp\nu$ (PYTHIA-CIRCE2 69.40 fb);
- $\gamma\gamma \to \tau^+\tau^- \to \mu^+\nu\nu\mu^-\nu\nu$ (PYTHIA-CIRCE2 72.5 fb);
- $\gamma\gamma \to \tilde{\mu}_R^+\tilde{\mu}_R^- \to \tilde{\chi}_1^0\mu^+\tilde{\chi}_1^0\mu^-$ (SHERPA-ISAJET 56.30 fb).

In brackets, generators and effective cross sections are specified. Clearly, one can identify to Ws as the major source of noise in both aspects, quantitatively and topologically. We have discarded the presence of $\gamma\gamma \to \mu^+\mu^-$ reactions or dimuon events from the beginning of analysis. Approximately a 99.9% of them, are defeated by preselection as shall be explained in next section. For the case of staus, they were simulated by means a two-step procedure, exactly the one used for signal generation. Firstly, the 2→2 reactions

- $\gamma\gamma \to \tilde{\tau}_1^+\tilde{\tau}_1^-$ (SHERPA-ISAJET 60.80 fb);
- $\gamma\gamma \to \tilde{\tau}_2^+\tilde{\tau}_2^-$ (SHERPA-ISAJET 29.00 fb);

denoting in brackets the generator responsible and effective cross section. Secondly, both staus were allowed to decay by respecting their branching ratios. The latest step uses PHYTHIA. Despite that the staus effective cross section are of order of 60 fb their contribution to the total background had turned out to be negligible because of the factor $(0.173)^2$. Turning now to Fig. 7.5 we have plotted E_{μ^+} for all relevant processes involved. Initially, the signal is tremendously overwhelmed by SM and SUSY backgrounds. There is noted the presence of a dip forming two well pronounced sectors due to that the muons came substantially from decays namely (7.8) and (7.9). This bizarre shape of energy distribution has its origin in the triangular nature of muon energy spectra which is certainly consistent with the one of right-handed partner. A logical hypothesis would rule out such shapes to a mostly general rule by which at least energy spectra of detected leptons derived from the $\tilde{\ell}_L \to \ell\tilde{\chi}_2^0 \to \ell\bar{\ell}\ell\tilde{\chi}_1^0$ decays must obey to a peaked or triangular nature.

In view of Fig. 7.5, the resulting signal histogram consists in two well-defined regions and their kinematical constrains are given by

$$\tilde{\mu}_L \to \mu\tilde{\chi}_1^0 \qquad (41\mathrm{G}eV < E_\mu < 153\mathrm{G}eV), \tag{7.12}$$

$$\tilde{\mu}_L \to \mu\tilde{\chi}_2^0 \qquad (11\mathrm{G}eV < E_\mu < 41\mathrm{G}eV), \tag{7.13}$$

what are derived from two body decay formulae. Even though we will not discuss here the origin of both the splitting and dip in terms of SUSY parameters space, one can argue that the areas viewed in signal histogram of Fig. 7.5 are proportional to the respective branching ratios. It is easy to note that the splitting of signal histogram gives rise to a major concentration of events over the region between 41 GeV and 153 GeV in agreement to (7.8), which is the region of particular interest.

The next task is the identification of signal events and for this purpose the left-handed smuon mass must be known accurately.

Preselection

Apart from the distinctive signature for smuons what consists in two acoplanar muons and missing energy and momentum, we have applied two cuts for preselection of signal events.

Firstly, the zone limited by 53 GeV and 143 GeV which are inside the kinematical range denoted in (7.12) is accepted. It is the most important discrimination in the analysis. Of course the knowledge of left-handed smuon and neutralino masses provides evidently an advantage.

Secondly, those events belonging to the range $0.6 < \phi < 3.13$ rad are accepted. As an immediate consequence of this cut the back-to-back $\gamma\gamma \to \mu^+\mu^-$ reactions were defeated in a 99.5%. The remaining events do not have an relevant impact on signal in the rest of analysis. For the sake of simplicity the histogram of these reactions were not plotted in Fig. 7.5 and also not considered in the analysis anymore. Aside from the $\gamma\gamma$ mode, the $e^-\gamma \to e^- Z^0$ also contributes with a sizeable amount of events just above 50 GeV, the region where signal distribution is located. It is because $\approx 80\%$ of $\sqrt{s}_{e^-\gamma}$ is transfered to the Z^0 boson and as consequence muons acquire energies up to 250 GeV.

In addition the SUSY backgrounds $\tilde{\tau}^+_{1,2}\tilde{\tau}^-_{1,2}$ were rejected in a 95%. In the following, these SUSY reactions are not considered. A special case turns out to be the $\tilde{\mu}^+_R\tilde{\mu}^-_R$ processes having noted that they still do survive after the preselection.

Respect to the signal one would expect $\mathcal{L} \cdot \sigma \cdot \mathrm{B}r(\tilde{\mu}_L \to \mu\tilde{\chi}^0_1)^2 = 9030$ events, however we have preselected 8344 signal events because cuts were applied closely to the theoretical endpoints yielding a lost in a small percent, whereas the total background is reduced $\approx$ in a 30%.

Selection and Final Statistics

The final selection of events have considered the cut variables listed Table 5.2. To enhance the purity by a factor 2, events with cosθ > -0.5 are accepted (cut 1). The effect of this cut is observed in top panel Fig. 7.6 where the Ws and $\tilde{\mu}_R^+\tilde{\mu}_R^-$ processes become seriously affected. However the cut does not affect the $\gamma e^- \to Z^0 e^-$ processes leaving untouched their distribution. In this case the Z^0 boson goes through a hemisphere featuring its $\mu^\pm$ pair to have a small opening angle θ. After of applying this cut a 30% of signal events are lost. The bottom panel of Fig. 7.6 displays the histograms for $P_{\mathrm{m}iss}$. A comparison between the signal and background histograms have suggested that a cut on 100 GeV has to be applied (cut 2). It is sustained by the fact that the signal inherently presents a considerable missing energy while most of the background histograms constituted by SM processes present a smooth behavior beyond 100 GeV.

Consequently a 90% of events produced by the right-handed smuon were discarded. Thus the signal purity increases in a 17%. In top panel of Fig. 7.7 the P_T distribution is displayed. The behavior of histograms accentuates the need in to apply a cut on $P_T = 90$ GeV (cut 3) where the major background, the Ws, turns out to be substantially affected. Note that signal histogram consists of events containing a P_T extended up to 180 GeV. For this reason the cut does not degrade the signal statistics but rather it increases its purity.

It is observed that the P_T cut does not substantially affects the distribution of events from the $\gamma e^- \to Z^0 e^-$ processes what behaves in somewhat like signal P_T distribution. On the other hand, this cut eliminates almost all the events derived from $\tilde{\mu}_R^+\tilde{\mu}_R^-$ pairs. Statistically the accomplishments of applied cuts so far is reflected in a signal purity of 54%. Since the events from the $\gamma e^- \to Z^0 e^-$ processes still persist we appeal finally to use the invariant mass defined by two muons what would reconstruct the Z^0 boson mass. It serves to pose cuts around the Z^0 mass, $M_{Z^0} \pm \Gamma_{Z^0}$) as the efficient reconstruction of the Z^0 boson had been possible (cut 4). This cut reduces the events from $e^- Z^0$ in a 90%. Thus signal purity and efficiency have reached a 74% and 42% respectively. The resulting histograms for energy distribution are plotted in bottom panel of Fig. 7.7. Favorably, signal spectrum significantly surpasses the background what is dominated by Ws over the lower region. Apart from the impressive statistics seen in Table 7.2, the signal maintains almost intact its initial (before cuts) triangle-like shape. Besides the flatness of remaining backgrounds events such as those coming of Z^0 ($e^-\gamma \to e^- Z^0$) (minor) and Ws processes, we clearly note that the peaked signal energy distribution stands in contrast to them.

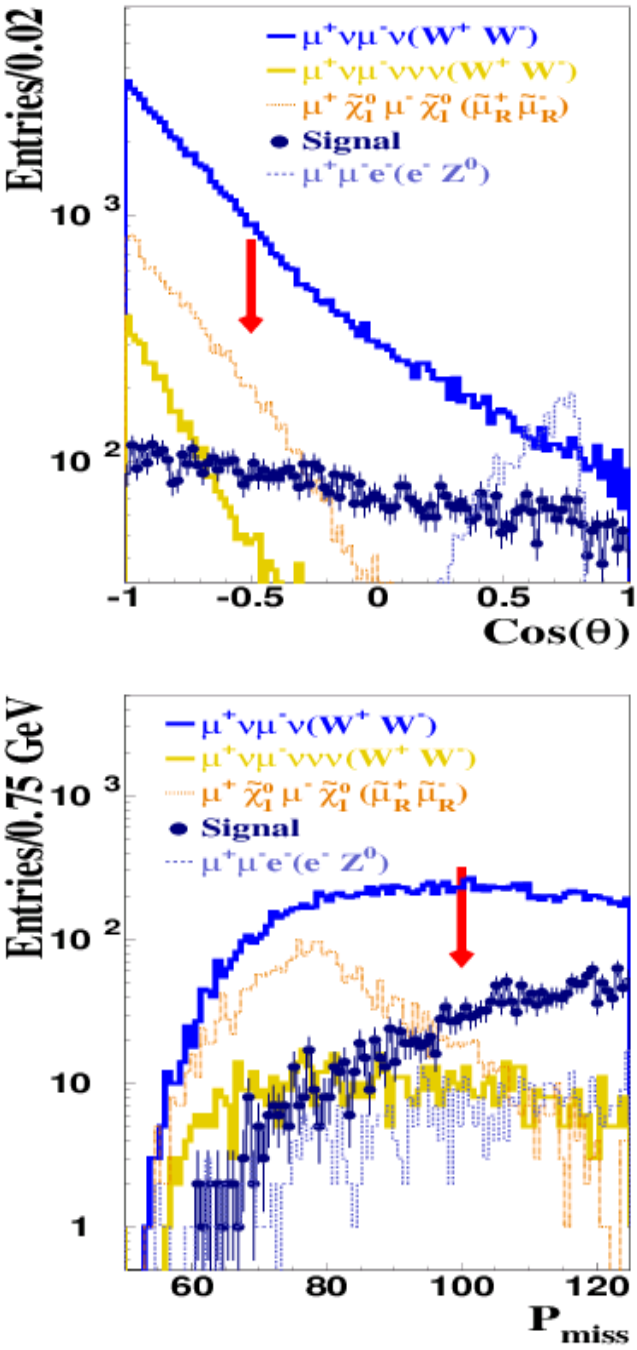

Figure 7.6: (Top) The cosθ distribution for signal (error bars) and background is plotted. The arrows indicate the position of the cuts to be applied. (Bottom) The missing momentum distribution. According to the plot, a cut on 100 GeV would have to be applied.

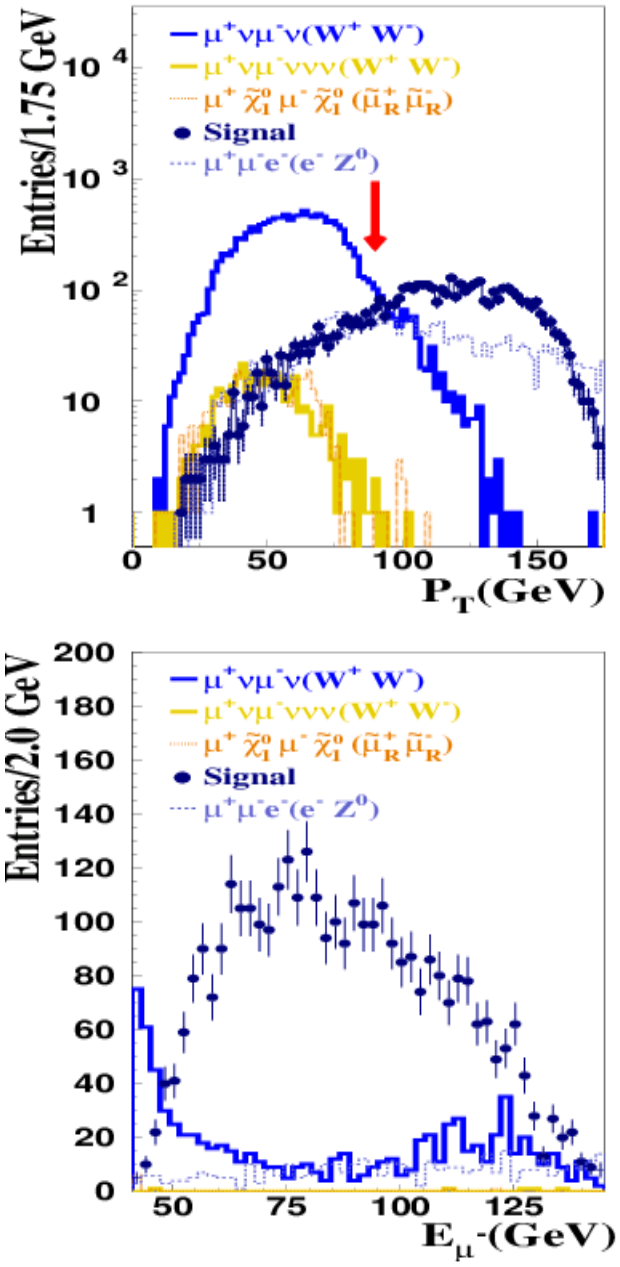

Figure 7.7: (Top) The transversal momentum distribution for signal (error bars) and background indicate that a cut on 90 GeV must be applied. (Bottom) Muon energy spectra after cuts showing to the Ws as the major source of irreductible background.

Cut	Signal	Background	Efficiency(%)	Purity(%)	$\frac{\Delta N_{1s}}{N_{1s}}$ (%)
	8344	142542	100.00	5.53	4.65
1	5761	55396	69.04	9.42	4.29
2	4981	24216	59.69	17.06	3.43
3	3642	3054	43.65	54.39	2.25
4	3506	1222	**42.02**	**74.15**	**1.96**

Table 7.2: Statistical behavior of signal and background events. Note that N_{1s} denotes the number of signal events before cuts.

Interpretation of the Results

The effectiveness of the set of cuts used in the analysis is reflected in the relative statistical error $\Delta N_{1s}/N_{1s} = 1.96\%$. In a similar manner from previous studies performed for right-handed smuons, the branching ratio enters quadratically in the cross section and therefore the relative statistical error of $\mathrm{Br}(\tilde{\mu}_L^{\pm} \to \mu^{\pm}\tilde{\chi}_1^0)$ can be written as

$$\frac{\Delta \mathrm{Br}(\tilde{\mu}_L \to \mu\tilde{\chi}_1^0)}{\mathrm{Br}(\tilde{\mu}_L \to \mu\tilde{\chi}_1^0)} = \frac{1}{2}\frac{\Delta N_{1s}}{N_{1s}} = 0.98\%. \tag{7.14}$$

This result constitutes a positive aspect to favour of a photon collider as to SUSY studies and ensures the smallness of the measurement of left-handed smuon decays. It is noteworthy that this result cannot be extracted from the LHC and ILC (e^+e^- mode) measurements. Note that this measurement assumes sparticle masses in the Z^0 scale.

7.3.2 Measurement of Minor Left-Handed Smuon Decays

In this part we take up the second channel, namely that the left-handed smuon decays promptly into a muon and a heavy neutralino $\tilde{\chi}_2^0$. The strategy for a measuring of branching ratio consists in to preselect events as follows

$$\gamma\gamma \to \tilde{\mu}_L^+\tilde{\mu}_L^- \to \mu^+\tilde{\chi}_2^0\mu^-\tilde{\chi}_1^0, \tag{7.15}$$

for what one smuon would decay into $\mu\tilde{\chi}_2^0$, while the one of opposite charge goes into $\mu\tilde{\chi}_1^0$. It implies again to take advantage of knowledge of SUSY masses for fixing the kinematical limits of muon energy in which the preselected events has to be constrained in according to (7.12) and (7.13). Furthermore the manner of selecting candidates indicated in (7.15) is based on the idea that this acceptance maximizes the initial number of events to be processed through the final selection.

We stress the fact that the way in selecting candidates using the combination of channels (7.12) and (7.13) has the disadvantage of including additional species as consequence of neutralino $\tilde{\chi}_2^0$ decays.

There is also background derived from the left-handed smuon itself. For this case, the most important background events coming from the combination of (7.8) and (7.10).

Concerning the background events produced partially by chargino decays, they mimics the signal ones and are going to populate the low energy region between 1 GeV and 30 GeV. The chargino suffers of cascade decay in the following way

$$\tilde{\chi}_1^{\pm} \to \tilde{\tau}_1^{\pm}\nu \to \tau^{\pm}\tilde{\chi}_1^0\nu \to \mu^{\pm}\nu\nu\tilde{\chi}_1^0\nu \tag{7.16}$$

with the number in brackets indicating the product of branching ratios involved. Thus, those muons emerging from (7.16) mimic seriously the signal and therefore shall be considered as a systematic in the results.

Decays of Heavy Neutralinos

In collider physics, often one try to understand the dynamics of $\tilde{\chi}_2^0$ a key sparticle wich could be comfortably seen at LHC [Mon96] within an exceptional resolution. In a vast region of parameter space, a typical decay chain is that of $\tilde{\chi}_2^0 \to \tilde{\chi}_1^0\ell\bar{\ell}$ where two leptons are emanated. Under the assumption of SPS1a [Mar04], $\tilde{\chi}_2^0$ has a mass of 182 GeV, and admits the following channels (numbers computed by `ISAJET`),

$$\tilde{\chi}_2^0 \to \tilde{\mu}_R^{\pm}\mu^{\mp} \to \mu^+\mu^-\tilde{\chi}_1^0 \qquad (6.6\%) \tag{7.17}$$

$$\to \tilde{e}_R^{\pm}e^{\mp} \to e^+e^-\tilde{\chi}_1^0 \qquad (6.6\%) \tag{7.18}$$

$$\to \tilde{\tau}_1^{\pm}\tau^{\mp} \to \tau^+\tau^-\tilde{\chi}_1^0 \qquad (86.8\%). \tag{7.19}$$

with the numbers in brackets denoting the corresponding branching ratios. It actually tell us the final states derived from $\tilde{\chi}_2^0$ are plagued of abundant species due to tau decays. The existence of this diversity of particles cannot be evaded and thus additional `e`nflo should be taken into account together with the muon pair through preselection of events. The simulation have revealed the net number of registered species can reach up to 50 `e`nflo, as consequence of tau hadronic channels plus the pile-up events. So that the candidates (7.15) should be made of two muons of opposite charge plus secondary leptons, several hadrons and photons, and missing energy.

Cut	Signal	Background	Efficiency(%)	Purity(%)	$\frac{\Delta N_{2s}}{N_{2s}}$ (%)
	8438	157338	100.00	5.09	4.82
1	5479	63963	64.93	7.89	4.81
2	3489	27774	41.35	11.16	5.07
3	2831	9064	**33.55**	**23.80**	**3.85**

Table 7.3: Statistical of signal and background events by effect of applied cuts.

Preselection and Selection

We have used the same sample used for the study of $\tilde{\mu}_L^{\pm} \to \mu^{\pm}\tilde{\chi}_1^0$ decays, for the present case. The preselection of events as written in (7.15) have demanded to accept at least two muons of opposite charge whose energies are inside the ranges (7.12) and (7.13) and up to 10 enflo. As consequence N_{2s}=8438 signal events were preselected. Note that this number surpasses the value obtained by $2{\cdot}\sigma \cdot \mathcal{L} \cdot \mathrm{Br}(\tilde{\mu}_L \to \mu\tilde{\chi}_1^0) \cdot \mathrm{Br}(\tilde{\mu}_L \to \mu\tilde{\chi}_2^0) = 5570$, where (7.8) and (7.9) are used. It reveals that N_{2s} have exceeded its nominal value in around 2800 events being the range given by (7.13) the most contamined. In order to appreciate differences with respect to behaviors between signal and backgrounds we have preferably plotted the $\mathrm{E}_{\mu^-} + \mathrm{E}_{\mu^+}$ variable in Fig. 7.8. A rather economic way to care the signal events is to keep the region between 150 GeV and 220 GeV (cut 1). As consequence, e^-Z^0 processes are almost rejected. In addition Ws and right-handed smuons are affected and both backgrounds lost a 75% of their events. The top panel of Fig. 7.9 shows the missing mass distributions and the position of the applied cut. We have accepted events with a missing mass below 410 GeV where the product efficiency times purity has its maximal value (cut 2). Roughly half of Ws events were discriminated, while the events coming from $\tilde{\mu}_L^+\tilde{\mu}_L^-$ pairs are reduced in around 90%. Besides the relative statistical error is enhanced in 5%, we finally see that a purity of 42% have been gained. In bottom panel of Fig. 7.9 the P_T distributions indicate an interesting point of confluence just around 60 GeV. It is clear that most of the background events with a P_T less than 60 GeV are rejected (cut 3). It is quite similar to the one shown in top panel of Fig. 7.7. Nonetheless, the implementation of P_T cut has also served as to reduce drastically those events which are constituted by the muons produced by the $\tilde{\chi}_2^0$ (7.17) and what are featured by a lower P_T. Finally 2831 signal events remains against to the 9063 of background. Again is found that the background is thus dominated by the Ws processes. The remaining events are plotted in Fig. 7.10. From this analysis a signal efficiency of 33.5% and a purity of 23.8% with a relative statistical error of 3.85% was gained. To estimate the relative statistical error of $\mathrm{Br}(\tilde{\mu}_L \to \tilde{\chi}_2^0\mu)$

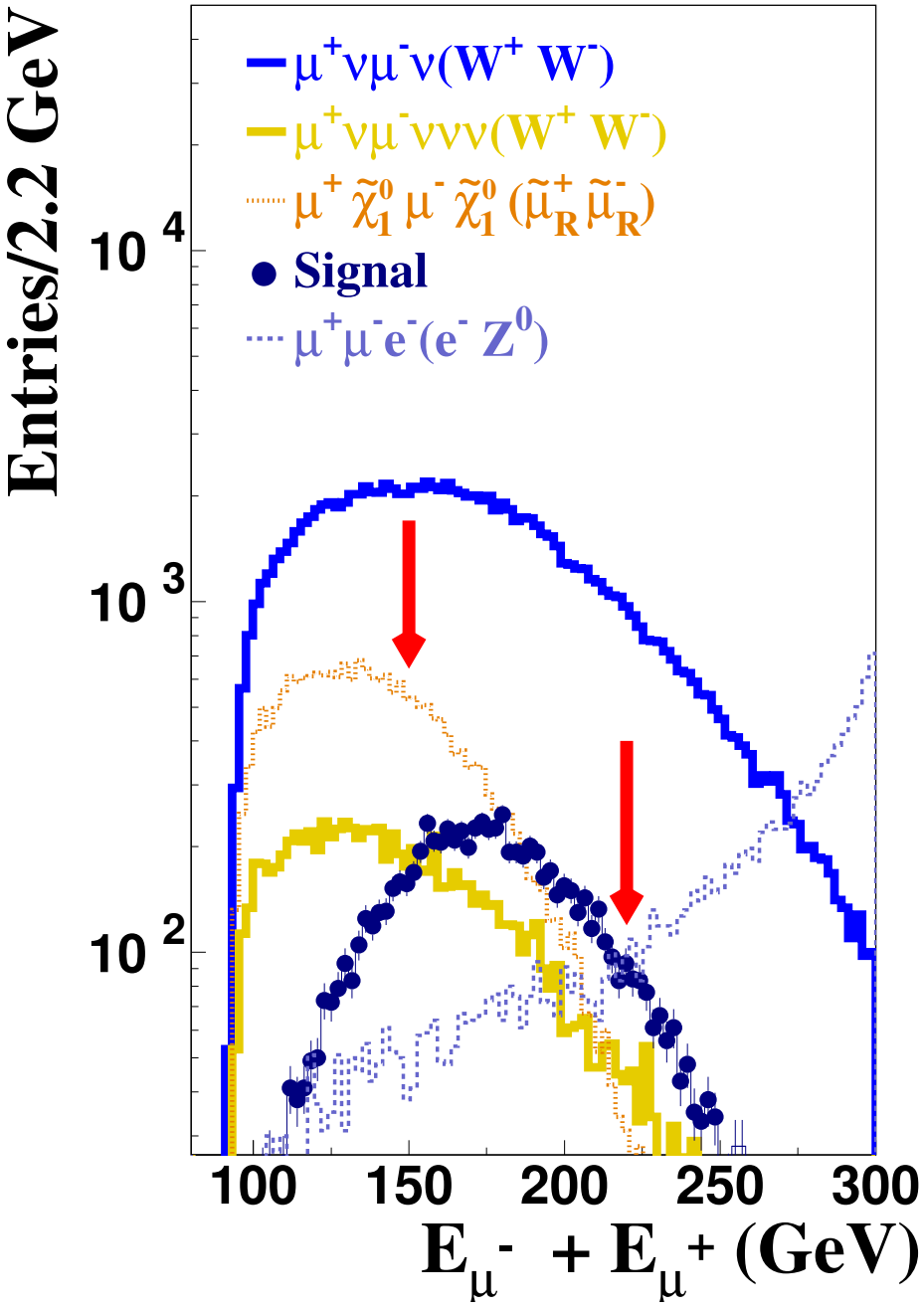

Figure 7.8: Plot of muon energy spectrum of signal (with error bars) and its background. The arrows show the position of the applied cuts.

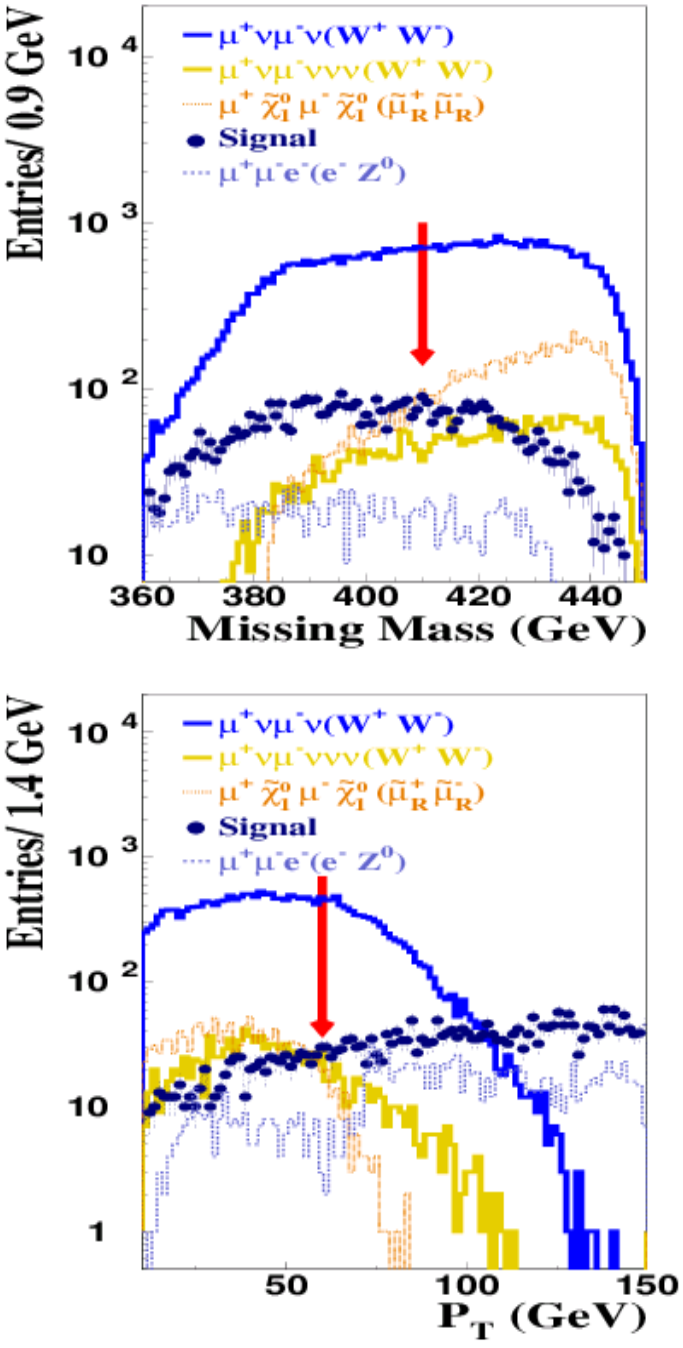

Figure 7.9: (Top) The missing mass distribution of signal (with error bars) and background. The arrow indicate the position of the cut applied. (Bottom) The P_T distributions and the position of applied cut.

we start with the relation

$$2 \cdot \mathcal{L} \cdot \sigma_{eff} \cdot \mathrm{B}r(\tilde{\mu}_L \to \mu\tilde{\chi}_1^0) \cdot \mathrm{B}r(\tilde{\mu}_L \to \mu\tilde{\chi}_2^0) = N_{2s}\frac{\mathrm{p}}{\epsilon}, \tag{7.20}$$

where the relative error can be obtained in a straightforward way as follows

$$\begin{aligned}\frac{\Delta \mathrm{B}r(\tilde{\mu}_L \to \mu\tilde{\chi}_2^0)}{\mathrm{B}r(\tilde{\mu}_L \to \mu\tilde{\chi}_2^0)} = & \sqrt{\left(\frac{\Delta N_{2s}}{N_{2s}}\right)^2 + \left(\frac{\Delta \mathrm{B}r(\tilde{\mu}_L \to \mu\tilde{\chi}_1^0)}{\mathrm{B}r(\tilde{\mu}_L \to \mu\tilde{\chi}_1^0)}\right)^2} \\ & = \sqrt{\left(\frac{\Delta N_{2s}}{N_{2s}}\right)^2 + \frac{1}{4}\left(\frac{\Delta N_{1s}}{N_{1s}}\right)^2} = 3.97\%, \end{aligned} \tag{7.21}$$

where N_{1s} had been used in virtue of (7.20). For the case where the quantity $\Delta N_{1s}/N_{1s}$ is smaller than 1%, one expects that (7.21) depends uniquely on $\Delta N_{2s}/N_{2s}$. In Fig. 7.10 can be viewed that there exist a notable difference between the remaining signal histogram and the one obtained for the $\tilde{\mu}_L \to \mu\tilde{\chi}_1^0$ decays. In other words, the signal is indistinguishable because the background events from Ws. Although the achieved statistics is good enough, the result indicates us the lack of evidence of SUSY events for energies beyond 175 GeV. Above this energy, the signal distribution is even underneathed by noise and therefore an evidence of SUSY events cannot be claimed.

7.4 Systematics Uncertainties

The most important sources of systematics for the previous "measurements" are: The $\gamma\gamma$ luminosity, helicity deviations, background effective cross sections, signal effective cross section and low energy muons.

- Luminosity: The luminosity does not transform linearly into the branching ratio errors. Therefore, for a luminosity error of 1% it was found a systematics error of 0.1% for the channel (7.8), whereas for the channel (7.9) a systematics of 4% is expected.

- Helicity deviations: For the calculation of the systematics, we have used SHERPA which allow us to manipulate the input parameters in the conversion point. For fluctuations of order of 1% the resulting systematics is of order of 0.5% for (7.8) and (7.9) channels.

- Background effective cross sections: Changes on this quantity affect the branching ratio measurements of (7.8) and (7.9) channels. For (7.8) we have found that the branching ratio is affected in 0.5% whereas for

(7.9) the influence is notable: of up to 12%. It is clear because the dominance of the background over the signal.

- Low energy muons: They affects substantially the measure of $\tilde{\mu}_L \to \mu\tilde{\chi}_2^0$. It is because the low energy region down to 20 GeV is contamined by muons produced by another smuon decay: $\tilde{\mu}_L \to \nu\tilde{\chi}_1^{\pm}$. We have calculated the corresponding systematics as follows: We have redo the analysis by simulating solely the channel (7.8) and we have apply the same cut procedure. We have found that the relative statistical error suffers a change of up to 25% (depending upon cuts).

In conclusion, we can state that the $\tilde{\mu}_L \to \mu\tilde{\chi}_2^0$ decays are quite sensitive to systematics because the presence of a large number of background events and low energy muons derived from other channels.

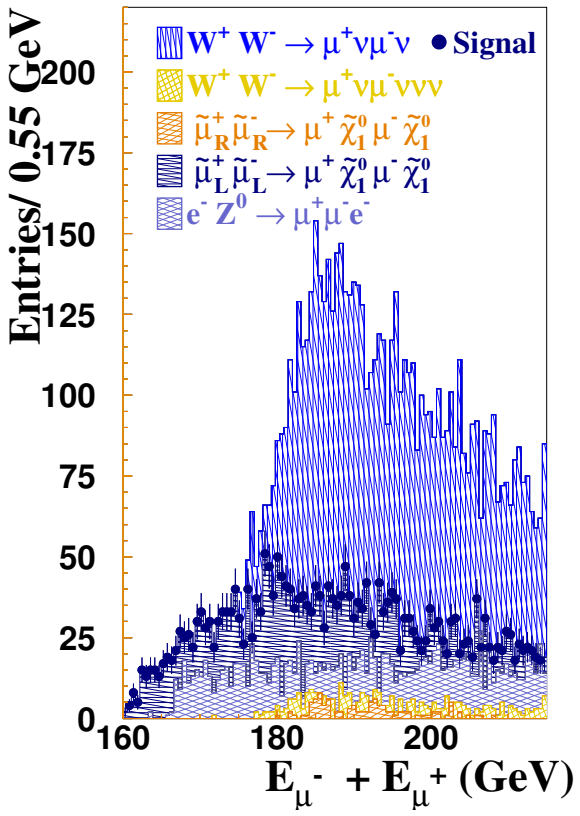

Figure 7.10: The energy distribution for signal (with error bars) and the remaining background is plotted.

7.5 Interpretation of the Results

To judge the obtained results in previous sections, we shall apply a technique developed in Ref. [B$^+$05a] aimed to fit SM parameters together with the expected measurements from LHC-ILC in order to extract some SUSY parameters and their uncertainties. Concretely, the interest here in to observe whether the branching ratio uncertainties obtained in the photon collider would serve for an improvement on the determination of errors of the SUSY parameters. A similar procedure was performed in the past [KM05] for the case of charginos. Two points shall be clarified, the tool responsible for fitting and the inputs. Later we will describe the procedure.

7.5.1 Tools

We will use the FITTINO [B$^+$05a] as the central code to be used in this section. FITTINO performs a fit by using the precision of future mass measurements of superpartners at the LHC and polarized topological cross-section measurements at ILC. Higher order radiative corrections are also accounted in FITINO. The code uses the Simulated Annealing Algorithm to determine the SUSY parameters by using one loop corrections to observables and couplings. FITINO does not needs an anticipated knowledge of the parameters. Instead it provides the reconstruction of SUSY lagrangian by means the measured observables what play the role of inputs for the fitting. SPheno [Por03] is employed as a calculator of supersymetric spectra. It should be noted that FITTINO uses the spectrum calculated by SPheno which is not in agreement with the one of ISAJET. Numerically, SPheno and ISAJET have a discrepancy of order of 2% [A$^+$02] what is acceptable to some extent.

7.5.2 The SM and SUSY Inputs

To continuation the input parameters as well as a few observables are listed. The SM parameters are of importance for the fitting. The are listed below,

- $\alpha_s = 0.1172 \pm 0.0002$,
- $G_F = 1.16630{\cdot}10^{-5} \pm 1{\cdot}10^{-11}$,
- $\alpha_{em} = (127.934 \pm 0.027)^{-1}$,
- $\sin 2\theta_W = 0.23113 \pm 0.00015$,

Aside from this, the $e^+e^- \to Z^0 h_0$ processes for $\sqrt{s}_{e^+e^-} = 0.4$ TeV and 0.5 TeV are considered,

- $\sigma(\sqrt{s}_{e^+e^-}$ =0.5 TeV, -0.8,-0.6) = 13.7432 ± 0.23 (fb),
- $\sigma(\sqrt{s}_{e^+e^-}$ =0.5 TeV, 0.8, 0.6) = 11.6626 ± 0.21 (fb),
- $\sigma(\sqrt{s}_{e^+e^-}$ =0.5 TeV, -0.8, 0.6) = 43.4364 ± 0.43 (fb),
- $\sigma(\sqrt{s}_{e^+e^-}$ =0.5 TeV, 0.8,-0.6) = 28.8723 ± 0.33 (fb),
- $\sigma(\sqrt{s}_{e^+e^-}$ =0.4 TeV, -0.8, 0.6) = 69.9194 ± 0.69 (fb),
- $\sigma(\sqrt{s}_{e^+e^-}$ =0.4 TeV, 0.8,-0.6) = 46.4757 ± 0.45 (fb).

These cross sections have been computed by SPheno [Por03]. It should be noted that the polarization states of the lepton beams are properly exploited. When the photon collider is running for energies $\sqrt{s}_{e^+e^-}$=0.6 TeV, cross section measurements involving the lightest Higgs boson are already known. In addition, masses of supersymmetric as well as SM particles are required. We have assigned an uncertainty because of their theoretical and experimental predictions in some cases, In Table 7.4 additional observables to be used in

Obs.	**Mass(GeV)**	δ**M**	**Obs.**	**Mass(GeV)**	δ**M**
m_Z	91.1187	0.0021	M_W	80.3382	0.039
m_c	1.2	0.2	m_b	4.2	0.5
m_t	174.3	0.3	m_τ	1.77	0.00029
m_{h_0}	110.2	0.502	m_{A_0}	399.76	1.3
m_{H_0}	400	1.3	m_{H^+}	407.695	1.1
$m_{\tilde{e}_L}$	208	0.2	$m_{\tilde{e}_R}$	143.91	0.05
$m_{\tilde{\nu}_L}$	192.3	0.7	$m_{\tilde{\mu}_L}$	208.01	0.5
$m_{\tilde{\mu}_R}$	143.8	0.11	$m_{\tilde{\tau}_1}$	134.28	0.3
$m_{\tilde{\tau}_2}$	211.79	1.1	m_g	630.449	6.4
$m_{\tilde{\chi}_1^0}$	95.74	0.05	$m_{\tilde{\chi}_2^0}$	182.39	0.08
$m_{\tilde{\chi}_1^+}$	180.46	0.55	$m_{\tilde{\chi}_2^+}$	379.96	3.0

Table 7.4: Spectrum of masses by assuming the SPS1a scenario as part of the input used for the fit.

the fit [G.04a] are listed. In Higgs sector $h_0 = 110.2\pm$ 0.5 GeV to be provided by the ILC, is expected. Measurements of heavy Higgs bosons are expected at LHC, resulting their precision in up to 2.5 times bigger than h_0. Some SUSY observables have been considered. For instance, the error on the right-handed selectron mass is assumed to be one per mile. For the gluino mass an uncertainty of 1% has been corresponded. The neutralinos $\tilde{\chi}_1^0$ and $\tilde{\chi}_2^0$ and charginos $\tilde{\chi}_1^+$ and $\tilde{\chi}_2^+$, have been also inserted in our list of input paramteres

discarding heavier gauginos whose mass resolution would be highly speculative. For the sake of the simplicity, the squark sector is fixed because it has not influence over the slepton and chargino sectors,

- $M_3 = 588$, X_t = -506, X_b = -4441,
- $M_{\tilde{s}_R} = M_{\tilde{d}_R} = 528$, $M_{\tilde{u}_R} = M_{\tilde{c}_R} = 530$, $M_{\tilde{u}_L} = M_{\tilde{c}_L} = 548$,
- $M_{\tilde{b}_R} = 524$, $M_{\tilde{t}_R} = 424$, $M_{\tilde{t}_L} = 499$,
- $m_t = 174.3$, $m_b = 4.2$, $m_c = 1.2$,

where X_t and X_b are the top and bottom mixing parameters at the MSSM model. These quantities have been obtained from SPheno. Because it is impossible to achieve a fit of 124 parameters, we will choose only 27 parameters for the fitting procedure. Only 15 of them, the parameters belonging to the squark (quark) sector are fixed, whereas 12 parameters corresponding to the Higgs and sleptons sectors are accepted for the analysis.

7.5.3 A Two Step Procedure

The two step procedure is necessary because we want to know the impact of the branching ratio measurements in a global fit.

In order to carry out the fit, the following procedure is used: Firstly, to carry out a fit without any information of the photon collider measurements, and secondly, redo the fit with the branching ratio errors. This procedure was successfully applied in the past for chargino studies [KM05]. For our analysis, an upgrade version of FITTINO has been used [B$^+$06].

Smearing of Observables

To start the analysis with FITINO, the tree-level estimates of the parameters according to the relation obtained in [B$^+$05b] are needed. It is solved by SPheno and once they are established, all of them enter to the statistical analysis until their χ^2 are globally minimized. The latest uses the Simulated Annealing Algorithm until a successful convergence have been reached. Then, the observables Λ_i^q are randomly smeared between Λ_i^q - δ_i^q and Λ_i^q + δ_i^q. The lenght $2\delta_i^q$ is obtained by using a normalized Gaussian probability density. The lower index i denotes the input value whereas the upper index q the ensemble. It serves to perform 1000 individual fits what actually can be interpretated as independent experiments. This operation have been used for the cases without and with branching ratio errors information (of left handed scalar muon). A few tens of fits were discarded because of their unphysical

meaning. After of cleaning the sample of inconsistencies, we have observed that the distributions agree well with Gaussian-like functions. We have also noted that the shape of them are quite sensitive to the binning. This fact forces us to incorporate a systematic error when a fit on the Gaussian-like distributions are performed.

Fitting the Fits

After of storing the information provided by the individual fits, we have filled the corresponding histograms for the fitted parameters. At first glance, the histograms are characterized by a Gaussian-like shape. In all cases, the central value coincides with the tree level prediction. On these histograms, we have performed a last fit. The shape of the distributions demand us to use Gaussian functions. These functions are described by three parameters: P1 the central value, P2 the height and P3 the uncertainty or σ. Since these functions are adjustable to the histograms, in all cases a reasonable χ^2 was obtained. The final results are shown in Fig. 7.11 where the whole procedure has yielded an improvement for the uncertainty of tanβ in about 4.5% "when the information of the measurements of left-handed smuon branching ratio have been included" (in the following, left and right panels display the fit with and without the uncertainties of $\tilde{\mu}_L \to \mu\tilde{\chi}^0_{1,2}$ decays, respectively). On top panels of Fig. 7.12 are plotted the corresponding results for the μ parameter. In this case, the parameter P3 was reduced by a 2.1%. For the M_1 parameter, on the bottom panels of Fig. 7.12 one can observe that an improvement of up to 4.7% can be gained. Concerning the remaining SUSY parameters, all of them were almost unaffected by emphasizing the poor impact of the achieved precision (of the branching ratio measurements) on some MSSM parameters.

Systematic Errors

The fitted values shown in Fig. 7.11 and Fig. 7.12 are not absolute in the sense that the number of entries produces a variation on the uncertainties of the fitted parameters. Therefore, exist there a dependence of the binning which in reality a kind of systematics. Thus, we have monitored the uncertainties by varying the number of entries or individual fits from 100 up to 800 in order to measure the variation on P3 and its respective uncertainty. We have observed a variation at the level of less than 1% which is actually negligible. Note that this variation have been compared to a referential value given by the results when 800 individual fits are used. Table 7.5 summarizes the results achieved.

Parameter (SPS1a)	Statistic (without)	Statistic (with)	Systematic
$\tan\beta$	0.18	0.1711	0.003
μ	0.3602	0.3528	0.007
M_1	0.0266	0.02537	0.001

Table 7.5: The absolute uncertainties from the fit results for MSSM for the cases with and without errors of the Br obtained in previous sections. Systematics uncertainties have been attained due to a slight dependence of the fit on the binning.

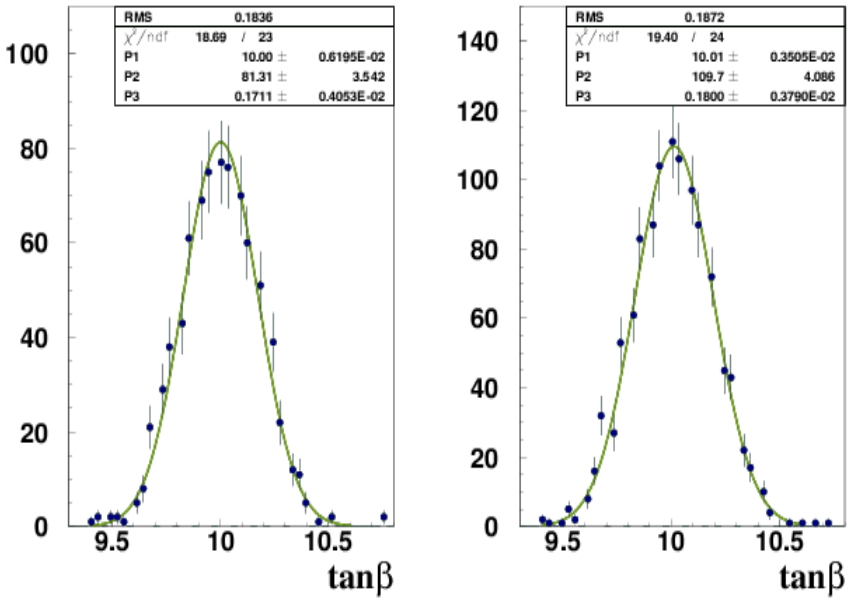

Figure 7.11: Left and right panels display the fit on the histograms for the case with and without additional information from the photon collider.

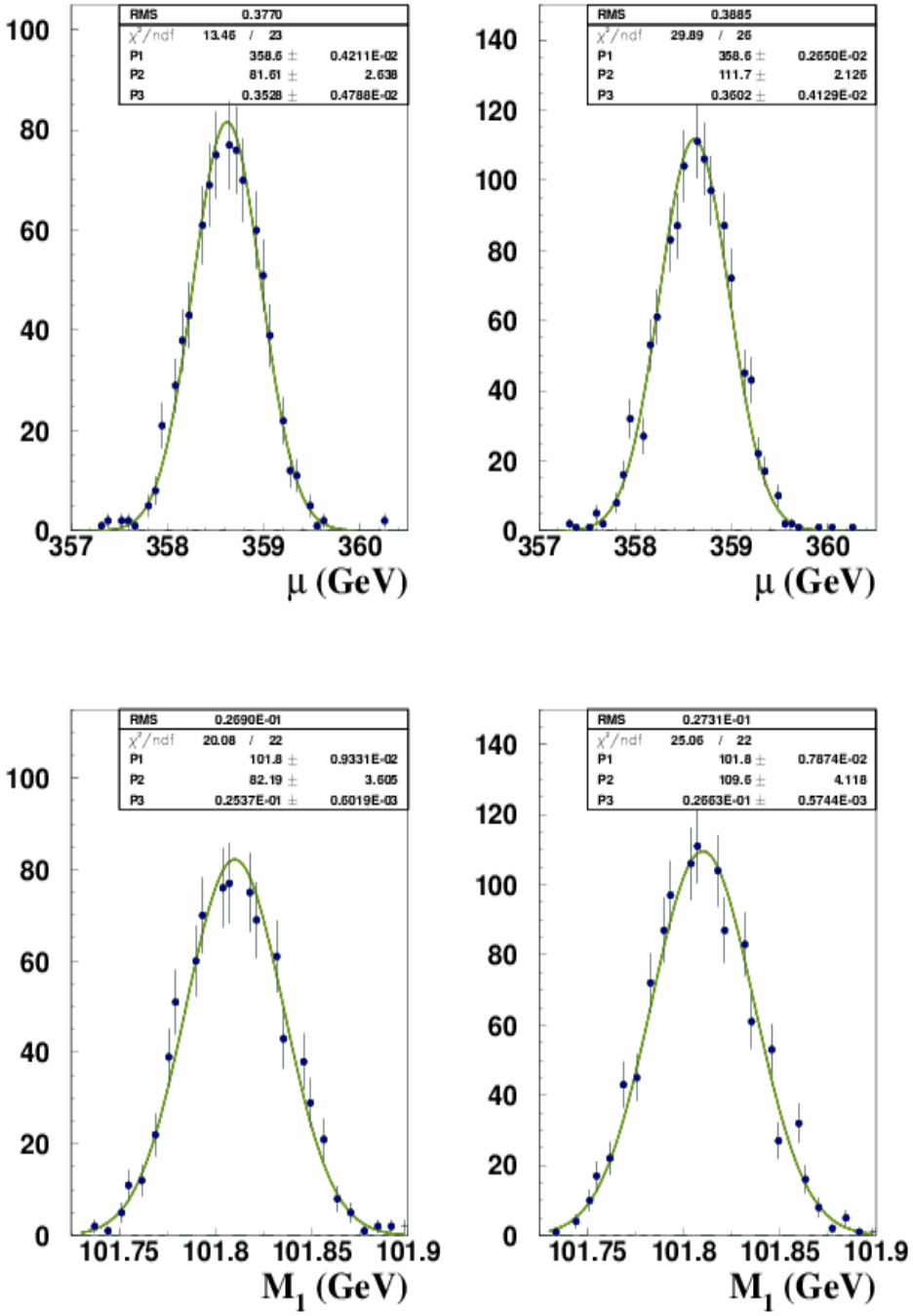

Figure 7.12: In top and bottom panels are displayed the curves that adjusts the histograms for the case without (left) and with (right) the obtained uncertainties from the photon collider.

Chapter 8

Study of Heavy Neutralinos Production at the Photon Collider

8.1 Arguments to Study Heavy Neutralinos in Photon Collisions

The why of studying $\tilde{\chi}_2^0$ production in the photon collider comes from the following reasons:

- For mSUGRA models like SPS1a, the effective cross section for left-handed smuon production is about 30 fb.
- The $\tilde{\mu}_L \to \mu\tilde{\chi}_2^0$ decays give rise to the final states containig several final state leptons because $\tilde{\chi}_2^0 \to \tilde{\chi}_1^0\ell^+\ell^-$.
- The production of the SUSY $e^+e^-e^+E^{miss}$, $\mu^+\mu^-e^+e^-E^{miss}$ and $\mu^+\mu^-\mu^+\mu^-E^{miss}$ events might be of order of several hundreds per year.
- The absent of dangeorus SM background processes containing several final state leptons might be an advantage to isolate the SUSY events.
- A measure of SUSY mass differences on the M(ℓ^+,ℓ^-) spectrum might be possible.

These arguments serve to justify a subsequent study of $\tilde{\chi}_2^0$ production in photon collisions. Actually, valuable information about the kinematics of the $\tilde{\chi}_2^0$ decays can be obtained. In the following we shall see how the kinematics of decay of this heavy neutralino lead to origin interesting final states.

8.2 SUSY Reactions at the Electron-Gamma Collider

In the past a special attention was paid in the investigation of the $e^-\gamma \to \tilde{e}_{R,L}\tilde{\chi}^0_{1,2}$ $(2 \to 2)$ reactions in which the mass splitting between gauginos and sleptons is to a large extent arbitrary [B$^+$97][Cho95]. These studies have motivated to carry out Monte Carlo studies guided by the possibility of extracting the signal from a few SM background processes. A first "experimental" treatment have emphasized an alternative method to measure the selectron mas These investigations have focused on the production and detection of the

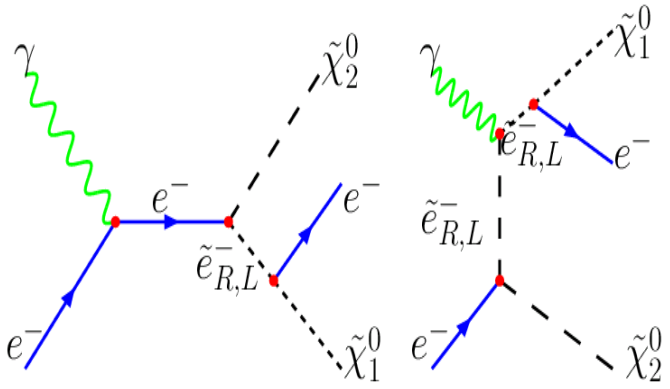

Figure 8.1: The Feynman graphs for the 2→3 reactions at the $e^-\gamma$ collider.

$e^-\gamma \to \tilde{e}^-_R\tilde{\chi}^0_1$ reactions followed by the $\tilde{e}^-_R \to \tilde{\chi}^0_1 e^-$ decay aimed to measure the right-handed selectron mass, having reached a statistical uncertainty of 0.3% [M$^+$06]. In this section, we shall discuss the prospects of identifying the $e^-\gamma \to \tilde{e}^-_L\tilde{\chi}^0_2$ reactions, and therefore to have access to an alternative way for measuring the mass difference $m_{\tilde{\chi}^0_2}$ - $m_{\tilde{\chi}^0_1}$. Even though these states are responsible to generate the 3-leptons and missing energy states and it would allow us again to extract the kinematics of $\tilde{\chi}^0_2$ decay. One should observe that the $e^-\gamma \to \tilde{e}^-_L\tilde{\chi}^0_2$ reactions can be best studied under the assumption of the SPS1a' [AS$^+$05] scenario because the $\tilde{e}^-_L$ scalar decays into electron-light neutralino in a 90%. Selectron production in γe^- collisions offers a certain complexity because of its s- and t-channel contributions to the matrix elements as it is shown in Fig. 8.1. To be specific, since the $\tilde{\chi}^0_2$ is involved $e^-\gamma \to \tilde{e}^-_L\tilde{\chi}^0_2$ reactions, it undergoes cascade as $\tilde{\chi}^0_2 \to \tilde{\ell}_{L,R}\ell$ with $\tilde{\ell} \to \ell\tilde{\chi}^0_1$ resulting in the following final states: $e^-\mu^+\mu^-\tilde{\chi}^0_1\tilde{\chi}^0_1$ or $e^-e^+e^-\tilde{\chi}^0_1\tilde{\chi}^0_1$. In this part, we concentrate on the latest in which these states are expected to be successfully reconstructed in the ECAL.

8.2.1 The 2 -> 3 Particles Reactions

The computation of 5 particles final states have been splitted in two parts. Monte Carlo simulation of the 2→3 reactions is possible with SHERPA which includes the massive propagators $\tilde{e}_{R,L}$. Technically speaking, once the $e^-\gamma \to e^-\tilde{\chi}_2^0\tilde{\chi}_1^0$ reactions had been written by SHERPA, we proceeded to generate the final states $e^-e^+e^-\tilde{\chi}_1^0\tilde{\chi}_1^0$ events by using the package PYTHIA interfaced with ISAJET. In other words, we allow the decaying of $\tilde{\chi}_2^0$ in according to the mSUGRA model. This exercise demand us to insert the mass values obtained from SPheno [Por03], an alternative generator of SUSY spectra that invokes one-loop corrections already used in previous chapter. It is

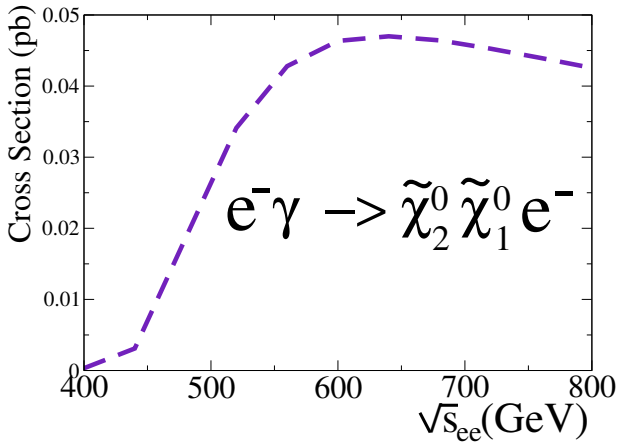

Figure 8.2: The effective cross section in function of center-of-mass energy in the e^-e^- system.

important to note the direct generation of the 2→3 reactions as depicted in Fig. 8.1, permit us to take into account s- and t-channel interferences which would be neglected as for the case of production of simple 2→2 production. We have assumed a polarized electron beam of 80% and J = -1 for the $e^-\gamma$ system. The photon spectrum is taken from CompAZ and nonlinear effects are included mandatorily. Besides same input parameters already used are taken for the present case, a luminosity of 2/3 e^+e^- is considered for the $e^-\gamma$ machine as proposed in its technical design. In this way, a luminosity of $\approx$ 1100 fb^{-1} at the $e^-\gamma$ mode when only one laser beam is switched on is assumed. Fig. 8.2 displays the effective cross section for the $e^-\gamma \to e^-\tilde{\chi}_1^0\tilde{\chi}_2^0$ reactions (2→3) having its maximum around $\sqrt{s}_{e^-e^-} = 0.6$ TeV. It is actually bigger than the $\gamma\gamma \to \tilde{e}_L^-\tilde{e}_L^+$ reactions by a factor 1.5 for the same center-of-mass energy. In these studies a $\sqrt{s}_{e^-e^-} = 0.5$ TeV is assumed because the background statistics is smaller than the signal. According to Fig. 8.2, 17200

$e^-\gamma \to e^-\tilde{\chi}_1^0\tilde{\chi}_2^0$ events can be produced at $\sqrt{s}_{e^-e^-} = 0.5$ TeV. Concretely, the number of signal events is derived by taking into account a Br($\tilde{\chi}_2^0 \to \tilde{e}_R^{\pm}e^{\mp}$) = 0.0119, and

$$\mathcal{L} \cdot \sigma \cdot 2 \cdot \mathrm{B}r(\tilde{\chi}_2^0 \to \tilde{e}_R^{\pm}e^{\mp}) = 1100(\mathrm{f}b^{-1}) \cdot 26(\mathrm{f}b) \cdot 2 \cdot 0.0119 \approx 680$$

Then 680 $e^-e^+e^-\tilde{\chi}_1^0\tilde{\chi}_1^0$ events were generated and all of them shall be processed by SIMDET.

8.2.2 Analysis at the Detector Level

The denomination of "primary" electron is herein adjudicated to the one whose source is that of the left-handed selectron, whereas the "secondary" electron is the one produced by the $\tilde{\chi}_2^0$. Actually, the angular distributions are crucial to deduce the origin of lepton. To observe the tracks of detected leptons, a dedicated simulation supported by GEANT [Gia00] and BRAHMS [Beh01b] was performed. These codes offer the possibility of a full reconstruction of individual events, including the reconstruction of tracking and energy deposition in comparison to the fast simulator SIMDET. In top panels of Fig. 8.3 is observed that the direction of electron produced by the left-handed selectron stands roughly opposite to that of the electron-positron pair derived from the $\tilde{\chi}_2^0$ decay.

SM backgrounds were simulated with the assistance of AMEGIC. The signal does not present SUSY backgrounds. The relevant SM processes which become a dangerous noise are $e^-\gamma \to e^+e^-e^+$ (σ=132 fb) and $e^-\gamma \to e^+e^-e^+\nu\nu$ (σ=5 fb). Another SM noise are the $e^-\gamma \to e^-\tau^-\tau^+$ processes, with the τs decaying into $e^{\pm}\nu\bar{\nu}$, but they were neglected because of the small total transverse momentum of the $e^{\pm}$. We have also found as to include pile-up events in the analysis, does not degrade the shape of the energy distributions on the detected leptons. Once the full kinematics is taped, a confrontation between signal and its noise is needed. Their differences are explicitly manifested in Fig. 8.4 where have been plotted the histograms corresponding to the e^+, e^-, and e^+ particles. One can see there the $e^-\gamma \to e^+e^-e^+$ processes become the dominant one for all individual registered leptons. It can be seen the expected differences between the spectra for the e^- and e^+ produced by the $\tilde{\chi}_2^0$ (top panels) and the one originated from the $\tilde{e}_L$ decay whose shape is immediately associated to the left-handed smuon analyzed early. Although its energy distribution differs in somewhat with that of SPS1a, one can distinguish the two-peaked characteristic even when selectron decays almost entirely into electron and neutralino. In bottom right panel, the reconstructed invariant mass made by a e^+e^- pair emanated from $\tilde{\chi}_2^0$ indicate us the presence of a

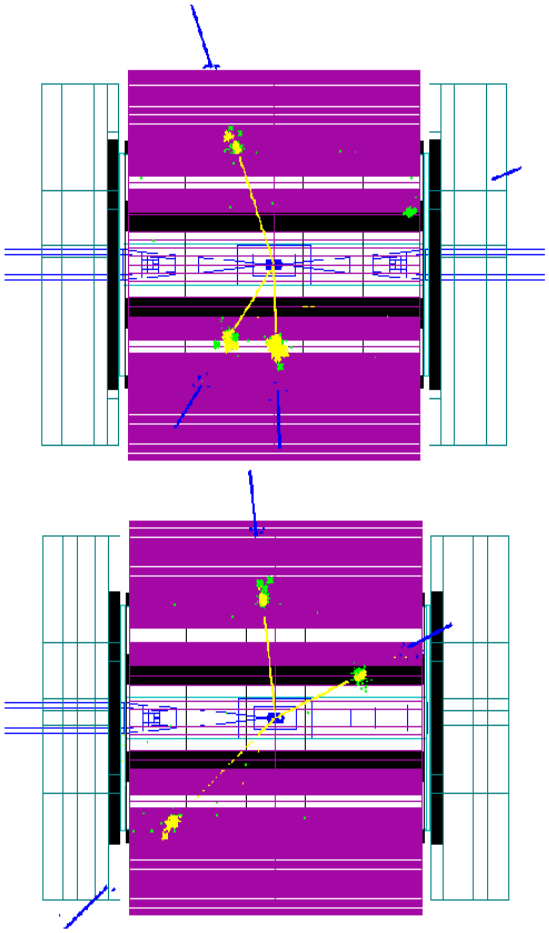

Figure 8.3: Reconstructed trajectories of $e^+e^-e^-$ at the planed ILC detector with the package BRAHMS based on GEANT.

hard edge closely to the Z^0 mass. Also it is noted the strong contamination just over the zone of edge is in essence caused by the efficient reconstruction of the Z^0 mass of background distributions. It constitutes a serious obstacle for a clean measurement of edge on the signal invariant mass distribution.

8.2.3 Preselection and Selection

Essentially, the cuts should be capable to defeat a sizeable amount of noise along the region where the edge is situated. After of processing 680 signal events through SIMDET a little percent of them (0.5%) are lost over the very forward zones. In some cases, the detected leptons were accompanied of low energy photons as result of "switch on" the final state radiation in

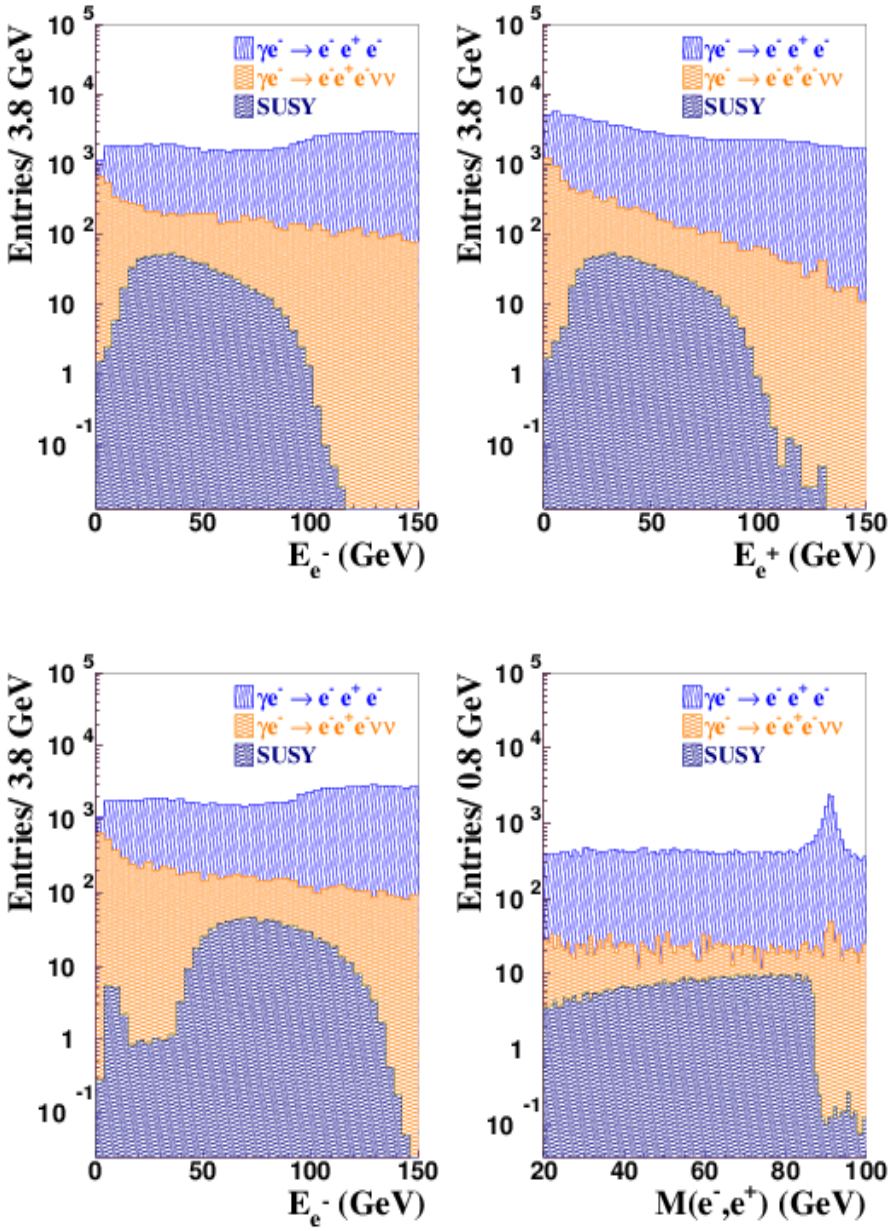

Figure 8.4: Reconstructed energy distribution after preselection. On bottom right panel, the invariant mass of "two-sided" e^+e^- is plotted. To note the Z^0 mass reconstruction overwhelming the endpoint of signal. Top panels show the distributions of the leptons produced by $\tilde{\chi}_2^0$ whereas in the bottom panel (left side) the one produced by the $\tilde{e}_L^-$. In the right side panel the invariant mass is plotted (both leptons come from $\tilde{\chi}_2^0$).

Cut	Efficiency(%)	Purity(%)	$\Delta N_s/N_s$(%)
	100	0.48	55.35
$P_{Miss}(3\ell)$ <90 GeV	50.74	0.79	60.56
$P_T(3\ell) > 5$ GeV	50.59	7.18	20.12
20 GeV $< E_1 <$100 GeV	45.15	16.00	14.45
50 GeV $< E_2 <$130 GeV	39.41	29.98	11.16
20 GeV $< E_3 <$75 GeV	33.97	48.73	9.42
60 GeV $< E_1 + E_3 <$120 GeV	32.35	56.56	8.97
110 GeV $< E_{3\ell} <$ 210 GeV	30.44	57.02	9.20
$M(e^+, e_s^-) <$ 88.5 GeV	**30.15**	**62.70**	**8.82**

Table 8.1: Cut-flow of signal showing the effect of applied cuts on both efficiency and purity. The upper index 1,2 and 3 denote the positron, "primary" and "secondary" electron, respectively.

PYTHIA. For the ECAL, the parametric code SIMDET assumes a minimum deposited energy of 0.10 GeV as well as a negligible electron misinterpretation probability.

The preselected candidates are those containing e^+, e^- and e^+ and up to 5 photons. In addition, a $P_{T,\ell} > 3.8$ GeV is required to defeat that species produced by the pile-up events, where ℓ denotes to the individual leptons. Throughout the final selection, we have used information acquired from the lepton energy as have been usual in this note. In Table 8.1 the cut variables are listed together with their respective effect on the statistics. We had have to reject noise with a $P_{Miss}(3\ell)$ greater than 90 GeV in conjunction with the requirement in accepting those events with a total transversal momentum greater than 5 GeV, having gained an signal purity of 7.18%. This happens because the noise is constituted by leptons with a higher longitudinal momentum in comparison to signal whose total momentum in average is dominated by the transversal component. As consequence, the signal purity reaches a 7.18%. Indeed, cuts on the energy spectra of individual leptons are required in virtue of their peculiar shape against backgrounds. In consequence the usage of lepton energy have led us to gain a purity of a 57%. However it is desirable to get a clean invariant mass distribution as stated early. Then this neccesity is translated in the application of a further cut and thus we have defined the cut variable M(e^+, e_s^-) which uses information of electron derived from the selectron decay instead the M(e^+, e^-) where both leptons come from $\tilde{\chi}_2^0$ decay. Finally, we require a M(e^+, e_s^-) less than 88.5 GeV, yielding a signal purity of 62.70%. We arrived to a reasonable discrimination manifested in the statistics given in Table 8.1, showing a signal efficiency of 30.15% and

a relative statistical error of 8.82%. So that 182 $e^+e^-e^+\nu\nu$ events of the major background still prevails agains to the 205 events of signal. Note that preselection and selection have omitted to use any information linked to the superpartner masses. In general, an independent model strategy for searching new physics signatures might be simplified in the relation $P_T(e^-, e^+, e^-)$ $< h(E_e^-, E_e^+, E_e^-) < \sqrt{s}_{e^-,e^-}$, being h a linear function which depends on the individual energies of the detected leptons.

8.2.4 Edge Measurement

Having reached a substantial purity of order of 62.70%, we turn to plot M(e^+, e^-) from the taped information of momentum-energy of "one - sided" electron-positron.

For further steps, we have added to the signal histogram the ones of the remaining background histograms.

Various histograms for different binning have shown a hard edge just over the region where it is expected the information of the mass difference between $\tilde{\chi}_2^0$ and $\tilde{\chi}_1^0$. Three of them are displayed in Fig. 8.5 and one can see on it an hard edge, fact what motivate us to apply a fit on that. To perform the fit, the step-function $M_{ll}(E)$ as defined,

$$M_{ll}(E) = \frac{p_1}{\pi}(1 - p_4(p_3 - E))(\frac{\pi}{2} - tan^{-1}(p_3 - E)), \tag{8.1}$$

where the parameters p_1, p_2 and p_4 denote the high, width and slope of the function respectively, while p_3 returns information of edge. The fitting was performed for different binning. In the top panel of Fig. 8.5, the fitting gave 86.16 GeV ± 0.59 GeV, whereas the bottom panel shows the best fit where the identification of the edge was quite precise being the fitted values quite close to the prediction of SPheno yielding 86.35 GeV ± 0.42 GeV. Under the SPS1a' scenario, the SPheno prediction is about 86.3 GeV. Upon varying out the binning these Lorentz invariants M(e^+e^-) are affected by systematics. It is manifested in a small variation of the fitted values when a change of binning is applied. After of taking the average of all fitted results, a systematic of 0.3 GeV by effect of binning was found. Hence, the present Monte Carlo study yields the following estimate: $m_{\tilde{\chi}_2^0}$ - $m_{\tilde{\chi}_1^0}$ = 86.4 GeV ± 0.4 GeV (stat) ± 0.3 GeV (syst), for the SPS1a' scenario with a spectrum mass provided by SPheno.

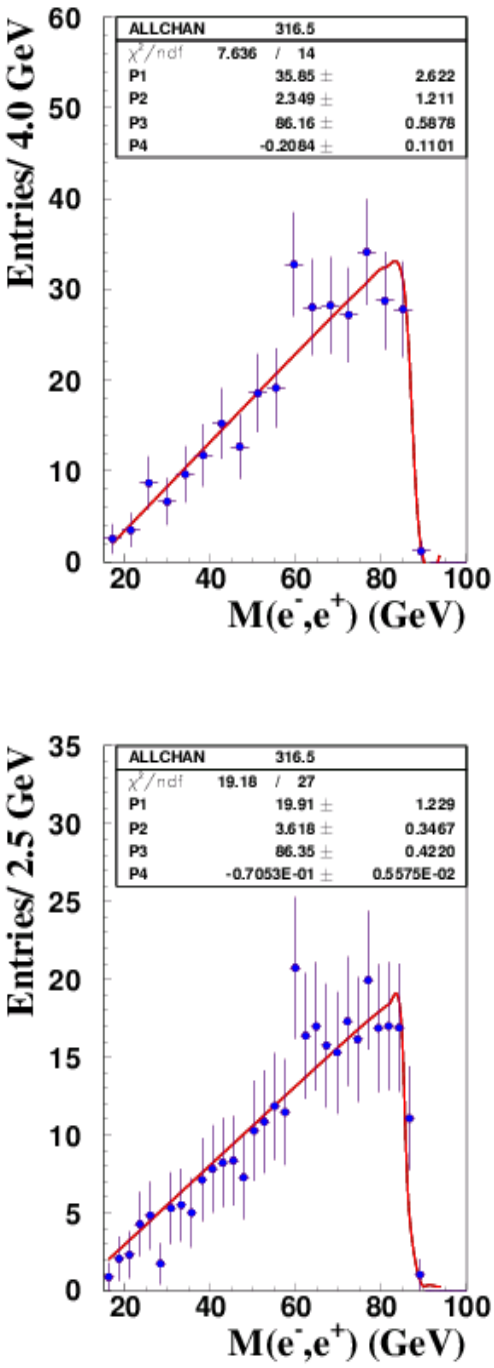

Figure 8.5: Mass difference measurement for different binning.

8.3 Study of the 4-Lepton and Missing Energy Final States at the Photon Collider

8.3.1 Cascade Decays From Left-Handed Smuon Decay

The previous studies has led to have a better comprehension of what SUSY observables can be identified and measured in a photon collider. In this section we shall address the SUSY multiple events identification issue, extensively. The possibility to recognize the SUSY final states containing more than 2 muons born out of the conjecture that these topologies might a priori be easily detected because of the lack of dangerous background processes.

As already seen, under the assumption of the SPS1a model the left-handed scalar muon mass and effective cross section are 204 GeV and 30 fb, respectively. Therefore, the rate of production is sufficient for exploring the cascade decays as depicted below,

$$\begin{aligned} \gamma\gamma \rightarrow \qquad & \tilde{\ell}_L^+\tilde{\ell}_L^- \rightarrow \ell_i^+(\tilde{\chi}_2^0)\ell_i^-\,\tilde{\chi}_1^0 \\ & \qquad\qquad\qquad\quad \searrow \\ & \qquad\qquad\quad (\tilde{\ell}_R^{\mp})\ell_j^{\pm,a} \\ & \qquad\qquad\qquad\quad \searrow \\ & \qquad\qquad\qquad\quad \tilde{\chi}_1^0\ell_j^{\mp,b} \end{aligned} \tag{8.2}$$

where $\tilde{\ell}_{L,R}$ denotes $\tilde{e}_{L,R}$, $\tilde{\mu}_{L,R}$. Clearly, our interest lies on those events defined as (7.15) with the $\tilde{\chi}_2^0$ decaying into (7.17) or (7.18). Turning now to (8.2) the upper index tags *secondary* leptons, whereas the ones without any label are referred as *primary* leptons. The purpose of this section is to find a strategy to extract the SUSY events defined by the final states containing the $e^+\mu^-\tilde{\chi}_1^0 e^-\mu^+\tilde{\chi}_1^0$ or $\mu^+\mu^-\tilde{\chi}_1^0\mu^-\mu^+\tilde{\chi}_1^0$ final states from SM backgrounds without the use of sophisticated techniques. We have discarded to carry out studies involving the tau leptons for multiple reasons. It is because their hadronic channels cannot be directly distinguished of those created by the pile-up ones at energies down to 10 GeV. Thus spectra made of either e^+e^- or $\mu^+\mu^-$ ought be reconstructed efficiently instead of hadrons or very low energy species. Once the kinematics of detected leptons are reconstructed, we expect to observe edges on the invariant mass distributions namely $\mathrm{M}(\mu^+,\mu^-)$ and $\mathrm{M}(e^+,e^-)$, in virtue of kinematical considerations leading to have a precise knowledge of the mass difference of SUSY particles involved in the decay of left-handed smuon or selectron. To achieve this expectation, we have taken into account alternative SUSY scenarios where the Higgs boson mass

m_h >84.5 GeV and tanβ<5 [Bec03]. Although the present study apparently lacks of arbitrariness, we are inclined to demonstrate that the photon collider also serves as a facility for mass measurement. Thus, for our purposes the SPS1a was slightly varied. We had have to set tanβ=4 in order to increase certain values of branching ratio under discussion. In other words, a sustantial improvement of statisics, most notably due to the variation of tanβ is feasible. The m_0 parameter was kept as the same value used as input to get the SPS1a spectrum. For simplicity this new scenario is called SPS1am. In Fig. 8.6 the product $BR_1 \cdot BR_2 \cdot BR_3$ in function of tanβ is displayed, with $BR_1 = BR(\tilde{\mu}_L \to \mu\tilde{\chi}_1^0)$, $BR_2 = BR(\tilde{\mu}_L \to \mu\tilde{\chi}_2^0)$ and $BR_3 = BR(\tilde{\chi}_2^0 \to \ell\tilde{\ell}_R)$. For tan$\beta$=4, SPS1am turns out to be advantageous in setting a suitable model for testing interesting SUSY 4-leptons final states. We stress the

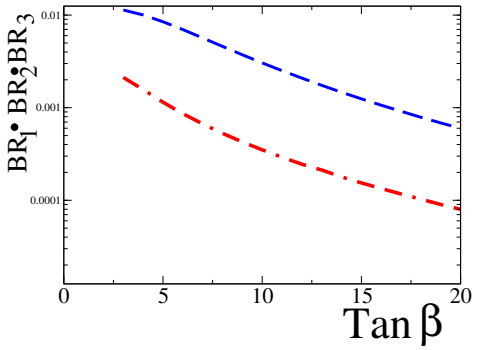

Figure 8.6: Product of branching ratios against tanβ are plotted. Curve containing only dashed lines (in blue) denotes the SPS1am. The one of dashed lines and dots (in red) is made of SPS1a' parameters.

4-leptons States	SPS1a	SPS1a'	SPS1am
$\gamma\gamma \to \mu^+\mu^-\tilde{\chi}_1^0\mu^+\mu^-\tilde{\chi}_1^0$	370	60	1188
$\gamma\gamma \to e^+\mu^-\tilde{\chi}_1^0\mu^+e^-\tilde{\chi}_1^0$	740	120	2376

Table 8.2: Number of events expected for an integrated luminosity $\approx$ one year is listed. Three models are regarded: SPS1a, SPS1a' and an alternative scenario that is established by the change of tanβ=10 $\to$ tanβ=4 inside the SPS1a model.

point by which the photon collider would offer certain advantages for direct identification of the final states given by (8.2) compared to a e^+e^- collider in where a huge amount of background is expected. In concreteness, in Table 8.2 are listed the expected number of events taking into account known models. We have considered the 4-leptons final states manifested in two of their six combinations (tau channel is not considered). The inclusion of

selectrons as source for generating 4-lepton ($e^-e^+\mu^-\mu^+$) events doubles the statistics and it deserves a separated analysis as we will see later. The program for our next steps is that of the identification of the $\mu^+\mu^-\tilde{\chi}_1^0\mu^+\mu^-\tilde{\chi}_1^0$ and $e^+\mu^-\tilde{\chi}_1^0\mu^+e^-\tilde{\chi}_1^0$ final states in order to reconstruct the invariant masses M(μ^+,μ^-) and M(e^+,e^-). After of fitting the expected edges on those spectra, would arise the following questions: whether the photon collider might actually serve for a precise mass measurement? Or whether the fitted values of the edges can compete with those already achieved of LHC, or do exist there a complementary role of photon collider in addition to the results from the e^+e^-?

8.3.2 Study of the 4-Muon and Missing Energy Final States

Before in entering in a more detailed analysis, we try to obtain a rough idea of the possible shapes of energy distributions of the species involved in (8.2), at the generator level. For this short excercise SHERPA-ISAJET and PYTHIA packages were used. Simulation have been carried out in two steps. Firstly, SHERPA was used for generating the $\gamma\gamma \rightarrow \tilde{\mu}_L^+\tilde{\mu}_L^- \rightarrow \mu^+\tilde{\chi}_2^0\mu^-\tilde{\chi}_1^0$ final states, whereas the second step PYTHIA was used to simulate the decay of $\tilde{\chi}_2^0$. The two-step procedure would neglect small interference effects by affecting the phase space integrations. However a robust treatment regarding this argument is beyond of the goals of this work. On the left panel of Fig. 8.7, energy of overall species as those indicated on first line of (8.2) are displayed. One can observe there the energy distributions of *primary* muons have almost the same shape in virtue of CP conservation. These distributions are in agreement with the ones examined in the study of the $\tilde{\mu}_L \rightarrow {}^{0}_{2}\mu$ decays. The simulation have demonstrated that an important fraction of the total energy is carried away by the $\tilde{\chi}_1^0$. The most remarkable fact is related to the morphology of the energy distributions. In effect, the variation of the center-of-mass energy due to the Compton backscattering is reflected in all distributions on what acquire a peaked characteristic. The right panel displays the energy spectra of the second and third lines of (8.2). While the $\tilde{\mu}_R$ decay into a *secondary* lepton $\mu^{+,a}$ accompanied by $\tilde{\chi}_1^0$, the hypothesis in what these four particles should still conserve their peaked shape despite of successive decays is confirmed. On the other hand, those as the *secondary* muons present similarly the same behavior and their energies are scattered between 1 GeV and 100 GeV. Furthermore, an accumulation of events around 40 GeV is noticeable. These energy spectra obtained at the generator level should not be too different of the ones obtained at the

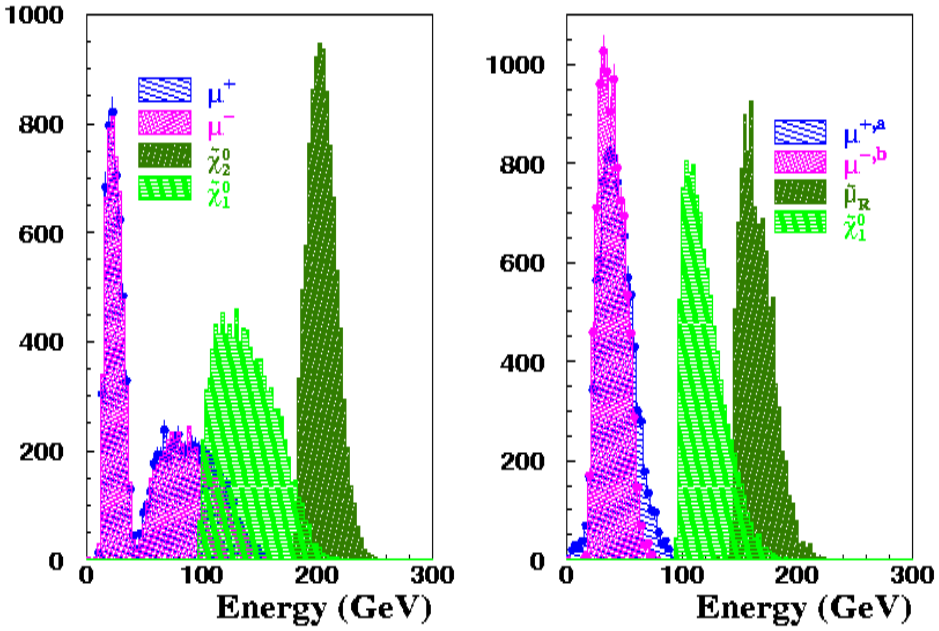

Figure 8.7: Generator level spectra showing the stages of cascade decay as indicated in (8.2). In left panel, energy of 4-particles is plotted. Note that the energy spectra for the μ^+ is almost the same of that of μ^-, thus both spectra appear to be superimposed. The right panel shows the energy of the species produced by the decay of $\tilde{\chi}_2^0$. The $\mu^{+,a}$ and $\mu^{-,b}$ spectra are hardly different because the first one comes from $\tilde{\chi}_2^0$ whereas the second one from $\tilde{\mu}_R$.

detector level. Note the range of muon energy in all cases is above 5 GeV, for what it guarantees an efficient reconstruction by assuming the same features already explained in previous sections.

The Signal Properties

As already stated the SPS1am model is used. Major inputs in SHERPA for simulation of $\gamma\gamma \to \mu^+\tilde{\chi}_2^0\mu^-\tilde{\chi}_1^0$ reactions (or 2→4) are $\sqrt{s}_{e^-e^-}$=600 GeV and P_{e^-}=0.85. Thus, for the $\tilde{\chi}_2^0$ decay PYTHIA was adjusted to have same SPS1am parameters. In addition we have simulated 1188 signal events. This number is calculated from

$$N_{4\mu} = 4 \cdot \mathcal{L} \cdot \sigma \cdot Br(\tilde{\mu}_L^- \to \mu^-\chi_1^0) \cdot Br(\tilde{\mu}_L^+ \to \mu^+\chi_2^0) \times \\ \times \mathrm{Br}(\tilde{\chi}_2^0 \to \tilde{\mu}_R^+\mu^-) \cdot \mathrm{Br}(\tilde{\mu}_R^+ \to \mu^+\chi_1^0) \qquad (8.3)$$

where σ is not affected for this new scenario. It occurs because sleptons masses do not suffer any change when tanβ is set to 4, contrarily to charginos

whose masses values become shifted in $\approx 5\%$ for $\tilde{\chi}_1^{\pm}$. The $\tilde{\chi}_2^0$ mass is also hardly affected in $\approx 1\%$ by which it gives rise to a minor displacement of both lower and upper limits of (7.12) and (7.13) respectively. So that the effective cross section of 30 fb is kept for the calculation of (8.3) as well as a luminosity of 1000 fb as established early. We remind that the right-handed smuon (selectron) decay into the lightest neutralino together to muon (electron) with a branching ratio of 100%. Simulation of detection of signal and background at the ILC have been efficiently carried out with SIMDET together with the overlapping of pile-up events having considered 1.8 pile-up events per bunching crossing. On Fig. 8.8 the t-channel exchange diagrams for production of the 4-muon final states are illustrated. A noteworthy property of signal is attributed to its topology. While *primary* muons are particularly "two-sided events", the *secondary* ones or those produced by $\tilde{\chi}_2^0$ are "one-sided events". This denomination had been coined in the past inside the context of theoretical calculations [B$^+$03] [B$^+$86]. Even more stringent, the opening angle between the *secondary* muons should be smaller than the *primary* ones. So that 4 charged tracks in the muon detector can be independently identified. A dedicated simulation with the package BRAHMS [Beh01b] supported by

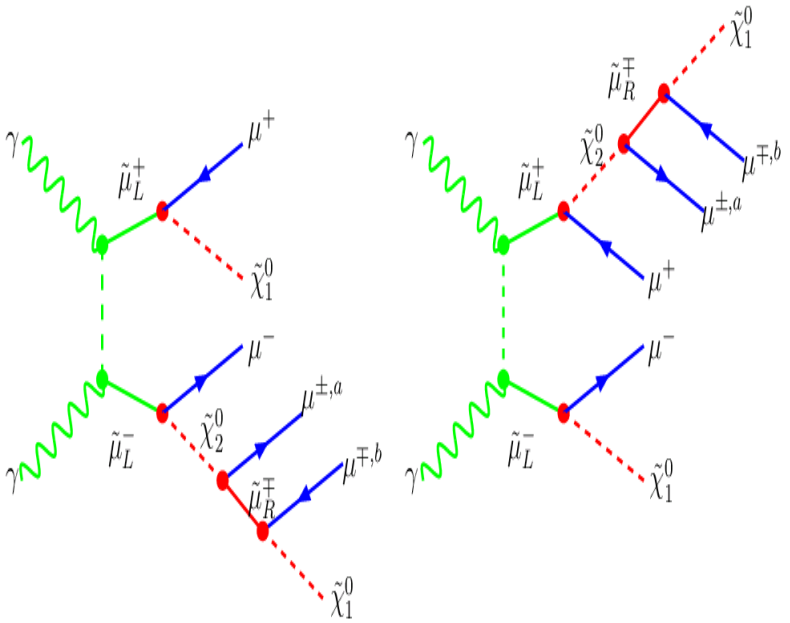

Figure 8.8: Feymann graphs showing the ways for producing the SUSY 4-muon final states. To note there that secondary muons, those produced by $\tilde{\chi}_2^0$, are labeled with an upper index (a) and (b).

GEANT [Gia00] have confirmed the hypothesis stated above by displaying

the expected geometry of the final states muons. In top panels of Fig. 8.9, the full reconstruction of two events is presented. The simulation have corroborated the fact that the primary $\mu^{\pm}$ and secondary ones ($\mu^{\pm,a,b}$) differs clearly in their opening angles. The background are uniquely constituted by SM reactions, $\gamma\gamma \to \mu^+\mu^-\mu^+\mu^-$ and $\gamma\gamma \to \mu^+\mu^-\tau^+\tau^-$ (with τ decaying into its muon channel) which contribute with 22500 and 580 events respectively. Event generation was achieved with AMEGIC++ [K$^+$01]. The $\gamma\gamma \to \mu^+\mu^-\mu^+\mu^-\nu\bar{\nu}$ reactions had been neglected by their small contribution to background. We perform a model-dependent strategy in the sense that we know in advance the $\tilde{\mu}_L$ and $\tilde{\chi}_1^0$ masses, expected to be measured from the ILC-LHC experiments.

Preselection and Selection

Initially, 1175 signal events had to be accepted. They contain up to 4 muons and a missing energy greater than 10 GeV. A very few percent of them were lost over the very forward regions roughly in a 1%. Consequently, individual muons of same charge are accounted together with their kinematical information. Based on the information provided by the top panels of Fig. 8.9 is possible to recognize and tag those muons of same sign coming from the $\tilde{\chi}_2^0$ or $\tilde{\mu}_L$. Indeed, another preselection cut is linked to the energy of *primary* muons. A precise information of the energy of at least two muons what are

Cut	Eff(%)	Pur(%)	$\Delta N_{4\mu}/N_{4\mu}$(%)
	100	5.02	12.96
$P_T(\mu^+,\mu^-)$ >5 GeV	88.97	21.16	6.69
10 GeV $< E_{\mu^+} + E_{\mu^-}$ <150 GeV	88.97	27.04	5.92
10 GeV $< E_{\mu^+,a} + E_{\mu^-,b}$ <150 GeV	88.05	53.04	4.25
10 GeV $< E_{\mu^+} + E_{\mu^-,a}$ <150 GeV	87.88	61.41	3.95
10 GeV $< E_{\mu^-} + E_{\mu^+,a}$ <150 GeV	87.63	65.89	3.82
30 GeV $< E_{\mu^+,b} + E_{\mu^-}$ <195 GeV	87.46	70.20	3.70
20 GeV $< E_{\mu^-,b} + E_{\mu^+}$ <200 GeV	82.99	84.56	3.46
145 GeV $< E_{4\ell} <$ 270 GeV	**81.82**	**89.01**	**3.39**

Table 8.3: Statistical behavior of signal for each applied cut.

in reality the most energetic ones, is supposed to be known. For these "two-sided", an individual muon should have their energies along the range given by 43 GeV and 153 GeV, being this muon derived from $\tilde{\mu}_L \to \tilde{\chi}_1^0\mu$, while the one of opposite sign is confined to have energies between 11 GeV and 43 GeV because of the $\tilde{\mu}_L \to \tilde{\chi}_2^0\mu$ decays. For completeness, throughout the

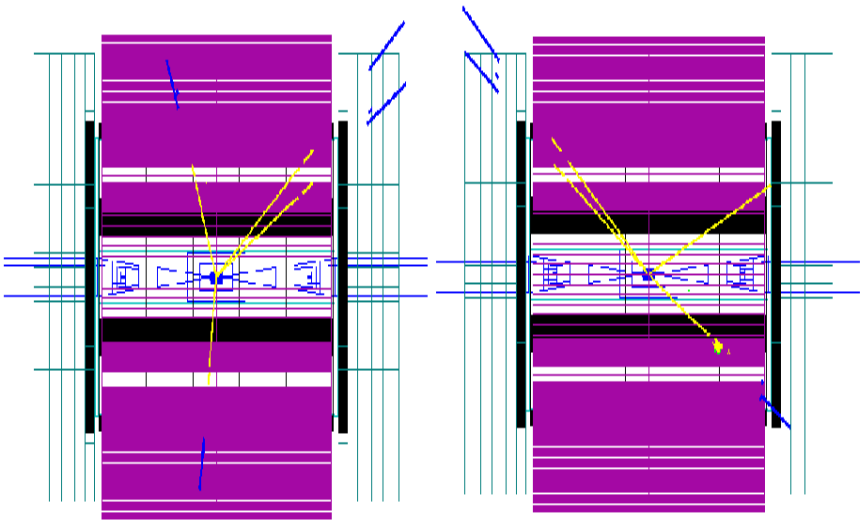

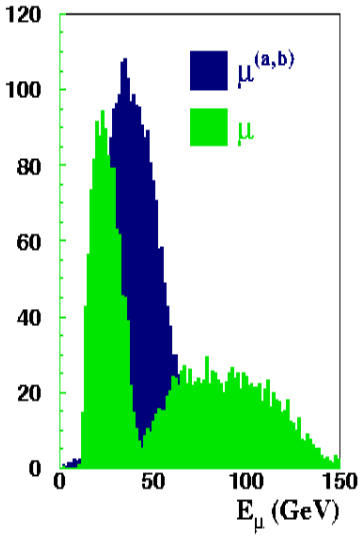

Figure 8.9: Top: Simulation of 4-muons final states with the package BRAHMS based on GEANT. Both *primary* and *secondary* muons have to be distinguished by measuring their opening angles. Bottom: reconstructed energy distributions of signal; by one hand those what are directly produced by left-handed smuons (denoted only by μ), and for the other hand the ones from the cascade (denoted by $\mu^{(a,b)}$).

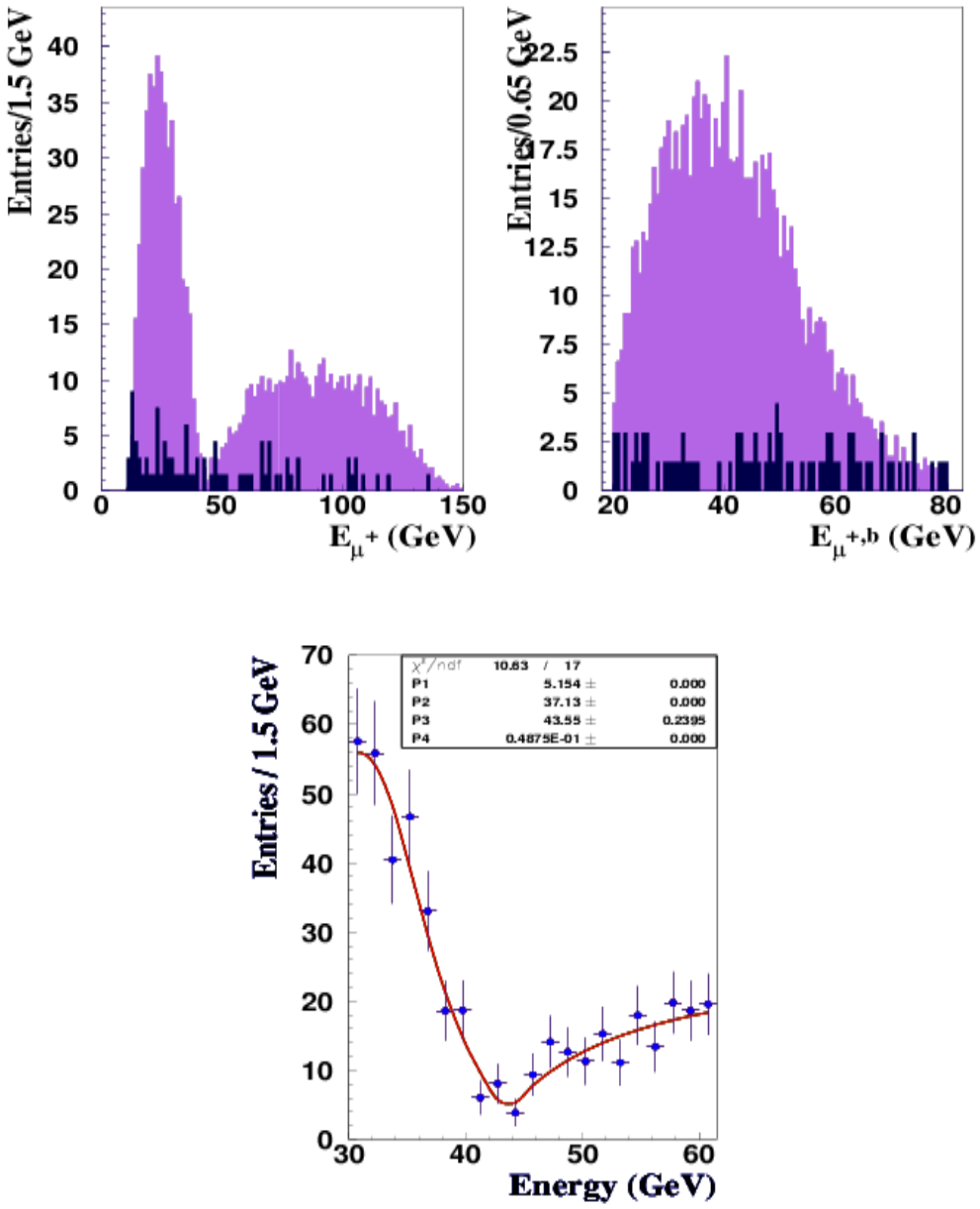

Figure 8.10: Top: Normalized histograms for *primary* (left) and *secondary* (right) signal and their major background ($\gamma\gamma \to \mu^+\mu^-\mu^+\mu^-$) after selection cuts. Bottom: Fitting along the dip region. Histograms containing energy distribution of primary muons were superimposed. Parameter P_3 denotes the fitted value of dip.

selection those events with a transversal momentum greater than 5 GeV are accepted. This cut variable takes information of the *primary* ones. Finally, it was opted to exploit the characteristics of the signal energy distributions and for this end, the variable $E_{\mu_1} + E_{\mu_2}$ where $E_{\mu_{1,2}}$ represents a *primary* or *secondary* muon, is used. We have searched by the most efficient pairs which led to increase the purity. They are listed in Table 8.3 as well as the statistical behavior of signal and its background. The cut procedure follows a criterion based on the sum of energies of two individual muons starting from the minimal values up to reach a value around the the smuon mass. The benefits in applying such algorithm is shown in Table 8.3, yielding an efficiency and purity of 81.82% and 89.01% respectively. In top panels of Fig. 8.10 are plotted the resulting histograms after cuts and their remaining background events produced by the $\gamma\gamma \to \mu^-\mu^+\mu^-\mu^+$ reactions.

Additionally, a relative statistical error of 3,39% was reached. In reality this efficient extraction from signal of noise is attributed to the evident difference between the SM and these "new physics" distributions.

Interestingly is the presence of a dip which is still noted after cuts selection. The manner of how the background events were defeated had not altered the morphology of dip. Logically, it serves for demanding further steps in the analysis. In the following, two aspects will be treated, the fitting of dip as an alternative way of measuring the $\tilde{\chi}_2^0$ mass and the extraction of the mass difference between two superpartners which take place during the cascade decay.

Measurement of the Heavy Neutralino Mass

In bottom panel of Fig. 8.10, is observed the presence of a dip which defines a priori the separation between the zones of $\tilde{\mu}_L \to \tilde{\chi}_1^0\mu$ and $\tilde{\mu}_L \to \tilde{\chi}_2^0\mu$ decays. The value of dip is in reality the endpoint of both zones, and its measurement would give rise to an alternative way in measuring the $\tilde{\chi}_2^0$ mass. It is actually an exceptional case, since such a dip could not be observed for the cases where the energy distributions are characterized by a flat nature, like the case of e^+e^- collider[1]. The disadvantage of having peaked distributions become now an unexpected advantage.

The endpoint method is usually used in e^+e^- collisions to measure the slepton and the lightest neutralino masses. In that case, knowledge of both edges are needed. In the present case, the dip turns out to be usable like an alternative method to have a precise measurement of the $\tilde{\chi}_2^0$ mass as we know at least the mass of $\tilde{\chi}_1^0$ and $\tilde{\mu}_L$ as argued early. On the other hand,

[1]A study of left-handed smuons produced at e^+e^- collisions is in preparation

SPS1am predicts that (7.12) and (7.13) ranges are not overlapped by sharing the same endpoint. Note in this case, the endpoint is slightly shifted to $\approx$ 43 GeV due to the variation of tanβ.

So, if cuts are capable to reduce efficiently the noise by leaving the signal substantially cleaned and undisturbed, then a dip should be observed. The fitting of the dip has a meaning, the measurement of the $\tilde{\chi}_2^0$ mass given by the relation

$$m_{\tilde{\chi}_2^0} = m_{\tilde{\mu}_L}\sqrt{1 - \frac{2E_d}{E_{\tilde{\mu}_L}(1+\beta)}} \tag{8.4}$$

where β=$\sqrt{1-(\frac{m_{\tilde{\mu}_L}}{E_{\tilde{\mu}_L}})^2}$, E_d denote the value of the dip, and $E_{\tilde{\mu}_L}$ is the maximum energy carried by the smuon and it is assumed to be roughly one-half of the maximum center-of-mass energy in the $\gamma\gamma$ system. In addition, an accurate information of $\tilde{\mu}_L$ mass is needed, but it should be provided by the ILC-LHC experiments. To perform the fit, only energy spectra made by *primary* muons are considered. For this end, it had been added to signal the remaining background histograms. Because of the small number of background events, polynomial functions were not required. Instead, we have adjusted the data helped by a modified Jacobian function, being expressed as follows,

$$F(E) = A + \frac{B}{\sqrt{(\frac{E-C}{X0})^2 - G}} \tag{8.5}$$

with $X0 = E - E_d$, and A, B, C, G are the parameters of function $F(E)$. After of identifying the values A, B, C, G we had have to fix them to determine the value of E_d. The fitting yields a δE_d=0.24 GeV as shown in Fig. 8.10 (bottom), having used the package MINUIT. Therefore, the associated statistical uncertainty for the $\tilde{\chi}_2^0$ mass can be estimated by assuming the following inputs: E_d=43.5 GeV, δE_d= 0.24 GeV, $E_{\tilde{\mu}_L} = \frac{1}{2}\sqrt{s}_{\gamma\gamma(max)} = 250$ GeV, $\delta E_{\tilde{\mu}_L} = \frac{1}{2}\delta\sqrt{s}_{\gamma\gamma(max)} = 2.5$ GeV, $m_{\tilde{\mu}_L}$= 143 GeV, $\delta m_{\tilde{\mu}_L}$= 0.18 GeV which led to $\delta m_{\tilde{\chi}_2^0}$=0.26 GeV.

Measurement of Mass Difference

In e^+e^- collisions, the production of 4-leptons accompanied of missing energy are expected to be almost negligible, but their purity of detection might be nearly above 90%. In such conditions is possible to get information of the mass difference as demonstrated in [B$^+$96]. Fig. 8.10 (top) shows the impressive statistical after cuts selection suggesting a posterior step aimed to recover the kinematics of superpartners involved in (8.2). Therefore the variables p^λ for *secondary* and P^λ *primary* muons are defined. These quantities

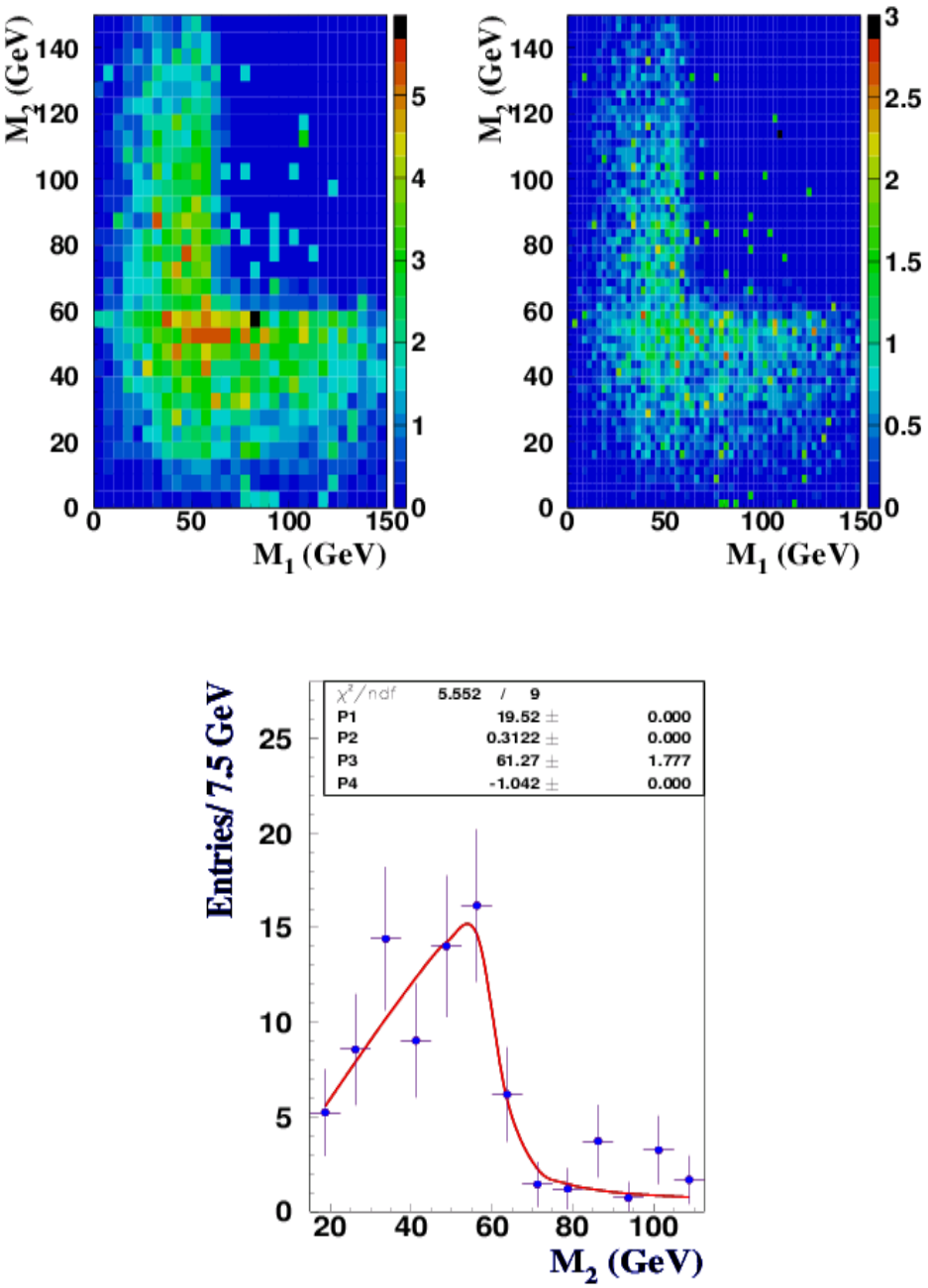

Figure 8.11: Top: 2-dimensional histograms for different binning by showing the presence of a sharp edge. To get information of the mass difference of the involved superparticles, a fit around the edge is performed. Bottom: the fit of the edge on the invariant mass distribution. On M_2 a step function was adjusted to the data. P_3 denotes the fitted value in GeV.

would allow us the construction of the invariant masses $M_1 = p_-^\lambda \cdot P_{\lambda,-}$ and $M_2 = p_+^\lambda \cdot P_{\lambda,+}$. On top panels of Fig. 8.11, are displayed for two different bins the Dalitz-like plots for the resulting signal and backgrounds histograms. These 2-dimensional histograms feature the signal events distributed along of a L-shape whereas the remaining background appears to be randomly scattered. Because of that peculiar shape of SUSY signal, a hard edge is observed. Looking on that, one gets for the edge a crude estimated in around 60 GeV. In order to be more precise, a fit on the edge is needed. The resulting fitted value is interpretated as already stated: the mass difference between $\tilde{\mu}_L$ and $\tilde{\mu}_R$. The fitting procedure was performed onto 1-dimensional histograms by selecting slices uniformly spaced from 2-dimensional histograms. Naturally we have considered the slices around the edge. Thus, we have applied the fit funcion (8.1). On the bottom panel of Fig. 8.11 we have plotted the best fit among several samples. Note that the function $M(E)$ is adjusted to data reasonably. Small fluctuations of fitted values was noted, by repeating the fit procedure for different binning. A troublesome point had been the fitting of the tail which in many cases it seems to have statistical fluctuations. Finally, have combined the results of all performed fits yielding a $\Delta m = m_{\tilde{\mu}_L}$ - $m_{\tilde{\mu}_R}$ = 61.20 GeV $\pm$ 1.9 GeV (stat) $\pm$ 0.2 GeV (sys). In summary, this result lies inside the value 61.6 GeV predicted by ISAJET. The statistical error is in essence due to the contamination of background below 60 GeV.

8.3.3 Study of the 2-Muon + Electron + Positron and Missing Energy Final States

The production of $\mu^+ e^- \tilde{\chi}_1^0 \mu^- e^+ \tilde{\chi}_1^0$ final states is a consequence of the cascade decays of $\tilde{e}_L$, $\tilde{\mu}_L$ and $\tilde{\chi}_2^0$. These states might be copiously created in pp collisions being one of the most cleanest SUSY channels to be discovered. Exactly these SUSY final states were first studied in Ref. [B$^+$96] where it was emphasized that such topologies are in some extent free of background. Fig. 8.12 illustrates the way in getting such events.

Preselection and Selection

Unlike the case of 4-muons, selectrons had been also simulated because they contribute significantly to the final state under discussion. It is actually manifested in the number of events which can be produced, as viewed in

Table 8.2. One can compute the number of signal events as follows

$$N_{4l} = \mathcal{L} \cdot (4 \cdot \sigma_{\gamma\gamma\to\tilde{\mu}_L^+\tilde{\mu}_L^-} \cdot Br(\tilde{\mu}_L^- \to \mu^-\chi_1^0) \cdot Br(\tilde{\mu}_L^+ \to \mu^+\chi_2^0) \cdot \\ \mathrm{Br}(\tilde{\chi}_2^0 \to \tilde{e}_R^+ e^-) \cdot \mathrm{Br}(\tilde{e}_R^+ \to e^+\chi_1^0) + \\ 4 \cdot \sigma_{\gamma\gamma\to\tilde{e}_L^+\tilde{e}_L^-} \cdot \mathrm{Br}(\tilde{e}_L^- \to e^-\chi_1^0) \cdot \mathrm{Br}(\tilde{e}_L^+ \to e^+\chi_2^0) \cdot \mathrm{Br}(\tilde{\chi}_2^0 \to \tilde{\mu}_R^+\mu^-) \\ \cdot \mathrm{Br}(\tilde{\mu}_R^+ \to \mu^+\chi_1^0)). \quad (8.6)$$

Hence, 2376 signal events were simulated at the generator level. For event generation, SHERPA is used for producing the $\gamma\gamma \to \mu^+\mu^-\tilde{\chi}_1^0\tilde{\chi}_2^0$ and $\gamma\gamma \to e^+e^-\tilde{\chi}_1^0\tilde{\chi}_2^0$ reactions simultaneously, whereas $\tilde{\chi}_2^0$ was allowed to decay in both $\tilde{\mu}_R, \mu$ and $\tilde{e}_R, e$. Last step was done with the assistance of PYTHIA. We remind that a luminosity and effective cross section of 1000 fb^{-1} and 30 fb are assumed. Then, we proceed to process all of them by means SIMDET. As usual, simulation at the detector level is devoted to tape information of momentum and energy of e^+, e^-, μ^-, and μ^+. Precisely, the preselection have

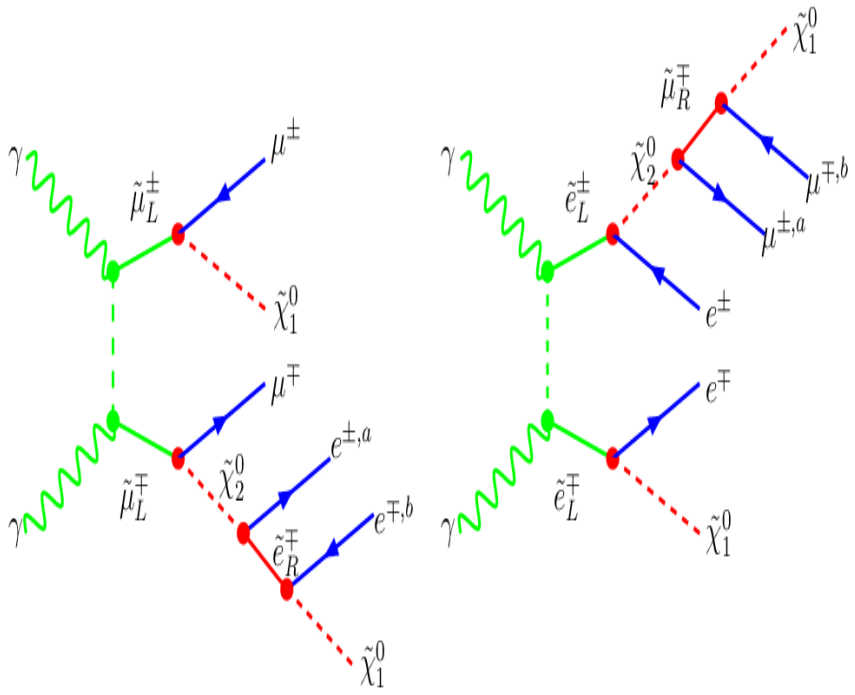

Figure 8.12: Feymann graphs showing 8 different contributions to produce the 4-lepton final states. To note there that secondary leptons, those produced by $\tilde{\chi}_2^0$, are labeled with an upper index (a) and (b).

demanded to accept those events with 4 leptons in the manner as depicted

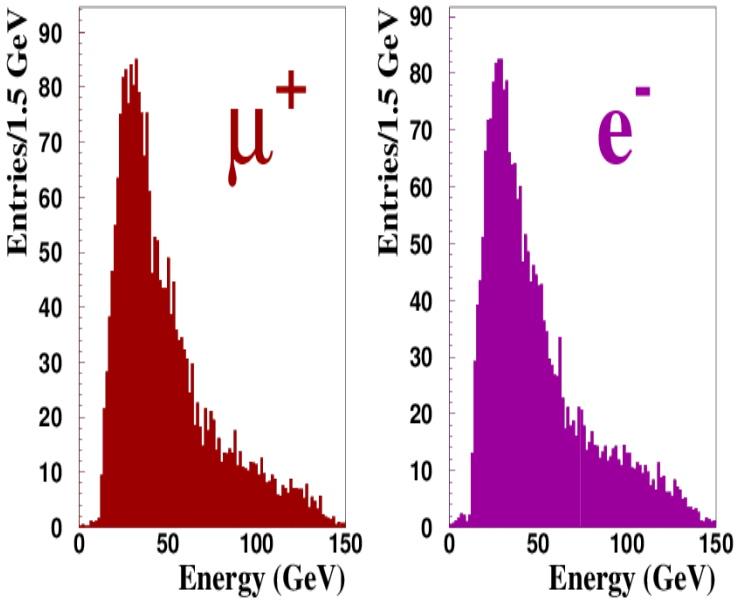

Figure 8.13: Energy distributions of muon and electron showing their similitude because of the overlapping of simultaneous contributions of both smuon and selectron.

in Fig. 8.12 and a missing energy greater than 10 GeV. Fig. 8.13 displays the detected energy distribution for μ^+ and e^-. The rest of leptons, μ^- and e^+ present a certain similitude with those plotted in that figure. It have been revealed that the energy distributions for all leptons have similar behavior. The reason of why all detected leptons has almost the same shape is attributed to the underlying topology. Since we demanded the detection of 4 leptons per event, the histogram corresponding to the μ^+ for example, (left panel Fig. 8.13) was filled in two ways: by events of *primary* muons derived directly from the left-handed smuon and with those events *secondary* ones which are produced in the cascade by the $\tilde{\chi}_2^0$. Thus, the resulting histogram is equivalent to the one obtained by the superimposition of left and right panels (top) of Fig. 8.10. The major background is given by the $\gamma\gamma \to e^+\mu^-e^-\mu^+$ reactions. A total of 18000 events were modeled with the package AMEGIC++. Aside, we used PYTHIA as generator supported by CIRCE in order to generate 580 events for the $\gamma\gamma \to \mu^+\mu^-\tau^+\tau^-$ reactions; the ones created by $\gamma\gamma \to W^+W^-Z^0$ reactions were not considered because of their small rate. Also, we have forced that the valid range for a candidate would have to have an energy between 10 GeV and 150 GeV. On the final selection, initially was applied a cut on the total transversal momentum by requiring

that the candidates should have at least a P_T greater than 5 GeV. The following cuts listed in Table 8.4 are uniquely builded with the information of the taped lepton energies.

Thus, the application of the cut procedure have brought positive consequences what are reflected on the obtained final statistics: a signal efficiency of 92.68% and purity of 93.15%. Furthermore, a relative statistical error of 2.21% was achieved. In other words, the effect in using uniquely information of lepton energy had been enough for a rather efficient discrimination. On left panel of Fig. 8.14 (top) is plotted the final distribution after final selection. Apart from the good statistics achieved, we would like to explore the possibility in to examinated the invariant mass of remaining events in order to evaluate the mass difference of superpartners in virtue of the graphs depicted in Fig. 8.12. Right panel of Fig. 8.14 (top) indicates us a hard edge on 85 GeV and thus we have performed an additional analysis to evaluate the mass difference between $\tilde{\chi}_2^0$ and $\tilde{\chi}_1^0$. It should be noted that the background does not damage the edge because of their smallness. Consequently, we have followed same fitting criterion like the one used for 4-muon studies.

Cut	Efficiency(%)	Purity(%)	$\Delta N_s/N_s$(%)
	100	11.66	6.00
$P_T(e^+, e^-, \mu^+, \mu^-)$ >5 GeV	99.75	61.59	2.62
10 GeV < E_{e^+} <150 GeV	99.49	68.70	2.48
10 GeV < E_{e^-} <150 GeV	99.12	75.22	2.38
10 GeV < E_{μ^+} <150 GeV	98.61	81.92	2.28
10 GeV < E_{μ^-} <150 GeV	98.15	87.28	2.22
30 GeV < $E_{e^+} + E_{e^-}$ <195 GeV	98.06	88.66	2.20
20 GeV < $E_{\mu^+} + E_{\mu^-}$ <200 GeV	97.85	89.46	2.19
20 GeV < $E_{e^+}+ < E_{\mu^-}$ <220 GeV	97.81	89.57	2.19
20 GeV < $E_{e^+}+ < E_{\mu^-}$ <220 GeV	97.77	89.59	2.19
145 GeV < $E_{4\ell}$ < 270 GeV	**92.68**	**93.15**	**2.21**

Table 8.4: Cut-flow of signal showing the effect of applied cuts on efficiency and purity.

Measurement of the Mass Difference

On the right panel of Fig. 8.14 (top) is accentuated a hard edge what actually is the mass difference $m_{\tilde{\chi}_2^0}$ - $m_{\tilde{\chi}_1^0}$. It was encountered a difficulty when the fit function pass over the tail of the distributions. It is due to statistical fluctuations of the Monte Carlo generator. In general, the fit results are not

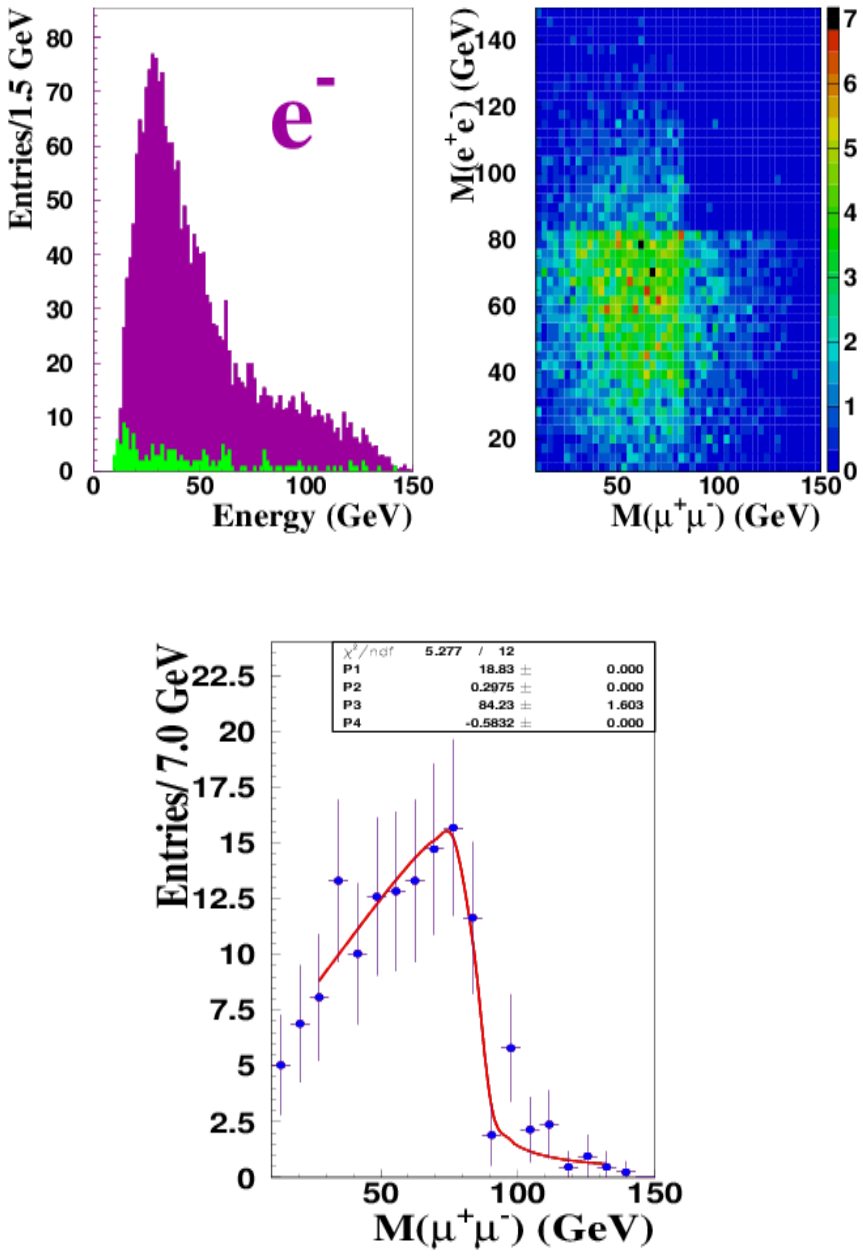

Figure 8.14: (Left-top) Normalized histograms for signal and remaining noise after selection cuts. (Right-top) 2-dimension histogram for $M(\mu^+, \mu^-)$ and $M(e^+, e^-)$. A hard edge is noted around 85 GeV which is supposed to be the mass difference between $\tilde{\chi}_2^0$ and $\tilde{\chi}_1^0$. On lower panels, the fit of the edge on the invariant mass distributions. P_3 denotes in both figures the fitted value in GeV.

too depending of the fitted region, for instance the one shown in Fig. 8.14 (bottom) indicates a minimum value for $M(e^+, e^-) = M(\mu^+, \mu^-) = 30$ GeV. Of course, we have accepted all the points along the tail which is extended up to 150 GeV. For regions between 50 GeV and 150 GeV, 60 GeV and 150 GeV the results turned out to be in disagree in around 0.1%. We have repeated several times the same procedure by changing the binning in the 1-dimensional histograms. This operation reveals a systematics in about 0.2 GeV. These uncertainties enter as a systematic into analysis. Finally, our estimate $\Delta m = m_{\tilde{\chi}_2^0}$ - $m_{\tilde{\chi}_1^0} = 84.82$ GeV $\pm$ 2.1 GeV (stat) $\pm$ 0.2 GeV (sys) have demonstrated not any discrepancy with the Monte Carlo value of 85.4 GeV provided by ISAJET.

Chapter 9

Conclusions

Through a Monte Carlo simulation we have examined the possibility of searching SUSY signals for the cases of the right and left-handed smuons at the TeV scale in the e^-e^+ and $\gamma\gamma$ colliders.

The case of the right-handed smuon at e^-e^+ collider have been of particular interest since such particle might be the first superpartner to be seen in experiments. Essentially, we have applied several cuts in order to separate the signal from its background. The simulation have shown that the presence of a forward detector would increase notably the signal purity by rejecting a sizeable amount of two-photons events. This analysis was aimed to extract the muon energy spectrum derived from the $\tilde{\mu}_R$ what gives the possibility in measuring the smuon mass. Therefore, the results have been $\delta m_{\tilde{\mu}_R} = 0.137$ GeV and $\delta m_{\tilde{\chi}_1^0} = 0.099$ GeV by assuming the SPS1a' scenario. It demonstrates excellent prospects for sparticles identification at the ILC e^-e^+ mode.

An analysis more speculative have been the searching of smuons at the $\gamma\gamma$ option at the ILC. In fact, we have investigated the production and detection of smuons in $\gamma\gamma$ collisions by assuming a plenty of assumptions. However a remarkable point in the whole procedure have consisted in the background rejection strategy. Unlike e^-e^+ collisions, in this thesis had been demonstrated that the identification and reconstruction of SUSY spectra is efficiently achieved without the necessity of appealing to complex strategies of preselection and selection of candidates. In this way, from these studies an error of 0.8% for the $\tilde{\mu}_R \to \mu\tilde{\chi}_1^0$ decay can be achievable. For the case of major importance, the $\tilde{\mu}_L \to \mu\tilde{\chi}_1^0$ decays can be extracted within a resolution of 0.98% by showing the potential of a photon collider as to SUSY studies.

In addition, a photon collider would offer a unique possibility in to explore rare topologies based on the fact of having high rates of left-handed smuon production. In some portions of parameter space, the number of

SUSY $4\ell + E^{miss}$ states can be copiously produced. We have searched the $\mu^-\mu^+\mu^-\mu^+\tilde{\chi}_1^0\tilde{\chi}_1^0$ and $\mu^-e^+\mu^+e^-\tilde{\chi}_1^0\tilde{\chi}_1^0$ final states what are actually an invaluable window to have access to a comfortable measuring of the $m_{\tilde{\mu}_L}$ - $m_{\tilde{\mu}_R}$ and $m_{\tilde{\chi}_2^0}$ - $m_{\tilde{\chi}_1^0}$ at the level of 1%. Although these results cannot compete with those expected from the LHC, the investigation have revealed interesting facts as for example the alternative manner in getting the $\tilde{\chi}_2^0$ mass. Moreover, a study for the $e^-\gamma$ option have led to determine $m_{\tilde{\chi}_2^0}$ - $m_{\tilde{\chi}_1^0}$ in a 2.4% of precision. All these results underline the importance of having a photon collider not only for Higgs and SM studies, but rather in to acquire more information about the dynamics of sparticles.

In summary, the results allow us to state that the photon collider might be conceived as a serious and potential machine to upgrade the e^+e^- collider. The present thesis address the question whether still there are more physics to be extracted from the $\gamma\gamma$ and $e^-\gamma$ colliders. This thesis suggests to carry out further simulations for extracting SUSY observables at the TeV scale (if SUSY is actually a low energy model).

Observable	LHC	ILC	$\gamma\gamma(2\mu)$	$\gamma\gamma(4\mu)$	$\gamma\gamma(2e2\mu)$	$e^-\gamma(3e)$
$m_{\tilde{\chi}_2^0}$	2.58	0.04		0.14		
$\tilde{\mu}_L \rightarrow \mu\tilde{\chi}_1^0$			0.98			
$\tilde{\mu}_L \rightarrow \mu\tilde{\chi}_2^0$			3.97			
$m_{\tilde{\chi}_2^0}$ - $m_{\tilde{\chi}_1^0}$	0.12	1.33			2.43	0.46
$m_{\tilde{\mu}_L}$ - $m_{\tilde{\mu}_R}$	0.32	0.24		3.08		

Table 9.1: Table of confrontation of relative errors between the results achieved in this work and the possible measurements to be done at LHC and ILC from Ref. [L$^+$04]. The relative errors are expressed in percent.

Bibliography

[A+01] Alexander, G.; et al.: TESLA The Superconducting Electron-Positron Linear Collider with an Integrated X-Ray Laser Laboratory Part IV - A Detector for TESLA. Technical report, TESLA Collaboration, 2001.

[A+02] Allanach, B.; et al.: Comparison of SUSY Mass Spectrum Calculations. In: , 2002. arXiv:hep-ph/0207314.

[A+07] Aarons, G.; et al.: ILC Reference Design Report Volume 1 - Executive Summary 2007. Technical report, ILC Global Design Effort and World Wide Study, 2007. arXiv:physics.acc-ph/07121950.

[Ant98] Antoniadis, I.: New Dimensions at a Milimeter to a Fermi and Superstrings at a TeV. In: *Phys. Lett.*, volume B346:p. 1, 1998.

[Aru63] Arutyunian, F. R. Tumanian V. A.: The Compton Effect on Relativistic Electrons and the Possibility of Obtaining High Energy Beams. In: *Phys. Lett.*, volume 4:p. 176, 1963.

[AS+05] Aguilar-Saavedra, J. A.; et al.: Supersymmetric Parameter Analysis: SPA Convention and Project . In: , 2005. arXiv:hep-ex/0511344.

[ATL99] ATLAS Collaboration: ATLAS Detector and Physics Performance. Technical Report TDR 15, CERN/LHC 99-15, Large Hadron Collider, 1999.

[B+71] Berestetski, V.; et al.: *Teoria Cuantica Relativista.* Editorial Reverte, 1971.

[B+86] Bartl, A.; et al.: Production and Decay of Neutralinos in e^+e^- Annihilation. In: *Nucl. Phys.*, volume B278:p. 1, 1986.

[B+87] Behrend, H. J.; et al.: Searches for Supersymmetric Particles with the CELLO Detector at PETRA. In: *Z. Phys. C*, volume 35:p. 181, 1987.

[B+96] Baer, H.; et al.: Supersymmetry Studies at Future Linear e^+e^- Colliders. In: *Phys. Rev. D*, volume 54:p. 6735, 1996.

[B+97] Barger, V.; et al.: Sparticle Production in Electron-Photon Collisions. In: *Phys. Lett. B*, volume 419:p. 233, 1997.

[B+03] Bartl, A.; et al.: CP Asymmetries in Neutralino Production in e^-e^+ Collisions. In: , 2003. `arXiv:hep-th/0308141`.

[B+05a] Bechtle, P.; et al.: Determination of MSSM Parameters from LHC and ILC Observables in a Global Fit. In: , 2005. `arXiv:hep-ph/0511006`.

[B+05b] Blair, G.; et al.: Reconstructing Supersymmetry at ILC/LHC. In: , 2005. `arXiv:hep-ph/0512084`.

[B+06] Bechtle, P.; et al.: FITTIN0-1.1.1. http://www-flc.desy.de/fittino, 2006.

[B+07] Behnke, T.; et al.: ILC Reference Design Report Volume 4 - Detectors 2007. Technical report, ILC Global Design Effort and World Wide Study, 2007. `arXiv:physics.acc-ph/07122356`.

[BB99] Barata, J.; Begalli, M., editors: *Particle and Fields (Proceedings of X Escola do Verao Andre Swiecca - Aguas do Lindoias Sao Paulo Brazil)*. World Scientific, 1999.

[Bec03] Bechtle, P.: The Search of Higgs Particle at OPAL PhD Thesis Hamburg University, 2003.

[Beh01a] Behnke, T.: The TESLA Project. In: *American Linear Collider Workshop*. Baltimore, Maryland, March 2001. URL `http://www.desy.de/~behnke/LC/tesla.pdf`.

[Beh01b] Behnke, T. and others: BRAHMS: A Monte Carlo for a Detector at a 500/800 GeV Linear Collider. Technical Report LC-TOOL-2001-005, DESY, 2001.

[Beh02] Behnke, T.: The 166 Experiment in SLAC. In: *ECFA-DESY Linear Collider Workshop - Prague*. 2002.

[BF02] Brinkman, R.; Floettman, K.: TESLA The Superconducting Electron-Positron Linear Collider with an Integrated X-Ray Laser Laboratory Part II - The Accelerator. Technical report, ILC Global Design Effort and World Wide Study, 2002.

[Bie07] Bienetruy, P.: *Supersymmetry: Theory, Experiment and Cosmology*. Oxford University Press, 1st edition, 2007.

[BT06] Baer, H.; Tata, X.: *Weak Scale Supersymmetry*. Cambridge University Press, 1st edition, 2006.

[Cho95] Choudhury, D.: Production of Heavy Selectrons in e^--Gamma Collisions. In: *Nucl. Lett. B*, volume 451:p. 16, 1995.

[Cuy93] Cuypers, F.: Cascade Decay of Selectrons. In: *Phys. At. Nucl.*, volume 56:p. 1460, 1993.

[D+07] Djouadi, A.; et al.: ILC Reference Design Report Volume 2 - Physics at the International Linear Collider 2007. Technical report, ILC Global Design Effort and World Wide Study, 2007. arXiv:hep-ph/07091893.

[E+04] Eidelman, S.; et al.: Particle Data Group Collaboration. In: *Phys. Lett.*, volume B592:p. 1, 2004.

[F+04] Freitas, A.; et al.: Sneutrino Production at e^+e^- Linear Collider - Addendum to Slepton Production. In: , 2004. arXiv:hep-ph/0408341.

[G.04a] G., Weinglein: Physics Interplay of the LHC and the ILC. In: , 2004. arXiv:hep-ph/0410364.

[G+04b] Gleisberg, T.; et al.: SHERPA 1.α A Proof-of-Concept Version. In: *JHEP*, volume 0402:p. 056, 2004.

[Gia00] Giani, S.: GEANT: Detector Description and Simulation Tool. Technical Report Program Library Long Writeup W5013, CERN, 2000.

[Gin81] Ginzburg, I.: Producion of High-Energy Colliding Gamma-Gamma and Gamma-e^- Beams with a High Luminosity at VLEPP Accelerators. In: *JETP Lett.*, volume 34:p. 491, 1981.

[GK90] Goto, A.; Kon, T.: Supersymmetric Particle Production at the TeV Gamma-Gamma Collider. In: *Europhys. Lett.*, volume 13:p. 211, 1990.

[GU02] Ghodbane, N.; U., Martyn. H.: . In: , 2002. arXiv:hep-ph/0201233.

[Hei05] Heinemeyer, S.: Towards High Precision Higgs-Boson Measurements at the International Linear e^+e^- Collider. In: , 2005. arXiv:hep-ex/0511332.

[Hig64] Higgs, P.: Broken Symmetries, massless particles and gauge fields. In: *Phys. Lett.*, volume 12:p. 132, 1964.

[I.95] I., Telnov V.: principles of Photon Colliders. In: *Nucl. Instr. A*, volume 355:p. 3, 1995.

[JR75] James, F.; Roos, M.: . In: *Comput. Phys. Commun.*, volume 10:p. 343, 1975.

[K+01] Krauss, F.; et al.: AMEGIC: version 1 Proof-of-Concept. In: , 2001. arXiv:hep-ph/0109036.

[Kle06] Klemz, G.: Private Communication, 2006.

[KM05] Klämke, G.; Mönig, K.: Studies of Chargino Production and Decay at a Photon Collider. In: *Eur. Phys. J. C*, volume 42:p. 261, 2005.

[Kol84] Kolanoski, H.: *Two-Photon Physics at e^-e^+ Storage Rings*. Springer Tracks in Modern Physics v. 105 Springer Verlag Ed., 1st edition, 1984.

[Kou07] Koutnezov, K.: PhD Thesis - Humboldt Universitat zu Berlin, 2007.

[KT02] Klanner, R.; Telnov., V.: TESLA The Superconducting Electron-Positron Linear Collider with an Integrated X-Ray Laser Laboratory Part IV The Photon Collider at TESLA 2002. Technical report, TESLA Collaboration, 2002.

[KZ06] Kilian, W.; Zerwas, P.: ILC: Physics Scenarios. In: , 2006. arXiv:hep-ph/0601217.

[L+04] Lafaye, R.; et al.: Supersymmetry at ATLAS. In: , 2004. arXiv:hep-ph/0410364.

[M+03] Mönig, K.; et al.: Measurement of the Polarization in the Photon Collider. In: , 2003. arXiv:hep-ex/0306135.

[M+06] Mönig, K.; et al.: Studies for a Photon Colider at the ILC. In: *Nucl. Instr. Meth. A*, volume 564:p. 243, 2006.

[Mar04] Martyn, H. U.: Study of Sleptons at Linear Collider - Supersymmetric Scenario SPS1a. In: , 2004. arXiv:hep-ph/0406123.

[Mar05] Martin, S.: Supersymmetry: Status and New Developments. In: *Lectures at the Summer School of ICTP*. Trieste, Italy, March 2005.

[Mar06] Martyn, S.: A Supersymmetry Primer. In: , 2006. arXiv:hep-ph/9709356.

[McP02] McPerson, R.: SUSY Searches: Lessons and Loopholes from LEP. In: *Proceedings of SUSY02: 10th Conference on Supersymmetry in Physics*. Hamburg, 2002.

[Mon96] Montarou, G. and Muanza, M.: The Search for Charginos and Neutralinos with ATLAS at LHC. Technical Report PCCF RI 9602 CERN Libraries GENEVA SCAN-9610095, Universite Blaise Pascal, Laboratoire de Physique Corpusculaire, 1996.

[NC03] Nieto-Chaupis, H.: Study of Smuons at TESLA - LC-PHSM-2003-074, 2003.

[Ohl] Ohl, T.: CIRCE 2.0: Beam Spectra for Simulating Linear Collider and Photon Collider Physics. ftp://heplix.ikp.physik.tu-darmstadt.de/pub/ohl/circe2/doc/manual.pdf.

[P+03] Paige, F.; et al.: ISAJET 7.69 A Monte Carlo Event Generator for pp, $p\bar{p}$ and e^+e^- Reactions. In: , 2003. arXiv:hep-ph/0312045.

[PAW95] PAW and HBOOK: Program Library Q121, CERN-Geneva 1995. Technical report, CERN, 1995.

[Poh02] Pohl, M. and Schreiber, J.: SIMDET: A Parametric Monte Carlo for a TESLA Detector. Technical Report DESY Reports 02-061, DESY-Zeuthen, 2002.

[Por03] Porod, W.: SPheno a Program for Calculating Supersymmetric Spectra, SUSY Particle Decays and SUSY Particle Production at e^+e^- Colliders. In: *Comp. Phys. COmmun.*, volume 153:p. 275, 2003.

[QWe07] QWeak: A Precision Test of the Standard Model and Determination of the Weak Charges of the Quarks Through Parity Violating e^- Scattering. http://www.jlab.org/qweak, 2007.

[R+01] Richard, F.; et al.: TESLA The Superconducting Electron-Positron Linear Collider with an Integrated X-Ray Laser Laboratory Part I - Executive Summary. Technical Report 23–2001, TESLA Collaboration, 2001.

[Ros03] Rosca, A.: The Detector and Interaction Region for a Photon Collider at TESLA. In: , 2003. arXiv:phys/0310005.

[Ros04] Rosca, A.: Studies of Higgs in a Photon Collider. In: , 2004. arXiv:hep-ex/0412345.

[RS99] Randall, L.; Sundrum, R.: Large Mass Hierarchy From a Small Extra Dimension. In: *Phys. Rev. Lett.*, volume 83:p. 3370, 1999.

[S+01] Sjöstrand, T.; et al.: PYTHIA 6.2 Physics and Manual. In: , 2001. arXiv:hep-ph/0108264.

[Sch97] Schulte, D.: Study of Electromagnetic and Hadronic Background in the Interaction Region of the TESLA Collider. Technical Report TESLA Report 97-08, DESY, 1997.

[Sta02] Stahl, A.: Private Communication, 2002.

[T+95] Tsukamoto, T.; et al.: Precision Study of Supersymmetry at Future e^+e^- Colliders. In: *Phys. Rev. D*, volume 51:p. 3153, 1995.

[Tel06] Telnov, V. I.: The Photon Collider at the ILC: Status, Parameters and Technical Problems. In: , 2006. arXiv:hep-ph/0604108.

[Tho06] Thompson, M. A.: Particle Flow Calorimeter at the ILC. In: , 2006. arXiv:phys/0607261.

[W+07a] W., Lohmann; et al.: Prospects to Measure the Higgs Boson Mass and Cross Section in e^+e^- →ZH Using the Recoil Mass Spectrum. In: , 2007. arXiv:phys/0710.2602.

[W+07b] Walker, N.; et al.: ILC Reference Design Report Volume 3 - Accelerator 2007. Technical report, ILC Global Design Effort and World Wide Study, 2007. arXiv:physics.acc-ph/07122361.

[Zar02] Zarnecki, A.: CompAz: Parametrization of the Photon Collider Luminosity Spectra. Technical Report LC-TOOL-2002-007, Warsaw University, 2002.

Apendix A: The FITTINO Input File

We provide the input file for the SPS1a scenario where we include the uncertainties of the branching ratio measurements at the photon collider. The input file is based on the FITTINO version 1.1. Below is an example, since the uncertainties of all known observables have been smeared around their respective error. massW 80.3150 +- 0.03900

massZ 91.1187 +- 0.00210
massTop 174.3000 +- 0.05000
massBottom 4.2000 +- 0.50000
alphas 0.1172 +- 0.00200
sin2ThetaW 0.2311 +- 0.00015
massh0 110.1870 +- 0.50000
massA0 431.9620 +- 1.30000
massH0 432.2550 +- 1.30000
massHplus 439.7790 +- 1.10000
nofit massSdownL 592.3710 +- 9.80000
nofit massSdownR 569.4010 +- 23.60000
nofit massSupL 587.1480 +- 9.80000
nofit massSupR 569.6690 +- 23.60000
nofit massSstrangeL 592.3700 +- 9.80000
nofit massSstrangeR 569.3930 +- 23.60000
nofit massScharmL 587.1510 +- 9.80000
nofit massScharmR 569.6790 +- 23.60000
nofit massSbottom1 534.2360 +- 5.70000
nofit massSbottom2 568.5430 +- 6.20000
nofit massStop1 422.7820 +- 2.00000
nofit massStop2 601.3820 +- 20.00000

massSelectronL 203.2820 +- 0.20000
massSelectronR 144.2300 +- 0.05000
massSnueL 187.0950 +- 0.70000
massSmuL 203.2910 +- 0.50000
massSmuR 144.2000 +- 0.12000
massStau1 134.0630 +- 0.30000
massStau2 207.4760 +- 1.10000
massGluino 625.3360 +- 6.40000
massNeutralino1 96.0168 +- 0.05000
massNeutralino2 180.2330 +- 0.08000
massChargino1 179.8540 +- 0.55000
massChargino2 382.6150 +- 3.00000
nofit cos2PhiL 0.6737 +- 0.00050
nofit cos2PhiR 0.8978 +- 0.00050
sigma (ee -> Z h0,500 GeV,-0.8,-0.6) 13.7432 +- 0.23 alias 1
sigma (ee -> Z h0,500 GeV,0.8,0.6) 11.6626 +- 0.21 alias 2
sigma (ee -> Z h0,500 GeV,-0.8,0.6) 43.4364 +- 0.43 alias 3
sigma (ee -> Z h0,500 GeV,0.8,-0.6) 28.8723 +- 0.33 alias 4
sigma (ee -> Z h0,400 GeV,-0.8,0.6) 69.9194 +- 0.69 alias 5
sigma (ee -> Z h0,400 GeV,0.8,-0.6) 46.4757 +- 0.45 alias 6
BR (SmuL -> Neutralino1 Muon) 0.5449 +- 0.01 alias 7
BR (SmuL -> Neutralino2 Muon) 0.1667 +- 0.02 alias 8
BR (Chargino1 -> Stau1 Nutau) 0.9388 +- 0.05 alias 9
fitModel MSSM
fitParameter TanBeta 10.0
fitParameter Mu 358.64562
fitParameter M1 101.809
fitParameter M2 191.7556
fixParameter M3 588.797
fitParameter massA0 399.767
fitParameter Xtau -3837.23
fixParameter MSelectronR 135.76
fixParameter MStauR 133.33
fitParameter MSmuR 135.760
fixParameter MSelectronL 195.21
fitParameter MSmuL 195.199
fixParameter MStauL 194.39
fixParameter Xtop -506.388
fixParameter Xbottom -4441.
fixParameter MSdownR 528.14
fixParameter MSstrangeR 528.134

fixParameter MSbottomR 524.718
fixParameter MSupR 530.253
fixParameter MScharmR 530.270
fixParameter MStopR 424.382
fixParameter MSupL 548.705
fixParameter MScharmL 548.702
fixParameter MStopL 499.972
universality MSelectronR MSmuR
universality MSelectronL MSmuL
LoopCorrections on
ISR on
Verbose off
PerformFit on
PerformSingleFits off
UseGivenStartValues on
FitAllDirectly on
BoundsOnX off
SepFitTanbX off
SepFitTanbMu off
SepFitmA off
XScanRange -5000. GeV -100. GeV
ScanX off
ScanParameters off
CalcPullDist off
UseSimAnnBefore off
UseSimAnnWhile off
TempRedSimAnn 0.6
MaxCallsSimAnn 450000
InitTempSimAnn 10000
Calculator SPHENO .../SPheno2.2.2/SPheno
UseMinos off
UseHesse off
NumberOfMinimizations 1
ErrDef 1.

Acknowledgements

First and foremost, I thank DESY (Hamburg and Zeuthen) for the full support to achieve this modest work. I would like to thank Professor Hermann Kolanoski for accepting me as PhD student at the Humboldt University at Berlin.
I would like to thank Professor Hannelies Klugge and Professor Klaus Mönig for accepting me as their student at DESY-Zeuthen. *O*f course I'm sure that it was not easy for them neither at the begining nor the end. Yet they were patient with me, fact that deserves all my respects. I've learned from their point of views not only in HEP but also in other aspects. Thus, their contribution in my formation as scientist had been invaluable. Viele danke!
Thanks also goes for alumni and current researchers of Zeuthen, Jürgen Schreiber, Sabine Riemann, Gunnar Klämke, Andreas Schälicke, Guido Klemz, Aura Rosca, Ralph Dollan, Ekaterina Koutnezova and Christian Grah. I'm also grateful with the SHERPA team at Dresden, specially to Steffen Schumann for his technical assistance of simulation of the SUSY 2→3 reactions.
I thank Frau Sabine Baer for the assistance that I have received from her in several administrative aspects during my years at DESY-Zeuthen. The usage of FITINO have demanded to have a communication with Peter Wienemann. Therefore I thank his support for the correct use of the code.
Finally, I must mention a few names, "Rudi" Leutenbauer *f*or his sincere friendship during my days of fun at Eichwalde, Abilio de Freitas at Venezuela, Bernd at Eichwalde, Barbel and Jürgen at Eichwalde as well (*c*old nights of "snow" and talks), Francisco De Zela Martinez for his contribution in my first days of learning Elementary Particles and Fields, and other excellent guys in both Zeuthen and Lima, and special thanks also goes for my best friends at Germany, Camila P. and Tanja W.

Erklärung

Hiermit erkläre ich, die vorliegende Arbeit selbständig ohne fremde Hilfe verfasst und nur die angegebene Literatur und Hilfsmittel verwendet zu haben. Ich habe mich anderwärts nicht um einen Doktorgrad beworben und besitze keinen Doktorgrad. Die Promotionsordnung der Mathematisch-Naturwissenschaftlichen Fakultät I der Humboldt-Universität ist mir bekannt.

Huber Nieto-Chaupis
September 2006